Suspension of A Point-Mass-Loaded Filament in Non-uniform Flows: Passive Dynamics of a Ballooning Spider

Moonsung Cho[1,2,*], Mariano Nicolas Cruz Bournazou[3], Peter Neubauer[1] and Ingo Rechenberg[4]

(1) Technical University of Berlin, Institute of Biotechnology, Ackerstraße 76 / ACK 24, 13355 Berlin, Germany

(2) University of Rostock, Animal Physiology, Albert-Einstein-Str. 3, 18059 Rostock, Germany

(3) Eidgenössische Technische Hochschule Zürich, Swiss

(4) Bionics and Evolution Technique, Ackerstraße 76 / ACK 1, 13355 Berlin, Germany

*Author for correspondence, E-mail: moonsung.cho@uni-rostock.de

Spiders utilize their fine silk fibres for their aerial dispersal, known as ballooning. With this method, spiders can disperse hundreds of kilometres, reaching as high as 4.5 km. However, the passive dynamics of a ballooning model (a highly flexible filament and a spider body at the end of it) is not well understood. The previous study (Rouse model: without consideration of an anisotropic drag of a fibre) suggested that the flexible and extendible fibres in a homogeneous turbulence reduces the settling speed of the ballooning model. However, the exact cause of the reduction of the settling speed is not explained and the isotropic drag of a fibre is not realistic in the low Reynolds number flow. Here we introduce a bead-spring model (Zimm model: the anisotropic drag of a fibre is considered.) to investigate the passive behaviour of the ballooning model in the various non-uniform flows (a shear flow, a periodic vortex flow field and a homogeneous turbulent flow). For the analysis of the wide range of parameters, we defined a dimensionless parameter, which is called 'a ballooning number'. The ballooning number means the ratio of Stokes' fluid-dynamic force on a fibre by the non-uniform flow field to the gravitational force of a body at the end of the fibre. Our simulation shows that the settling speed of the present model in the homogeneous turbulent flows shows the biased characters of slow settling as the influence of the turbulent flow increases. The causes of this slow sediment is investigated by simulating it in the wide rages of the shear flow. We revealed that the cause of this is the drag anisotropy of the filament structure (spider silk). In more detail, the cause of reduced settling speed lies not only in the deformed geometrical shape of the ballooning silk but also in its generation of fluid-dynamic force in a nonuniform flow (shear flow). Additionally, we found that the ballooning structure could become trapped in a vortex flow. This seemed to be the second reason why the ballooning structure settles slowly in the based homogeneous turbulent flow. The reduced settling speed in the previous study may also be caused with this trapping phenomenon by a quasi vortical flow in the homogeneous turbulence. These results can help our deep understanding of the passive dynamics of spiders ballooning in the atmospheric boundary layer.

1 Introduction

Passive flight of spiders, which is known as “ballooning”, is a unique method in animal locomotion. Spiders use their fine fibres as a sail for their aerial dispersal. It is known that some species of spiders can travel hundreds of miles and reach as high as a few km above sea level. Darwin observed spiders’ landing while he was traveling on the sea, about 100 km off from the Argentina seacoast (Darwin 1845). The entomology laboratory in United States department of agriculture collected the vast number of insects in the air with a biplane for five years and found a spider at the altitude of 4.5 km (Glick 1939). This passive flight of spiders is interesting from not only ecological viewpoint but also the viewpoints of physical question, “how can point-masses (particles) be spread widely and energy-efficiently through the air?”. However, the mechanism of this fluid-dynamics on the ballooning structure is not well understood. The ballooning structure is described as a very light and thin single filament (Rel atively heavy spiders spin multiple silks, but we consider the simplest case first.) with the weight of a body at the end. We refer to this as the ‘ballooning structure’.

The first fluid-dynamic approach is made by Humphrey (Humphrey 1987). He assumed a single silk ballooner and determined the possible physical dimensions (thickness and length of a fibre) of a ballooner from the viewpoints of fluid-dynamics, possible constraint by obstacles in the nature and mechanical property of a spider silk. However, the developed chart could not explain the ballooning of large spiders, heavier than 9 mg. Later, Suter suggested that spiders may use their legs to control their drag when they are suspending in the air (Suter 1992) and also provided the possible clues of the chaotic motion of the turbulent air flows (Suter 1999). In 2006, Reynolds showed that the flexible and extendible ballooning structure settles slower than that of a ballooning having inflexible and rigid silk (a single link ballooner). The study provided rational insight for spiders’ ballooning in nature. However, the simulation needs some improvements. First, the drag anisotropy of a fibre structure should be considered for the simulation of fibre dynamics, because various filament-like structures in nature, for example, cilium, flagellum and pappus, experience and generate anisotropic drag forces (Purcell 1977, Childress 1981, Happel and Brenner 1986). However, the simulation considered isotropic drag on a spider silk. Second, the rigid silk model in the simulation is described as a dumbbell model. This structure is hard to be regarded as a rigid silk in the turbulent flow. Third, the simulation regards that a spider silk is flexible and extendible. The consideration of the flexibility is reasonable. However, the consideration of the extendibility should be reexamined by the following reason. From the simple calculation, the extendibility of a spider silk during a flight is almost negligible, because the 0.5 mg spider (either the case of a small spider or the distributed weight of a large spider, which use tens of fibres, on an single fibre) weight extends only 47 mm in length (1.5% elongation; elastic modulus: 10 Gpa; Gosline et al. 1999) in the case of a spider silk that is 3 m long and 200 nm thick (Cho et al. 2018). However, the study provides the economical insight in methodology. Although Zhao et al. recently implemented the very detailed numerical simulation using an immersed boundary method, the proposed simulation was limited in two-dimensional flow and the lengths of a spider silk is limited under 20 cm (Zhao et al. 2017). If we introduce the chain-like fibre and the unsteady-random-Fourier-modes based turbulence model, the simulation time can be enormously saved and various combinations of physical parameters can be investigated by the simulation.

From the view of physics, the ballooning structure has three unique features. First, two different flow regimes are involved in its dynamics. Because a ballooning silk shows the feature of extreme high slenderness (16.1×10^7, Cho 2018), the structure has two different length scales (thickness, 200 nm, and length, 3.22 m, of it, Cho 2018). Therefore, the unique feature appears, that the small segment of a spider silk is dominated by the low Reynolds number flow, while the behaviour of the entire silk is governed by the high Reynolds number flow, the turbulent flow. The upper limit of the Reynolds number is about 0.04 ($Re = \rho V d/\mu$; air density: 1.225 kg m^{-3}; maximum possible velocity: 3 m s^{-1}; thickness of spider silk: 211 nm; dynamic viscosity of air: 1.837 x 10^{-5} kg m^{-1} s^{-1}). Second, the ballooning silk in turbulent wind is exposed to different wind vectors, while the aerial seeds are exposed to quasi homogeneous (uniform) flow fields because of their small sizes. Whether or not the ballooning structure gains energy from this nonuniform flow, if it is so, how the structure extracts energy for its long permanence in the air, can be interesting questions. Third, the asymmetric characteristics of a fibre appears because of the weight of the body at the end of a fibre. As the lower end of a fibre is constrained by the weight (body), the upper part of a fibre can be distorted and adapted more easily than the lower part of a fibre. How an asymmetrically constrained fibre behaves in a non-uniform flow and what it influences on its dynamic can be also interesting questions in the ballooning flight of spiders.

The fibre suspension in low Reynolds number flow has been frequently dealt in polymer dynamics (Yamamoto and Matsuoka 1993, Ning and Melrose 1999, Schroeder et al. 2005, Delgado-Buscalioni 2006, Gerashchenko and Steinberg 2006, Winkler 2006, Lindström and Uesaka 2007, Das and Sabhapandit 2008, Delmotte et al. 2015) and in the region of DNA stretching (Bustamante et al. 1994, Perkins et al. 1994, 1995, Jian et al. 1997, Larson 1997, Bustamante et al. 2000, Wong et al. 2003, Schroeder et al. 2004, Lee and Thirumalai 2004, Shaqfeh 2005, Wang and Lu 2007, Jo et al. 2009, Dai et al. 2014). However, the applied flows on these studies are not turbulent flow, but rather a simple shear flow or Brownian motion of solution molecules. Recently, the motion of a fibre in the turbulent flows is paid attention because of its anisotropic shape and studied by experiment (Brouzet and Le Gal 2014, Verhille and Bartoli 2016). However, the Reynolds number, which the local segment of a fibre experiences, is rather in the range of a moderate Reynolds number flow, about $Re \approx 4000$ than a low Reynolds number flow, $Re < 0$. Asymmetric condition of a fibre is mostly studied as a tethered fibre (Doyle et al. 2000, Ladoux and Doyle 2000, Ibáñez-Garcıá and Hanna 2009, Litvinov et al. 2011). Suspension of a flexible fibre under asymmetric condition is first simulated by Reynolds et al. (2006) for the study of ballooning dynamics. The study proposed that turbulent wind may reduce the rate of fall of the spider by deforming and stretching the flexible fibres. The study points out that the extendibility and flexibility of a filament may be the causes of the settling retardation. However, the model did not consider the drag anisotropy of a fibre (Rouse model; Rouse 1953, Dhont 2003, Reynolds at al. 2006, Doi and Edwards 2007), which is an important factor in fibre dynamics in the low Reynolds number flow (Purcell 1977, Childress 1981, Happel and Brenner 1986).

There are two representative aspects to the study of ballooning. One is from the viewpoint of fluid dynamics, which is a primary factor in the passive aerial dispersal of animals and plant seeds (Humphrey 1987, Suter 1991, 1992, 1999, Reynolds at al. 2006, Zhao et al. 2017, Cho et al. 2018). The other is from the viewpoint that tries to find clues from the Earth's electric field (Gorham 2013, Morley and Robert 2018). In the fluid dynamic approach, the atmospheric turbulent flow has been examined as an influential factor for high aerial dispersal capability (Suter 1999, Reynolds 2007, Zhao et al. 2017), because flexible spider silks are deformed by turbulent flows and fall

slowly (Reynolds 2006). However, the question of how the physical mechanism behind this works has not yet been answered. In the Earth's electric field approach, moreover, it has recently been reported that the electric field induces spiders' pre-ballooning (tiptoe) behaviour (Morley and Robert 2018). Despite this, we are still on the way to understand the electrical properties of a spider silk in many electrical conditions and the behind physics of the electrical flight (Vollrath and Edmonds 2013, Ortega-Jimenez and Dudley 2013, Kronenberger and Vollrath 2015, Joel Baumgartner 2017).

In this study, we focus on the understanding of the suspension character of the ballooning structure (an asymmetrically-constrained fibre) in the nonuniform flows from the viewpoint of fluid-dynamics. To describe a flexible fibre, we employ a bead-spring model considering hydrodynamic interaction between beads (Zimm model, which can describe the anisotropic drag of a fibre). There are two major purposes in this study. First, we want to clarify the role of anisotropic drag of a fibre in spiders' flight. Second, whether or not this fibre induces preferential motion of a ballooning structure in the homogeneous turbulent flow.

2 Methodology

According to the data acquired by Cho et al. (2018), the spider silks are locally exposed to a low Reynolds number flow. However, the silks as a whole are passively governed by the chaotic motions of turbulence, as their length on average is 3.22 m. Additionally, most of the weight of the airborne object is concentrated at one end of the silk. This asymmetric (eccentric) feature may in fact be the point of interest when investigating its behaviour in turbulent conditions. This idea will now be investigated with the help of numerical computation. For the concentration on the asymmetric distribution of the mass on a fibre, several things are assumed: (i) a single silk ballooner; (ii) ignorance of the effect of the body size (the diameter of a spider body equals to the thickness of a silk); (iii) no consideration of the inertia of the spider body.

2.1 Modelling

Due to the extreme thinness and long length of each fibre, high computational performance and extensive time are required to solve the dynamics of this flexible thin filament. Therefore, we employ a relatively simple method, the bead-spring model, to describe a flexible filament and simulate the motion of a ballooning structure in various non-uniform fluid-flows. Owing to its fast calculation capacity, this model offers a significant advantage for the investigation of various simulation parameters.

To investigate the dynamics of a highly-slender filament with the bead spring model, which has relatively small slenderness of 45-120, a nondimensional parameter is defined and an artificial fluid model is applied, the motion which resembles that of homogeneous turbulence of the air, but that has high viscosity. These treatments enable

the incorporation of the two different flow regimes in a single model and the universal analysis under the condition of different scales of the structure and various properties of fluids is possible.

2.1.1 Bead-Spring Model

To model a ballooning silk that is suspended in the air flow, we introduce the bead-spring model (Zimm model), which is frequently used to approach the polymer physics and dynamics of a micro-swimmer (Doi and Edwards 1986, Yamamoto and Matsuoka 1993, Gauger and Stark 2006, Lindström and Uesaka 2007). Each bead is connected to the other with a tensile and a bending spring. By adjusting each stiffness value, we can simulate various extendibility and flexibility values of a filament. (see Figure 1) Moreover, each bead experiences hydrodynamic viscous drag in a low Reynolds number flow, which is governed by Stokes' law (see Eqn. (2.1); Happel and Brenner 1986). η indicates dynamic viscosity of fluid medium. a is radius of a bead and U is relative flow velocity on the bead. The Zimm model considers hydrodynamic interactions between beads. This consideration can describe the anisotropic drag of a thin filament in a low Reynolds number flow, which show the drag different between a transverse drag and a longitudinal drag (Purcell 1977, Childress 1981, Happel and Brenner 1986, Gauger and Stark 2006).

$$F = 6\pi\eta a U \tag{2.1}$$

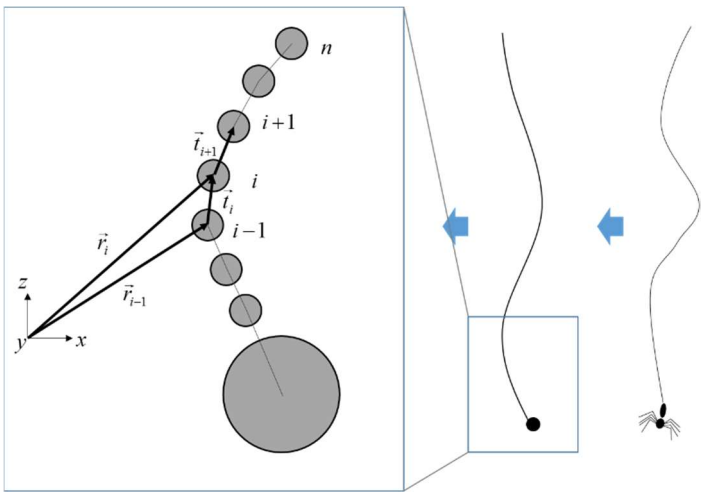

Figure 1. Bead-spring model for a ballooning spider.

In a low Reynolds number flow, the influence of inertia is almost negligible. This means that at every moment, the net force on the structure is zero (see Eqn. (2.2); Doyle and Underhill 2005). The net force $\boldsymbol{F}_i^{total}$ on each bead includes a fluid-dynamic force $\boldsymbol{F}_i^F$, a gravity force $\boldsymbol{F}_i^G$, a stretching force $\boldsymbol{F}_i^S$ and a bending force $\boldsymbol{F}_i^B$:

$$\boldsymbol{F}_i^{total} = \boldsymbol{F}_i^F + \boldsymbol{F}_i^G + \boldsymbol{F}_i^S + \boldsymbol{F}_i^B \approx 0 \tag{2.2}$$

The fluid-dynamic force is proportional to the fluid velocity. Therefore, resistances are defined as a reciprocal of bead mobilities $\boldsymbol{\mu}_{ij}$:

$$\boldsymbol{F}_j^F = \frac{1}{\boldsymbol{\mu}_{ij}}\left(\boldsymbol{u}^\infty(\boldsymbol{r}_i) - \frac{d\boldsymbol{r}_i}{dt}\right) \tag{2.3}$$

The bead mobility is derived through the consideration of the hydrodynamic interactions between beads. Here, we introduce the Rotne-Prager approximation, which can be applied to different sizes of beads (see Eqn. (2.6); Jeffrey and Onishi 1984, Gauger and Stark 2006):

$$\frac{d\boldsymbol{r}_i}{dt} = \boldsymbol{u}^\infty(\boldsymbol{r}_i) + \sum_j \boldsymbol{\mu}_{ij}\left(\boldsymbol{F}_j^G + \boldsymbol{F}_j^S + \boldsymbol{F}_j^B\right) \tag{2.4}$$

$$\boldsymbol{\mu}_{ii} = \mu_0 \mathbf{1} \quad \text{with} \quad \mu_0 = \frac{1}{6\pi\eta a_i} \tag{2.5}$$

$$\boldsymbol{\mu}_{ij} = \frac{1}{6\pi\eta \boldsymbol{r}_{ij}}\left[\frac{3}{4}\left(\mathbf{1} + \hat{\boldsymbol{r}}_{ij} \otimes \hat{\boldsymbol{r}}_{ij}\right) + \frac{1}{4}\frac{a_i^2 + a_j^2}{\boldsymbol{r}_{ij}^2}\left(\mathbf{1} - 3\hat{\boldsymbol{r}}_{ij} \otimes \hat{\boldsymbol{r}}_{ij}\right)\right] \tag{2.6}$$

The gravity forces can be defined as follows:

$$\boldsymbol{F}_i^G = [0 \quad 0 \quad -v_i(\rho_i - \rho_{air})g]^{\mathrm{T}} \tag{2.7}$$

Here, we consider a linearly varying spring. Therefore, the total stretching energy can be described as in Eqn. (2.8), while the stretching force on a bead can be obtained by differentiating Eqn. (2.8):

$$E^S = \frac{1}{2} k_0 \sum_{i=2}^{N} (l_i - l_0)^2 \tag{2.8}$$

$$\boldsymbol{F}_i^S = -\boldsymbol{\nabla}_{\boldsymbol{r}_i} E^S = -k_0(l_i - l_0)\hat{\boldsymbol{t}}_i + k_0(l_{i+1} - l_0)\hat{\boldsymbol{t}}_{i+1} \tag{2.9}$$

The bending force can also be obtained by differentiating the bending energy on a bead (see Eqn. (2.11)):

$$E^B = \frac{A}{l_0} \sum_{i=1}^{N} f_i (1 - \hat{\boldsymbol{t}}_{i+1} \cdot \hat{\boldsymbol{t}}_i) \text{ where } f_i = \begin{cases} 1 \ for\ 2 \le i \le N-1 \\ 0 \ for\ i = 1, N \end{cases} \tag{2.10}$$

$$\begin{aligned} \boldsymbol{F}_i^B = -\boldsymbol{\nabla}_{\boldsymbol{r}_i} E^B = \frac{A}{l_0} \Bigg\{ & \frac{f_{i-1}}{l_i} \hat{\boldsymbol{t}}_{i-1} - \left[\frac{f_{i-1}}{l_i} \hat{\boldsymbol{t}}_{i-1} \cdot \hat{\boldsymbol{t}}_i + \frac{f_i}{l_{i+1}} + \frac{f_i}{l_i} \hat{\boldsymbol{t}}_i \cdot \hat{\boldsymbol{t}}_{i+1} \right] \hat{\boldsymbol{t}}_i \\ & + \left[\frac{f_i}{l_{i+1}} \hat{\boldsymbol{t}}_i \cdot \hat{\boldsymbol{t}}_{i+1} + \frac{f_i}{l_i} + \frac{f_{i+1}}{l_{i+1}} \hat{\boldsymbol{t}}_{i+1} \cdot \hat{\boldsymbol{t}}_{i+2} \right] \hat{\boldsymbol{t}}_{i+1} - \frac{f_{i+1}}{l_{i+1}} \hat{\boldsymbol{t}}_{i+2} \Bigg\} \end{aligned} \tag{2.11}$$

For details, please refer to Gauger and Stark 2006.

2.1.2 Turbulent Model

The chaotic motion of flows is modelled by Fung's kinematic simulation, which describes the turbulent flow with multiple Gaussian random velocity fields (see Figure 2). This model was originally developed by Kraichnan (1970), modified by Drummond et al. (1984), Turfus (1985) and Fung et al. (1992), and later used to model turbulent flows for various purposes: for example, the study of turbulent structures (Fung 1996, Vassilicos and Fung 1995, Fung and Perkins 2008, Suzuki and Sakai 2012, Lafitte et al. 2014), investigation of particle dynamics (Fung 1993, Sakai et al. 1993, Fung 1998, Fung and Vassilicos 1998, Fung 2003, Gustavsson et al. 2012), etc. The turbulence model is intended to be homogeneous and to show von Karman energy spectrum, which can describe grid-generated turbulence and the spectrum in natural wind (Harris 1971, Bearman 1972, Hunt 1973).

$$\boldsymbol{u}(\boldsymbol{r}, t) = \sum_{n=1}^{N} \left[\frac{\boldsymbol{a}_n \times \boldsymbol{k}_n}{|\boldsymbol{k}_n|} cos(\boldsymbol{k}_n \cdot \boldsymbol{r} + \omega_n t) + \frac{\boldsymbol{b}_n \times \boldsymbol{k}_n}{|\boldsymbol{k}_n|} sin(\boldsymbol{k}_n \cdot \boldsymbol{r} + \omega_n t) \right] \tag{2.12}$$

The subscript n refers to the quantity of the n-th Fourier mode. The wavenumber vectors $\boldsymbol{k}_n$ are randomly chosen on each spherical shell of radius k_n. The coefficients $\boldsymbol{a}_n$ and $\boldsymbol{b}_n$ are determined by picking independently random vectors from a three-dimensional isotropic Gaussian distribution, with zero mean vector and variance $3\,\gamma \int_{k_n-\delta k/2}^{k_n+\delta k/2} E(k)dk$, where $\gamma = \int_0^\infty E(k)dk / \int_0^{k_\eta} E(k)dk$ and $\delta k = (k_\eta - k_c)/(N_k - 1)$ (Fung et al. 1992). Wavenumbers range from $k_c = 1$ to $k_\eta = 10$. For 10 Fourier modes, $k_n = k_c + (k_\eta - k_c)\,(n-1)/(N_k - 1)$, where $N_k = 10$ (Fung et al. 1992). Therefore, the sizes of eddies range from 0.628 to 6.28.

The 'von Karman' energy spectrum is expressed as follows (Hinze 1975, Fung et al. 1992):

$$E(k) = \frac{g_2 k^4}{(g_1 + k^2)^{17/6}} \tag{2.13}$$

$E(k)$ is normalised to give $\langle u_1^2 \rangle = \langle u_2^2 \rangle = \langle u_3^2 \rangle = 1$, meaning that the turbulent kinetic energy is $3/2$ (Fung 1990, Fung et al. 1992):

$$\frac{1}{2}\langle \boldsymbol{u}^2 \rangle = \int_0^\infty E(k)dk = \frac{3}{2} \tag{2.14}$$

The integral length scale is also normalised as Eqn. (2.14) (Monin and Yaglom 1977):

$$L_{11} = \frac{3\pi}{4} \int_0^\infty k^{-1} E(k)dk \Big/ \int_0^\infty E(k)dk = 1 \tag{2.15}$$

We thus obtain the numerical constants $g_1 = 0.558$ and $g_2 = 1.196$ (Hunt 1973).

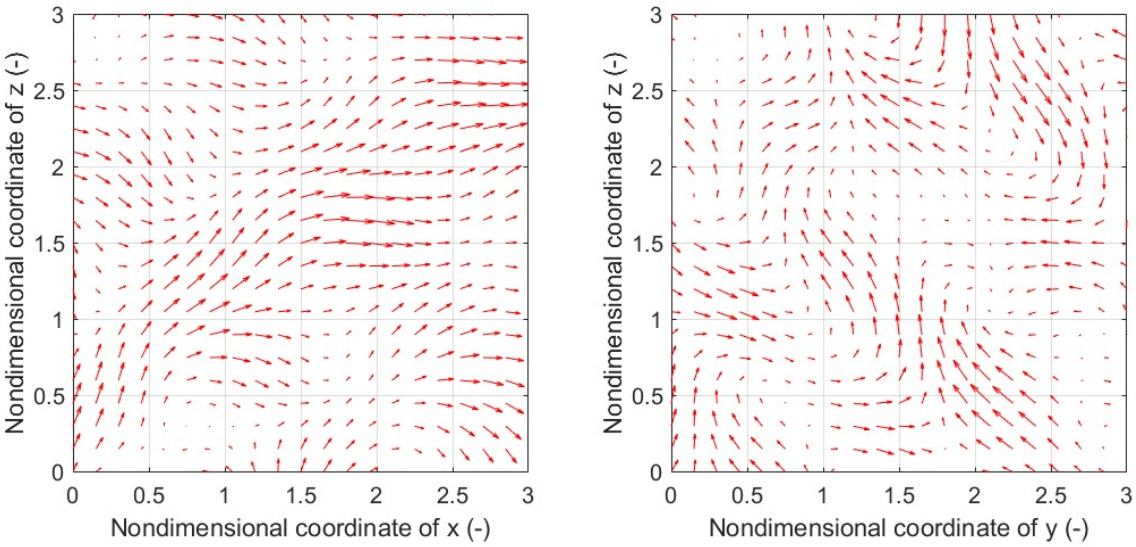

Figure 2. Cross-sectional velocity fields of the 3-dimensional homogeneous turbulence.

2.1.3 Shear Flow Model

In order to investigate the sediment characteristic in a non-uniform flow, a shear flow is used. Only horizontal components exist in a shear flow. Therefore, it is a very good model to investigate the sediment characteristic (vertical motion) of a ballooning structure in a non-uniform flow. Shear flow can be described as in Eqn. (2.16) (γ refers to shear rate, which has units of s^{-1}, while z is the vertical coordinate; see Figure 3):

$$\boldsymbol{U}(z) = [\gamma z \quad 0 \quad 0] \tag{2.16}$$

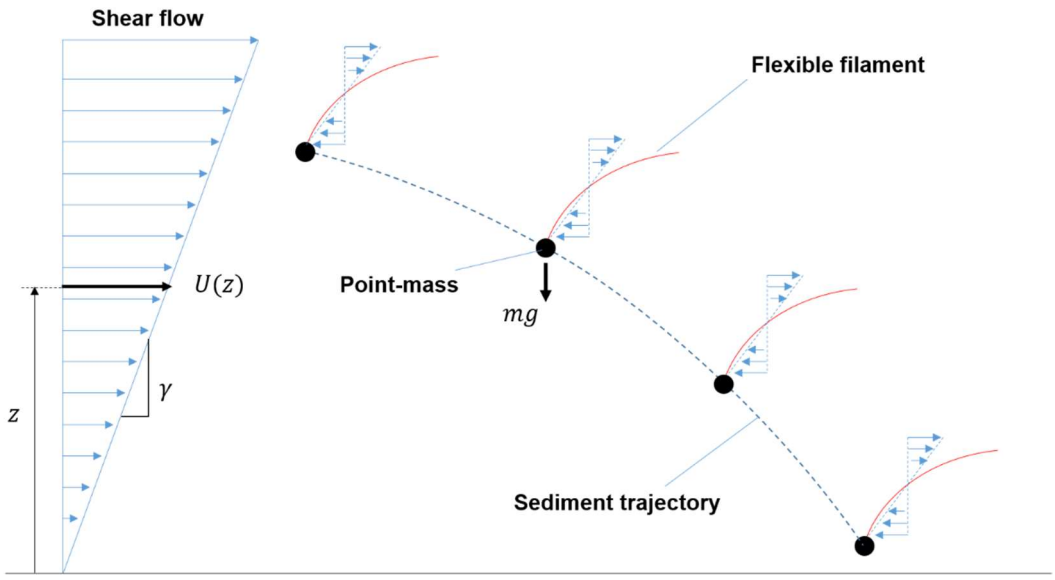

Figure 3. Schematic of the simulation in a shear flow.

2.1.3.1 Decomposition of Velocity Fields

To figure out the physical cause of settling speed reduction of a ballooning structure in a shear flow, we decompose the relative flow velocities $\boldsymbol{U'}_j$ on beads into the vertical and horizontal components of the relative flow velocities (see Eqn. (2.18) and Figure 4). This decomposition is valid because bead spring models are governed by linear relations. From the vertical components of the relative velocities on beads $\boldsymbol{U'}_j^V$, we can calculate the vertical resistance force due to the pure geometric shape of a filament (see Eqn. (2.20)). From the horizontal components of the relative flow velocities $\boldsymbol{U'}_j^H$, moreover, we can calculate the vertical resistance force that is caused by the pure horizontal shear flow (see Eqn. (2.21)). The horizontal flows on a thin filament can induce a vertical force because of the anisotropic character of the filament drag and the asymmetrically curved shape of the filament (see Figure 5BC). In the low Reynolds number flow, the drag (resistance) force of a thin filament depends on the angle of inflow. If the shape of the filament is asymmetric between the upper and lower halves of a filament, the total integrated fluid dynamics forces along the filament are not zero, but should produce a force in either the upward or downward direction. This is analogous with the swimming mechanism of a sperm. A sperm uses the drag anisotropy of a flagellum, when it moves forward. The drag anisotropy provides a force perpendicular to the direction of the local undulatory motion (Lowe 2003, Lauga and Powers 2009). The direction of the force depends on the direction of wave propagation of the undulatory motion (Fung 1990). In this way, a sperm can move forward. The same mechanism may occur passively in a ballooning structure by the asymmetric constraint.

$$\boldsymbol{F}_i = \boldsymbol{\zeta}_{ij}\boldsymbol{U'}_j \text{ with } \boldsymbol{U'}_j = \boldsymbol{U}_j - \boldsymbol{V}_j \tag{2.17}$$

$$\boldsymbol{U'}_j = \boldsymbol{U}_j'^V + \boldsymbol{U}_j'^H \tag{2.18}$$

$$\boldsymbol{F}_i = \boldsymbol{\zeta}_{ij}\left(\boldsymbol{U}_j'^V + \boldsymbol{U}_j'^H\right) = \boldsymbol{F}_i^V + \boldsymbol{F}_i^H \tag{2.19}$$

$$\boldsymbol{F}_i^V = \boldsymbol{\zeta}_{ij}\boldsymbol{U}_j'^V \tag{2.20}$$

$$\boldsymbol{F}_i^H = \boldsymbol{\zeta}_{ij}\boldsymbol{U}_j'^H \tag{2.21}$$

The total forces on the bead spring model is calculated by summating the drag forces on each bead (see Eqns. (2.22) and (2.23)). Once the forces have been calculated, the non-dimensional vertical resistance coefficient of a ballooning structure can then be calculated by dividing the vertical components of forces by the viscosity, settling speed and silk length (see Eqns. (2.24), (2.25) and Figure 4):

$$F_z^V = \sum_i F_{z,i}^V \tag{2.22}$$

$$F_z^H = \sum_i F_{z,i}^H \tag{2.23}$$

$$R_z^V = \frac{F_z^V}{\eta V_z^b L} \tag{2.24}$$

$$R_z^H = \frac{F_z^H}{\eta V_z^b L} \tag{2.25}$$

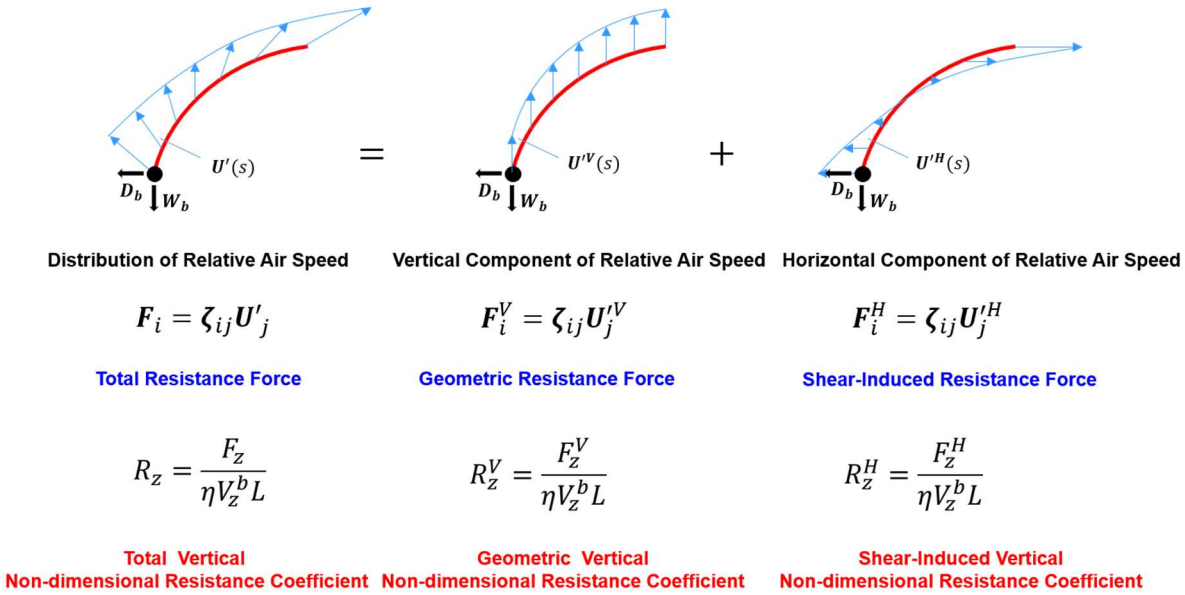

Figure 4. Schematic diagrams showing the decomposition process of the fluid-dynamic forces on the ballooning structure in a shear flow.

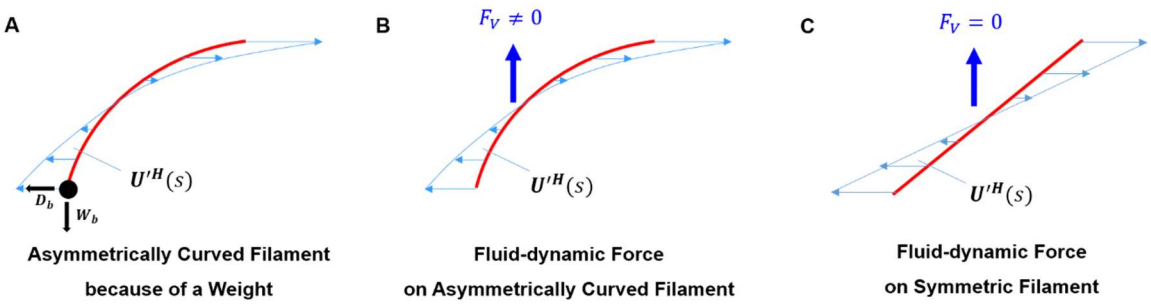

Figure 5. Schematic diagrams of the ballooning structure in a shear flow. (A) Ballooning structure in a shear flow; (B) In the case of an asymmetrically curved filament in a shear flow, the integrated net fluid-dynamic force along the filament is not zero; (C) In the case of a symmetrically curved or symmetric filament in a shear flow, the integrated net fluid-dynamic force along the filament is zero.

2.1.4 Periodic Cellular Flow Model

The periodic cellular flow model is used to study the settling behaviour of a particle (Maxey and Corrsin 1986, Maxey 1987a, Fung 1997, Bergougnoux et al. 2014). The cellular flow field was first used by Stommel to investigate plankton suspension in Langmuir circulation, and has since been frequently used for the study of particle sediment in turbulent flow (Stommel 1949, Maxey and Corrsin 1986, Maxey 1987a, Fung 1997, Bergougnoux et al. 2014). The flow field can be described by means of two-dimensional convection cells (see Figure 6). This flow field is similar with Taylor-Green vortices, but does not decay with time (Taylor and Green

1937). The flow is two dimensional, incompressible and steady and specified by a streamfunction ψ (see Eqn. (5.22)). U_0 and L_c are maximum velocity in the flow field and size of a convection cell, respectively. The velocity field of the cellular flow can be expressed by spatially differentiating the given streamfunction ψ (see Eqns. (5.23) and (5.24)).

$$\psi(x,z) = \frac{U_0 L_c}{\pi} sin\left(\frac{\pi x}{L_c}\right) sin\left(\frac{\pi z}{L_c}\right) \tag{2.26}$$

$$u = \frac{\partial \psi}{\partial z} = U_0 sin\left(\frac{\pi x}{L_c}\right) cos\left(\frac{\pi z}{L_c}\right) \tag{2.27}$$

$$w = -\frac{\partial \psi}{\partial x} = -U_0 cos\left(\frac{\pi x}{L_c}\right) sin\left(\frac{\pi z}{L_c}\right) \tag{2.28}$$

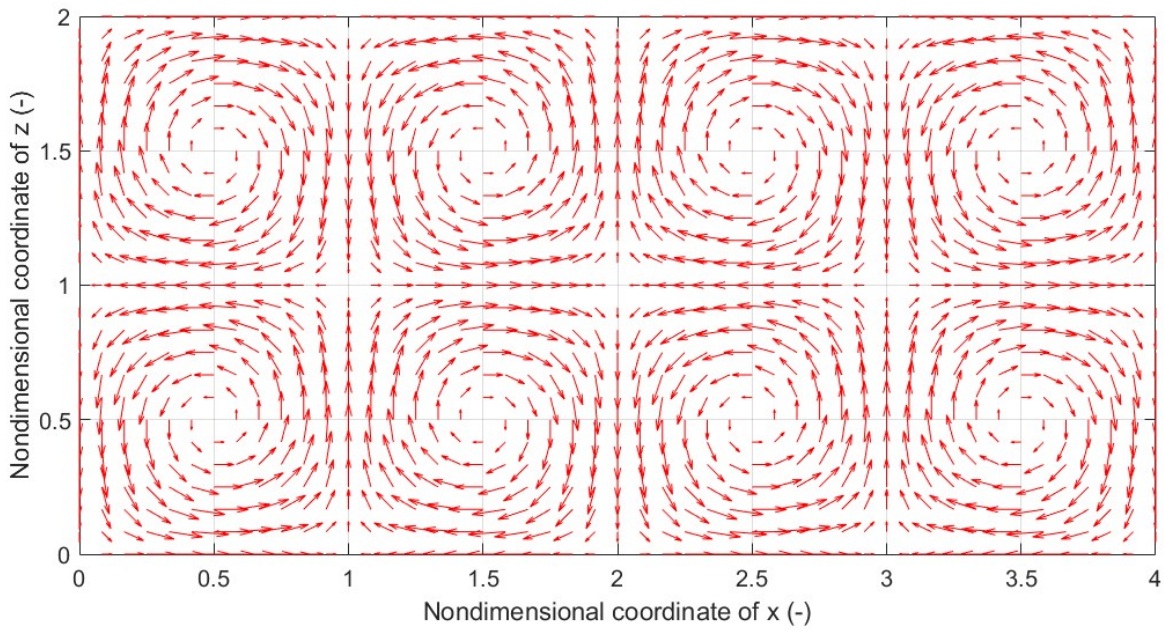

Figure 6. Velocity field of a periodic cellular flow model at $\boldsymbol{U_0 = 1}$ and $\boldsymbol{L_c = 1}$

2.2 Non-dimensional Parameter

In order to consider a wide range of physical scales, we define a non-dimensional parameter, referred to as the 'ballooning number', by comparing the Stokes force on a filament to a gravity force on the weight, i.e. a spider's body at the end of a slender and flexible filament (see Eqn. (2.30)). Here, we do not consider the thickness of the

filament, because the influence of filament thickness on the fluid-dynamic force in a low Reynolds number flow is relatively much smaller than that of filament length. The Stokes force on a filament is described by multiplying the viscosity, characteristic velocity of fluid-flow length of a filament. The gravity force on a weight is defined as the mass of the weight multiplied by a gravity acceleration, 9.8 m/s^2. The characteristic velocity can be defined in various ways according to the flow conditions. For a shear flow, it is defined as the value of the shear rate multiplied by the length of the filament, $U = \gamma L$ (see Eqn. (2.31)). In the case of a cellular flow, moreover, the characteristic velocity is the maximum velocity in the flow, U_0 (see Eqn. (2.32)). For a homogeneous turbulence, the characteristic velocity is the root-mean-square fluctuation velocity, σ (see Eqn. (2.33)):

$$Ballooning\ Number = \frac{Stokes\ force\ on\ a\ filament\ by\ nonuniform\ flow}{Gravity\ force\ on\ a\ body} \tag{2.29}$$

$$Bn = \frac{\eta U L}{(\rho_{body} - \rho_{fluid}) v_{body} g} \tag{2.30}$$

$$Bn_{shear} = \frac{\eta \gamma L^2}{(\rho_{body} - \rho_{fluid}) v_{body} g} \tag{2.31}$$

$$Bn_{vor} = \frac{\eta U_0 L}{(\rho_{body} - \rho_{fluid}) v_{body} g} \tag{2.32}$$

$$Bn_{tur} = \frac{\eta \sigma L}{(\rho_{body} - \rho_{fluid}) v_{body} g} \tag{2.33}$$

2.3 Execution

The motion of the bead-spring model is numerically integrated by using the Euler method. The external flow field influences the motion of the bead-spring model. However, the structure does not affect the flow field. The integration of the simulation in a shear flow is performed until the simulation reaches to the steady state. The execution time for the simulation in a periodic cellular flow and in homogeneous turbulence are defined by comparing the settling speed of the model in the still fluid-medium and the strength of a cellular flow U_0 and the root-mean-square fluctuation velocity of the homogeneous turbulence σ, respectively. The total number of integration time-steps are calculated by equations (2.34), (2.35), (5.38), and (2.37). If the sedimentation is more

dominant than the background velocity fields, the length of a fiber L is divided by the possible smallest sediment velocities of $|V_{z,still} + U_0|$ and $|V_{z,still} + \sigma|$. This time is defined as one time-revolution. In order to collect enough data for the average, 20 times longer period of this one time-revolution is used for the total simulation time ($f_{vor} = 20,\ f_{tur} = 20$). The total number of integration time-steps are acquired by dividing it by the time-step Δt. (see Eqns. (2.34) and (2.36)) If the strength of the background velocity field is more dominant than the sedimentation, the perimeters of a vortex in a periodic cellular flow and the largest eddy in the turbulence, πL_c and $\pi l_{large\ eddy}$, are divided by the possible smallest drift velocities of $|V_{z,still} + U_0|$ and $|V_{z,still} + \sigma|$, respectively. As the same with above, this time is defined as one time-revolution. For the collection of enough data, 20 times longer period of this one time-revolution is used for the total simulation time ($f_{vor} = 20,\ f_{tur} = 20$). The total number of integration time-steps are acquired by dividing it by the time-step Δt. (see Eqns. (2.35) and (2.37))

$$N_{vor} = f_{vor} \frac{L}{|V_{z,still} + U_0|\Delta t} \qquad \text{if } |V_{z,still}| > U_0 \tag{2.34}$$

$$N_{vor} = f_{vor} \frac{\pi L_c}{|V_{z,still} + U_0|\Delta t} \qquad \text{if } |V_{z,still}| < U_0 \tag{2.35}$$

$$N_{tur} = f_{tur} \frac{L}{|V_{z,still} + \sigma|\Delta t} \qquad \text{if } |V_{z,still}| > \sigma \tag{2.36}$$

$$N_{tur} = f_{tur} \frac{\pi l_{large\ eddy}}{|V_{z,still} + \sigma|\Delta t} \qquad \text{if } |V_{z,still}| < \sigma \tag{2.37}$$

3 Results

3.1.1 Homogeneous Turbulence

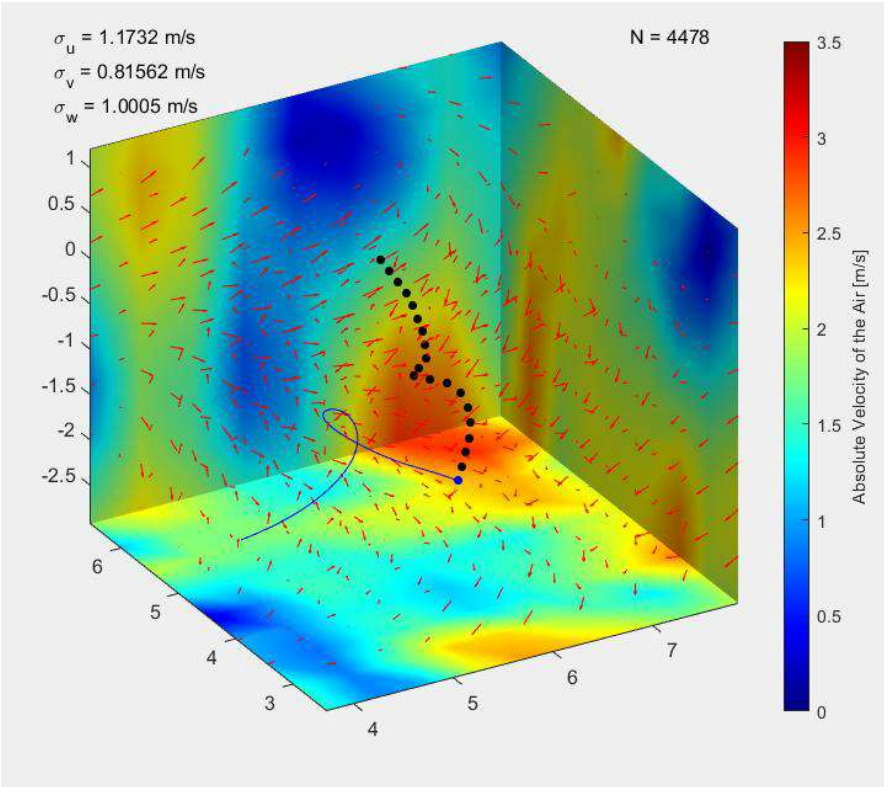

Figure 7. Simulation of the filament-like structure in the homogeneous turbulence. The bold points describe the bead-spring model. The blue point is the bead on which the point mass is applied. The blue solid line is the trajectory of the point mass. The colour bar represents absolute velocities of the flow. σ_u, σ_v, σ_w denote the standard deviations of the x, y, z components of velocity until n-th iteration.

Spiders fly passively in chaotic air currents. Accordingly, the influence of the homogeneous turbulence on the spider fibre is explored using the bead-spring model. The dimensionless mean settling velocities for different ballooning numbers are presented in Figure 8. As the strength of flow fluctuation becomes more dominant, the ballooning structure exhibits a slow settling character (see Figure 8). There are two reasons for the scatter at high ballooning numbers. First, as the ballooning number increases, the settling speed of the ballooning structure in the still air becomes smaller because of its light weight, which is used for the nondimensionalisation of the settling speed. Therefore, the scatter of the nondimensionalized settling speed is amplified at the high ballooning numbers. Second, the finite number (n=10) of Fourier modes in the turbulent model is limited to describe an isotropic homogeneous turbulence. Each experimental simulation has a different turbulent structure.

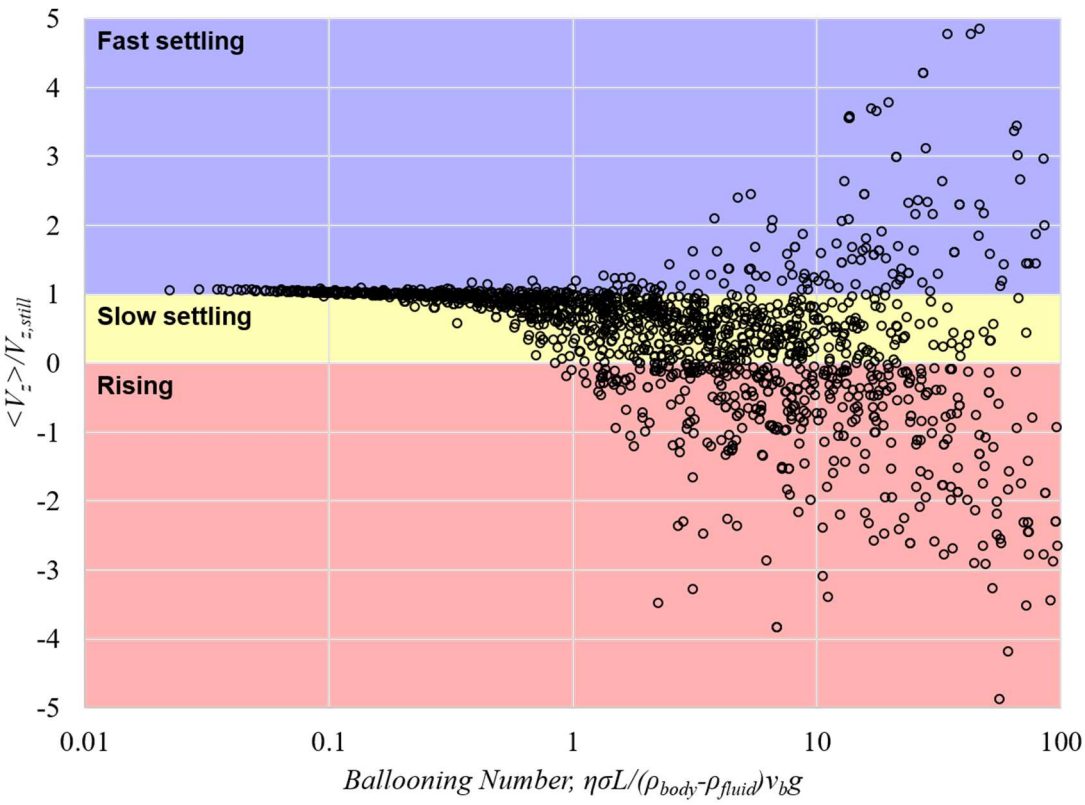

Figure 8. Dimensionless settling speed distribution of the ballooning structure in the homogeneous turbulence model according to the ballooning number. Total 1400 cases of combination of the parameters are simulated and the averaged settling speeds are plotted. Fast settling: the structure falls faster than it would in still air. Slow settling: the structure falls slower than it would in still air. Rising: the structure does not fall, but rises upward.

An end-to-end vector, $\overrightarrow{R_e}$, represents the statistical shape of the ballooning structures during their suspension in turbulence (see Figure 9E). The averaged z component of the end-to-end vector approximates 1 as the ballooning number decreases (see Figure 9AB and Appendix A Figure C (f)). The value scatters either near or around 0 as the ballooning number increases (see Figure 9AD).

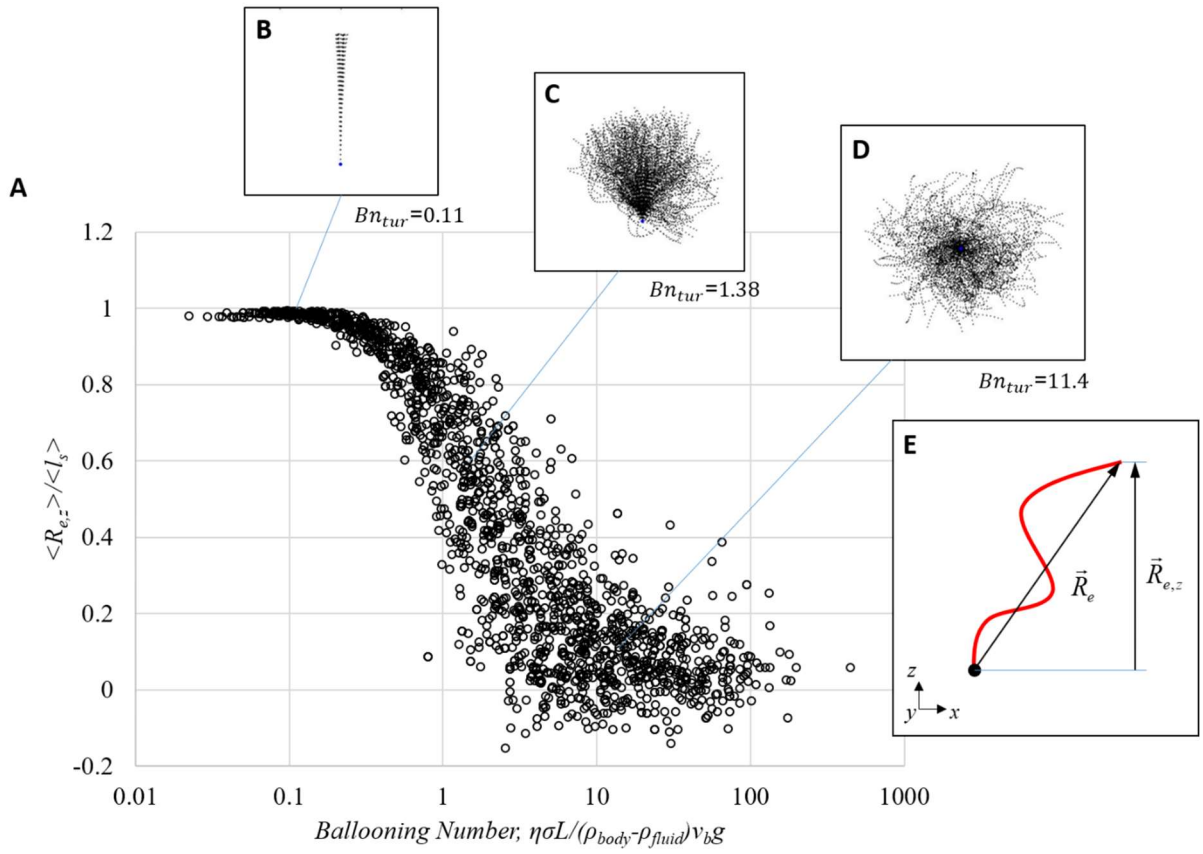

Figure 9. Distribution of the mean vertical (z-direction) components of end-to-end vectors according to the ballooning number for homogeneous turbulence. Total 1400 cases of combination of the parameters are simulated.

3.1.2 Shear Flow

The vertical velocity difference in a shear flow deforms the filament structure in its sedimentation. As the shear rate increases, the deformation becomes larger and the deformed geometry in the shear flow effects on the sediment velocity of the structure (see Figure 10 and Figure 11). The influence of strength of the shear flow on the sedimentation is universally investigated by introducing the non-dimensional parameter of the "ballooning number" (see Eqn. (2.31)) and applying various compositions of the parameters e.g. viscosity of the medium, shear rate of the flow, length of the filament and weight of the point mass.

3.1.2.1 Influence of Anisotropic Drag

The influence of the anisotropic drag is studied by comparing two results: namely, those with and without hydrodynamic interaction. The settling speed of a ballooning structure is non-dimensionalised by the settling speed of the same structure in still conditions (i.e. zero shear rate). Therefore, the dimensionless settling speeds, which are above 1, indicate fast falling (faster than the settling speed in still medium), while the dimensionless settling speeds, which are below 1, indicate slow settling events caused by shear flow. As the dimensionless shear

rate (ballooning number for shear flow, Bn_{shear}) increases, the ballooning structure stretches horizontally (see Figure 10) and the settling speed is reduced. These results are not seen in cases in which the hydrodynamic interaction is ignored (considering the isotropic drag of a fibre) (see Figure 11). The settling speed is reduced by 40% at the high ballooning number (Bn_{shear}=1000).

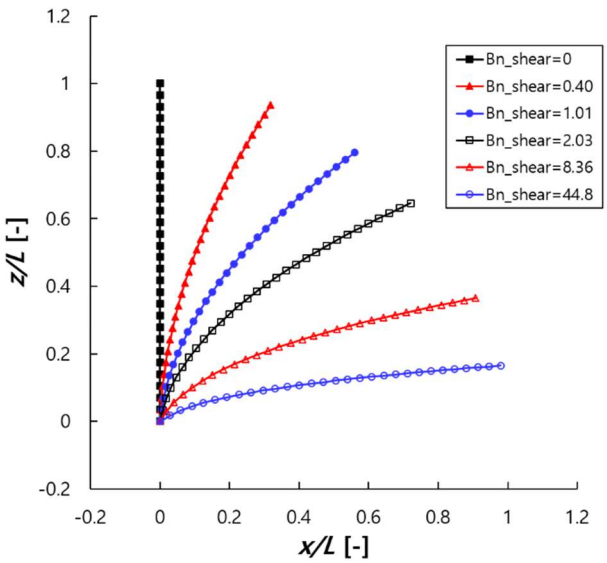

Figure 10. Shapes of a filament in various strengths of a shear flow (various ballooning numbers).

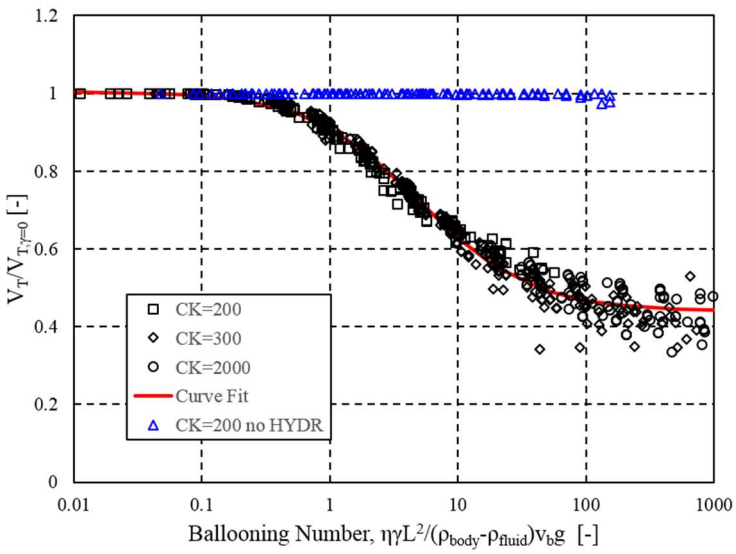

Figure 11. Variation of dimensionless settling velocity of the ballooning structure in a shear flow with variation of the ballooning number. Black marks (720 cases) indicate the cases with hydrodynamic interaction (considering the anisotropic drag of the filament), while blue marks (138 cases) are the cases without hydrodynamic interaction (considering the isotropic drag of the filament). CK refers to the spring constants between beads.

3.1.2.2 Cause of Reduction of the Settling Speed

The parameter most associated with settling speed is the resistance coefficient of the object. The resistance coefficient of a filament-like object is expressed by a vertical drag force divided by the settling speed and the length of the filament.

$$K_z = \frac{F_z}{V_z L} \tag{3.1}$$

To elucidate the causes of the reduction of the settling speed, the nondimensional resistance coefficient is decomposed into geometric (see Eqn. (2.24)) and shear-induced (see Eqn. (2.25)) nondimensional resistance coefficients (see Figure 4).

The variation of the dimensionless resistance coefficient is presented in Figure 12. As the ballooning number increases, so too does the total nondimensional resistance coefficient. This coincides with the fact that the nondimensional settling speed decreases as the ballooning number increases (see Figure 11). The increase of the nondimensional resistance coefficient at the beginning, $0.1 < Bn_{shear} < 3$, is mostly caused by the geomeric shape of a filament, which is stretched horizontally and falls in a transverse attitude (see red triangular marks in Figure 12). At ballooning numbers over 3, the increase of the nondimensional resistance coefficient is caused by a shear flow (see blue circular marks in Figure 12).

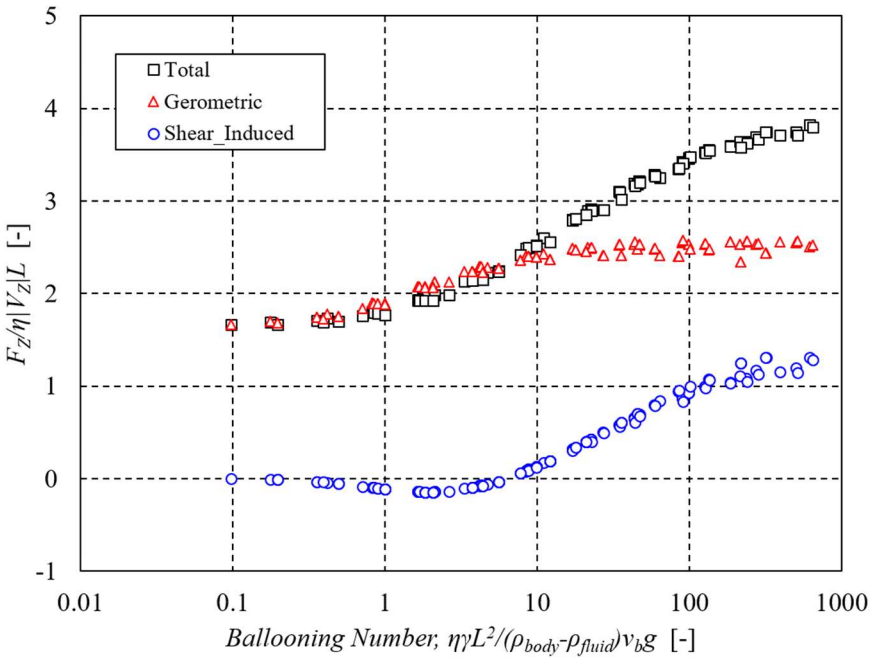

Figure 12. Variation of dimensionless resistance coefficients with the ballooning number for a shear flow. The dimensionless resistance coefficient is decomposed into geometric coefficient and shear-induced coefficient. Total 128 cases for different ballooning numbers are simulated.

3.1.3 Vortex Field

The ballooning structure exhibits various behaviours in a cellular flow field. According to the size and strength of the vortices, the ballooning structure exhibits the following motions: (i) 'vortex crossing'; (ii) 'fast settling'; (iii) 'slow settling'; and (iv) 'vortex trapping'. At low ballooning numbers ($Bn_{vor} < 2$), the ballooning structure falls crossing the vortices. The influence of flow eddies on their settling speed are small; therefore, their dimensionless settling speeds are around 1 ($0.9 \leq \langle V_{z,last} \rangle / V_{z,still} < 1.1$, see Figure 13, Figure 15 (a)(d)(f), and Appendix C Figure C 8Figure C 13). As the ballooning number increases, the motions split into three different behaviours. The split depends on the size of the vortices and the initial positions. If the sizes of the eddies are under 1.2 times the silk length, the ballooning structure falls faster than it would in still air (see Figure 13, Figure 14, Figure 15 (e)(h)(i) and Appendix C Figure C 14Figure C 17, Figure C 20Figure C 23); if the eddies are larger than 1.2 times the silk length, however, the ballooning structure falls slower than it would in still air (see Figure 13, Figure 14 and Figure 15 (b)). At higher ballooning numbers, the ballooning structure is trapped by an eddy and the mean settling speed approaches zero (see Figure 13, Figure 14 and Figure 15 (c)(f); see Appendix C Figure C 18Figure C 19 and Figure C 24Figure C 29).

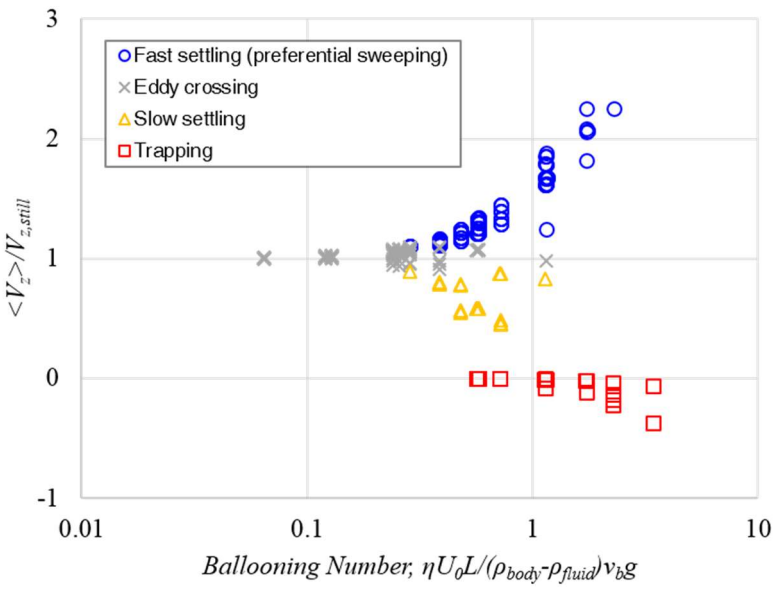

Figure 13. Dimensionless settling speed of a ballooning structure in a cellular vortex (eddy) field versus ballooning number. If the settling behaviour converges to a periodic motion, the dimensionless settling velocity of the last two periodic motions is averaged as a representative value.

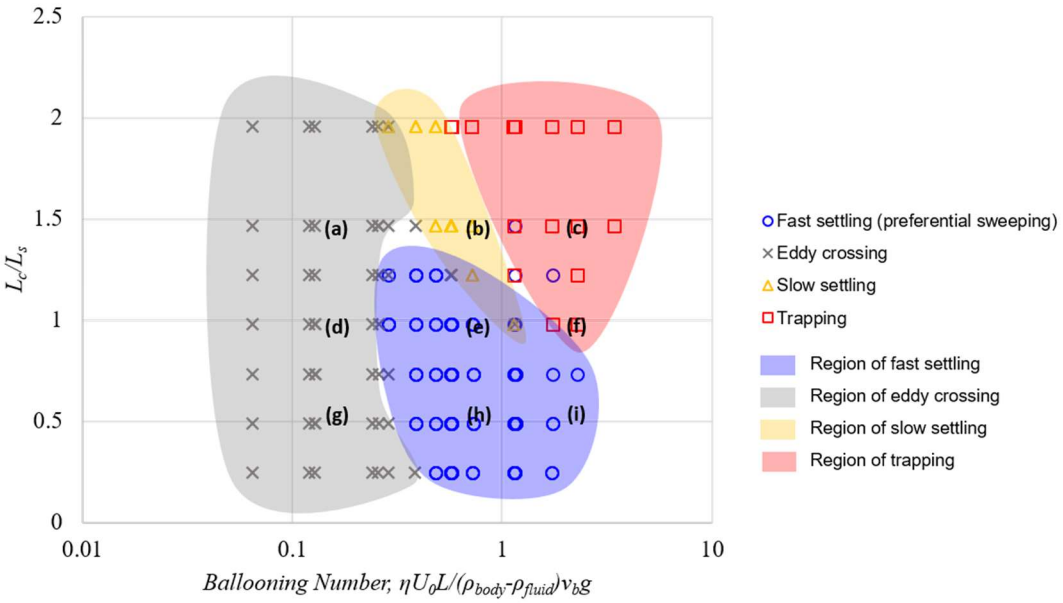

Figure 14. Different behavioural modes according to eddy size and ballooning number. The behavioural modes are categorized by the motion and settling speed of the structure. 'Eddy crossing' is the mode in which their dimensionless settling speeds are between 0.9 and 1.1; 'slow settling' is where speeds are slower than 0.9; 'fast settling' is the mode that falls faster than 1.1. The 'trapping motion' is recognised by detecting the averaged settling speed of 0 (or near 0).

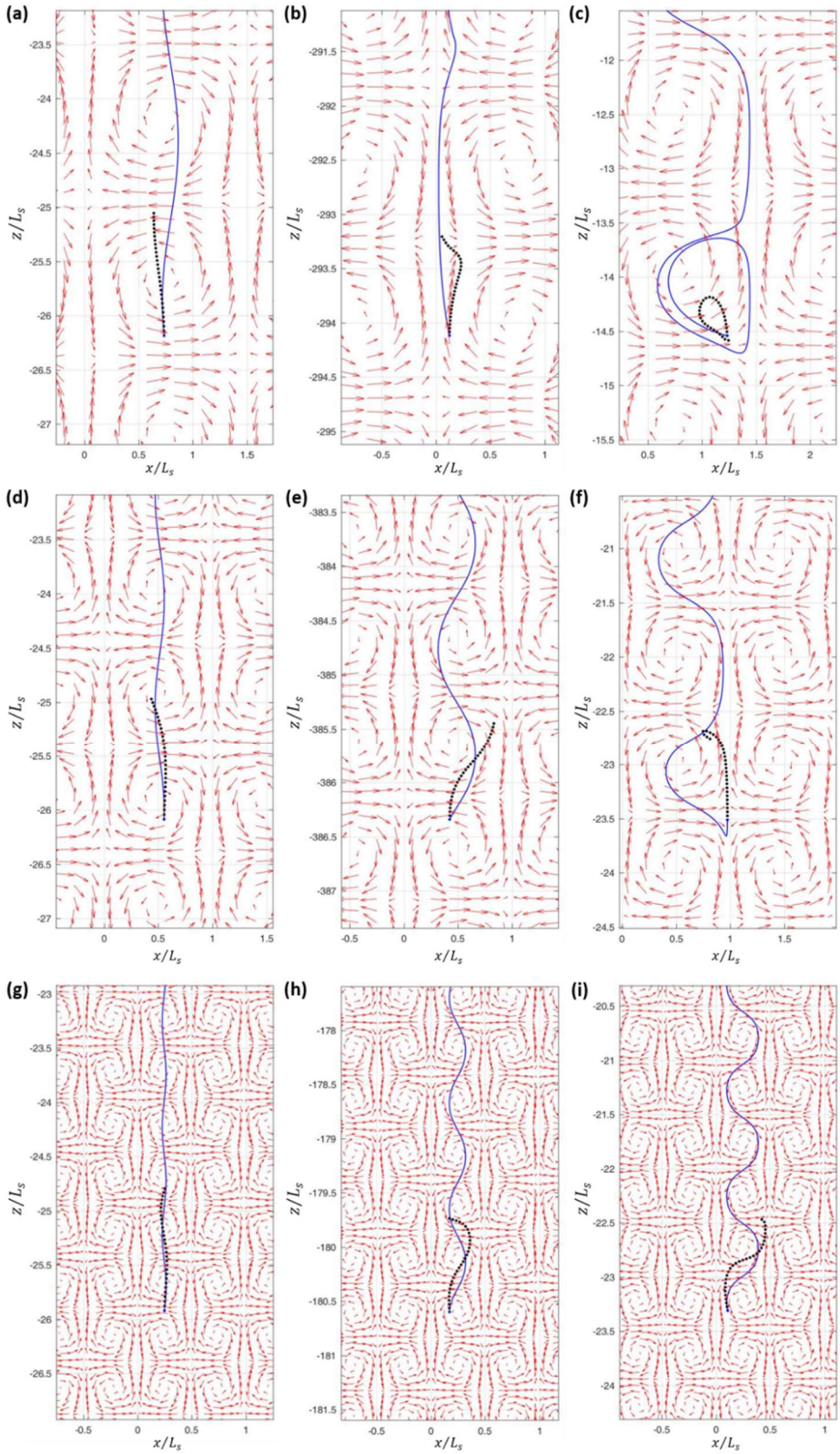

Figure 15. Trajectory of the ballooning structure in a cellular vortex field. (a)(d)(g) Eddy crossing: the ballooning structure falls crossing the eddies; (b) Slow settling: the ballooning structure stays between two vortex columns and falls slower than the structure in still air; (c)(f) Trapping: the ballooning structure is trapped by a vortex after a few or many periodic sediment motions; (h)(i) Fast settling (preferential sweeping): the ballooning structure deforms and passes through a curved high strain path, and the structure falls faster than it would in still air.

Some interesting features emerging from these results include the fact that the ballooning structure is preferentially trapped by a vortex in certain flow conditions (high ballooning number and in large vortex cells). The structures travel downwards through the high-strain region between vortices; then, after a few oscillations in sediment progress, the structure becomes trapped in a vortex (see Appendix C: Figure C 24Figure C 26Figure C 28). The distances travelled by sediment before the trapping events depend on its initial positions, where those are released (x direction). However, at the end, all structures were trapped in a vortex. This suggests that a biased character exists in the suspension of the ballooning structure in vortex fields: namely, the ballooning structure is preferentially trapped by a vortex at high ballooning numbers. Moreover, two trapping motions can be observed in the events: cycling trapping, which shows a closed loop trajectory of the body (see Figure 16A), and stationary trapping, which converges to the equilibrium states in the position and shape of the filament (see Figure 16B).

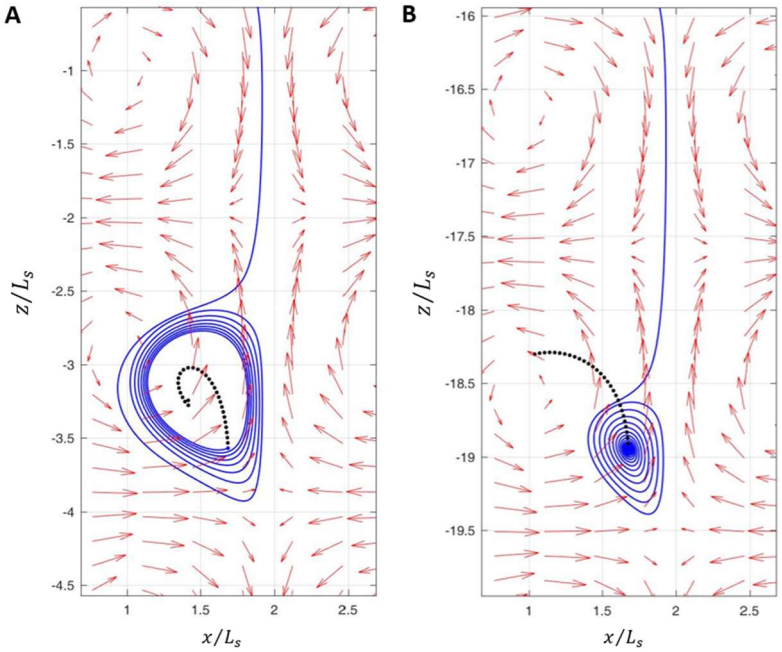

Figure 16. Two different trapping modes in a cellular vortex field. (A) Cycling trapping building a closed loop; (B) Stationary trapping remaining in an equilibrium state.

3.1.4 Energy Extraction from the Turbulent Flow

The sediment behaviour of a ballooning spider is compared with a point-like parachuter, which represents dandelion and thistle seeds. The size of the point-like parachuter is adjusted to give it the same settling speed as the ballooning spider (see Figure 17); therefore, both structures have the same weights and settling speeds in still air. Both are released from identical locations in the identical turbulence model.

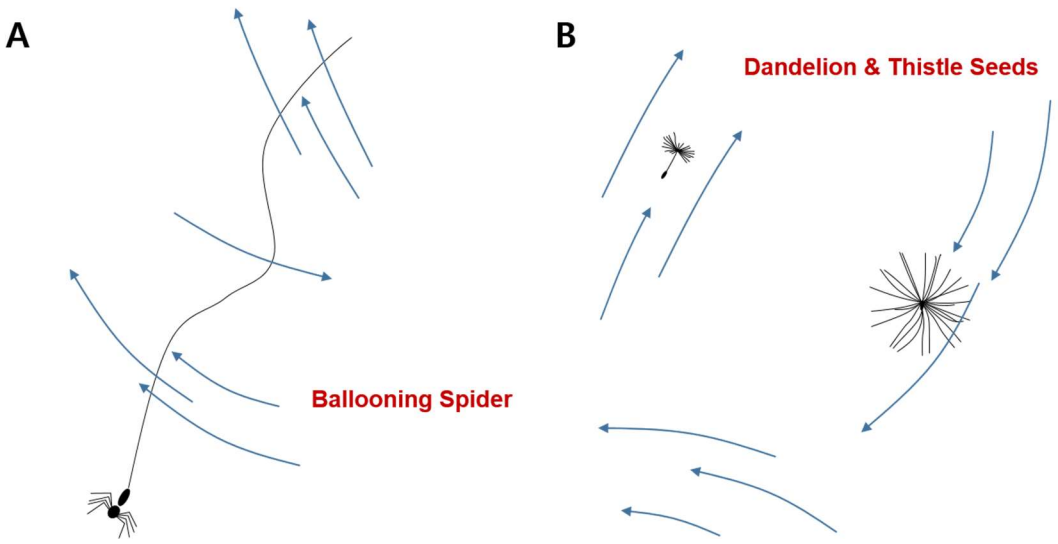

Figure 17. Comparison between the flight of a ballooning spider and the flight of a dandelion (or thistle) seed. (A) Sketch of a spider's ballooning; (B) Sketch of the flight of dandelion and thistle seeds.

While the point like-parachuter showed a mirror-symmetric distribution about $\langle V_z \rangle / V_{z,still} = 1$ (see Figure 18C), the filament-like parachuter showed a biased distribution about $\langle V_z \rangle / V_{z,still} = 1$ (see Figure 18A). To reduce the scattered distribution at high ballooning numbers, both sediment speeds are nondimensionalised by the root-mean-square fluctuation velocity $\sigma = \sqrt{\overline{\boldsymbol{u}'(t)^2}} = \sqrt{(1/3)\overline{\left(u'^2 + v'^2 + w'^2\right)}}$. The dimensionless settling speeds for the ballooning structure exhibit a wider distribution (Figure 18B) compared with those (Figure 18D) for the point-like parachuter. For ease of comparison, both sets of data are plotted in one chart (see Figure 18F). The red points are the biased plots of the filament-like parachuter (the data of a point-like parachuter are plotted on the data of a filament-like parachuter; see Figure 18EF). The dimensionless settling speeds for the filament-like parachuter are biased to the region where the structure falls slower than it would in still air, or sometimes even the rising region. Figure 19 clearly shows the biased motion of the filament-like parachuter in comparison with the point-like parachuter.

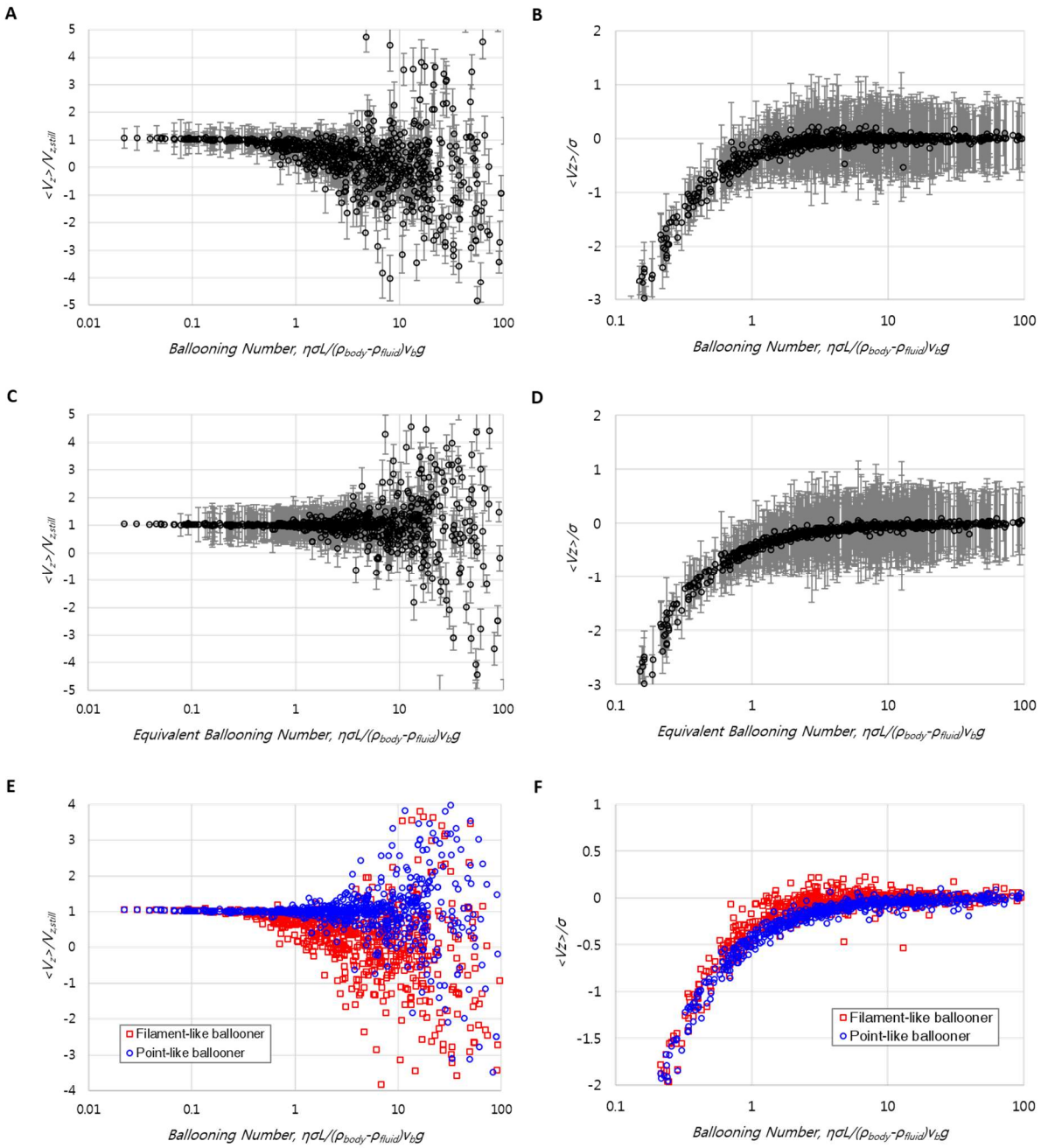

Figure 18. Comparison between a filament-like parachuter and a point-like parachuter under dimensionless settling speed. Total 750 cases are simulated and the averaged settling speeds with their standard deviations are plotted. (A) Dimensionless settling speed (divided by the settling speed in the still medium) of a filament-like parachuter in homogeneous turbulence; (B) Dimensionless settling speed (divided by the root-mean-square fluctuation velocity) of a filament-like parachuter in homogeneous turbulence; (C) Dimensionless settling speed (divided by the settling speed in the still medium) of a point-like parachuter in homogeneous turbulence; (D) Dimensionless settling speed (divided by the root-mean-square fluctuation velocity) of a point-like parachuter in homogeneous turbulence; (E) Comparison of dimensionless settling speeds (divided by the settling speed in the still medium) between filament-like and point-like parachuters in homogeneous turbulence; (F) Comparison of dimensionless settling speeds (divided by the root-mean-square fluctuation velocity) between filament-like and point-like parachuters in homogeneous turbulence.

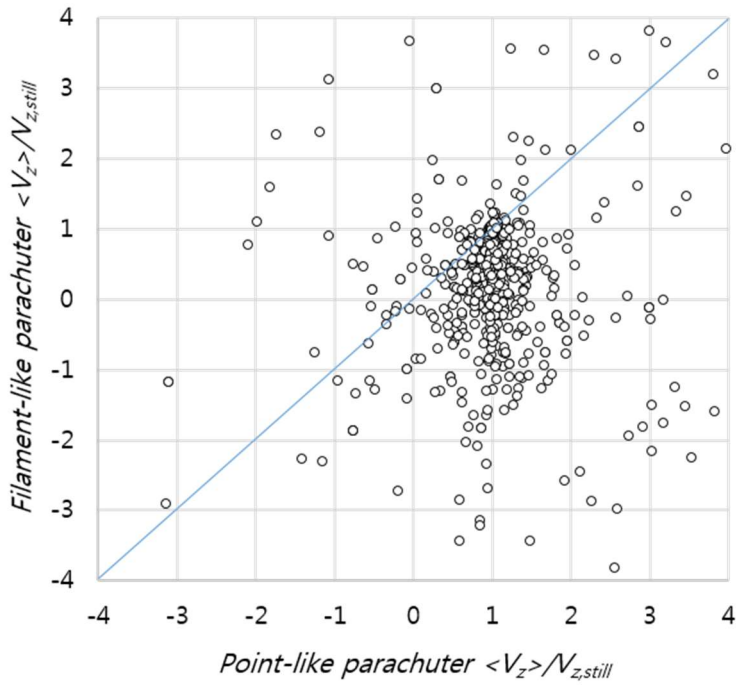

Figure 19. Simultaneous plot of the dimensionless settling speeds for a filament-like parachuter and a point-like parachuter. Both cases are simultaneously simulated in an identical turbulence model.

The characteristics of the shape of the ballooning structure can be described by averaging the radius of gyration of the filament during the event. Eqns. (3.2) and (3.3) are used for the lower and upper half parts respectively. $R_{g_{lower}}$ and $R_{g_{upper}}$ indicate the radiuses of gyration for the lower and upper halves of the filament. l_s and $l_{s,mid}$ refers the length of the filament and its half. $\boldsymbol{r}$ and $\boldsymbol{r}_{mid}$ are a position vector and its middle position vector of the filament.

$$R_{g\,lower}^2 = \frac{\int_0^{l_{s,mid}} (\boldsymbol{r} - \boldsymbol{r}_{mid})^2 ds}{\int_0^{l_{s,mid}} ds} \tag{3.2}$$

$$R_{g\,upper}^2 = \frac{\int_{l_{s,mid}}^{l_s} (\boldsymbol{r} - \boldsymbol{r}_{mid})^2 ds}{\int_{l_{s,mid}}^{l_s} ds} \tag{3.3}$$

At the very small ballooning number $Bn_{tur} = 0.02$, both dimensionless squared radiuses of gyration are around 0.33, $\langle R_{g\,lower}^2 \rangle \approx \langle R_{g\,upper}^2 \rangle \approx 0.33$, meaning that the shapes of both filaments are similar (resembling a straight line; see Appendix C: Figure C 2 (f)). As the ballooning number increases ($0.1 \leq Bn_{tur} < 10$), the dimensionless squared radius of gyration of the lower half part of the filament is larger than that of the upper half part. This means that the upper part of the filament is more curved than the lower part (see Figure 20 and Appendix C: Figure C 2 (c)(d)(e)). At high ballooning numbers ($10 \leq Bn_{tur} < 100$), the differences are small and both squared

radiuses of gyration are reduced (see Appendix C: Figure C 2 (a)(b)). This tendency can be seen more clearly in Figure 21.

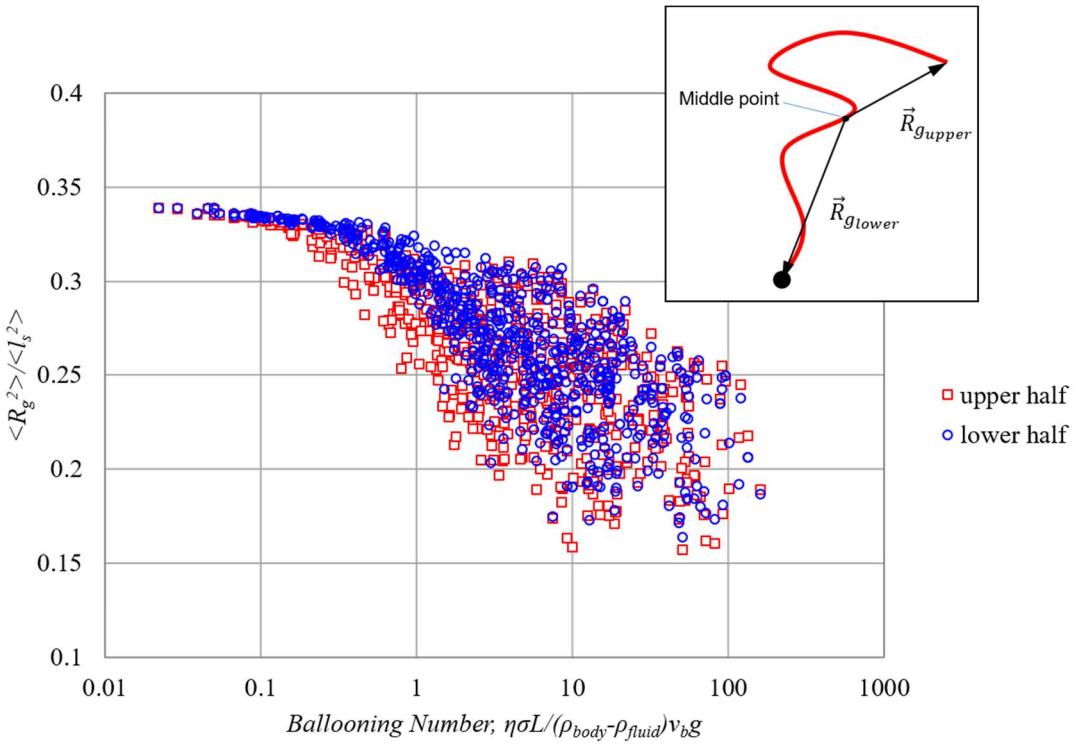

Figure 20. Distribution of the dimensionless mean square value of the upper half and lower half radiuses of gyration according to the ballooning number for homogeneous turbulence.

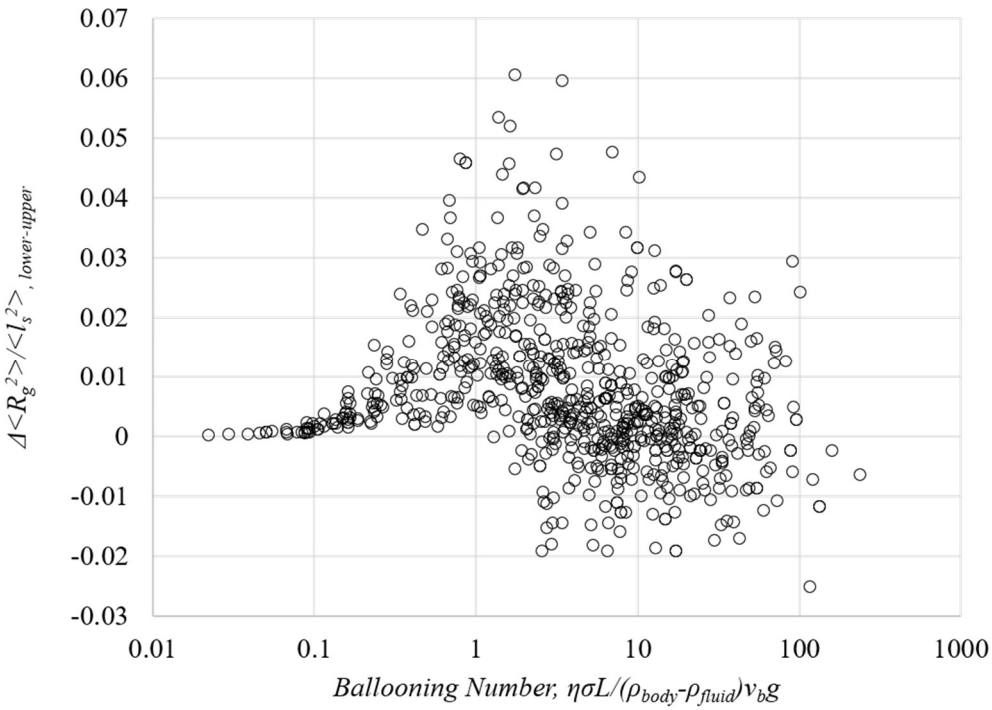

Figure 21. Distribution of the difference of the dimensionless mean square values between the upper half and lower half radiuses of gyration according to the ballooning number for homogeneous turbulence.

4 Discussion

4.1.1 Role of Anisotropic Drag of a Filament

The anisotropic drag of a thin filament structure is a crucial aspect of the dynamics of a microswimmer. The cilia and flagella of a microswimmer enable organisms and cells to move forward in a viscous medium (Purcell 1977, Brennen and Winet 1977, Fung 1990, Happel and Brenner 1991, Lauga and Powers 2009). In the low Reynolds number flow, the perpendicular drag on a filament is about twice larger than its tangential drag. Because of this drag anisotropy, a flagellum can slip in a certain direction in a viscous fluid and can also regulate the fluid-dynamic force on it by deforming its shape for the locomotion of a microswimmer. This character of the anisotropic drag is valid not only in the active dynamics of a swimming microorganism, but also in the passive dynamics of an artificial microswimmer, such as a flexible magnetic filament in an oscillating external magnetic field (Dreyfus et al. 2005, Gauger and Stark 2006). From this, we may infer that the anisotropic drag is also an important factor in the passive dynamics of a flexible filament moved by an external fluid flow.

In the simulation, the influence of the anisotropic drag is checked by releasing the ballooning structure in various shear flow strengths. In the bead-spring model, the drag anisotropy is described by the Rotne-Prager hydrodynamic interaction between beads (Rotne and Prager 1969, Dhont 2003, Gauger and Stark 2006). The drag anisotropy modelled by the hydrodynamic interaction was shown in Appendix A Figure A 1 and compared with the experimental data. The velocity reduction of the ballooning structure in a shear flow shows that the reduction

is due to the drag anisotropy; this is because the model without hydrodynamic interaction did not exhibit any velocity reduction effect during sedimentation in a shear flow (see Figure 11).

The main cause of reduction of the settling speed in a shear flow is its geometrical shape of a filament concerning with the anisotropic drag. However the geometric contribution reaches maximum at the ballooning number of 10. After that the reduction of the settling speed is caused by the shear-induced resistance coefficient (see Figure 12).

Particle sedimentation has been widely studied in physics: for example in a fluctuating fluid (Boyadzhiev 1973), in a cellular flow field (Maxey and Corrsin 1986, Maxey 1987a, Fung 1997, Bergougnoux et al. 2014), and in an isotropic turbulence (Snyder and Lumley 1971, Riley 1974, Reeks 1977, Well and Stock 1983, Maxey 1987b, Squires and Eaton 1990, 1991, Wang and Maxey 1993). Some studies have observed retardation of the settling velocity (Snyder and Lumley 1971, Well and Stock 1983, Squires and Eaton 1991, Stout et al. 1995, Fung 1998), while others have observed fast falling (Maxey 1987b, Fung 1997, 1998). It was later found that the retardation is caused by the nonlinear drag of the heavy particles in the range of Reynolds number $1 < Re < 5000$ (Stout et al. 1995, Fung 1998). The fast falling is caused by the inertia of a particle, which induces the particles toward regions of downdraft path, rather staying in a vortex (Maxey 1987b, Fung 1997, 1998). This increases the settling speed of a particle in comparison with the same particle settling in a still medium. In line with these previous studies on particle sedimentation, the present work finds that the observed nonlinearity, which retards the settling speed of a spider, is due to the anisotropic drag of their flexible filament in nonuniform flows.

4.1.2 Trapping Phenomenon by a Vortical Flow

The simulation in a cellular vortical flow field reveals various motions according to the flow conditions (see Figure 16). In the simulation, two flow condition parameters are considered: the size L of a vortex, and the strength (vortex velocity U_0) of the vortex. In a previous study of particle sedimentation, Stout et al. (1995) categorised three regimes of heavy particle motion in turbulent flow (see Figure 22): (i) suspension for $\sigma/W_T \gg 1$ (Stommel 1949, Manton 1974); (ii) preferential sweeping for $\sigma/W_T \approx 1$ (Maxey and Corrsin 1986, Maxey 1987b, Wang and Maxey 1993, Fung 1997, 1998, Toschi and Bodenschatz 2009, Balachandar and Eaton 2010); (iii) eddy crossing for $\sigma/W_T \approx 1$ (Stout et al. 1995; see Figure 22). The ballooning structure in a cellular flow field exhibited similar behaviours to particle motions in the turbulent flow (Maxey and Corrsin 1986, Maxey 1987a, Stout et al. 1995, Fung 1997, Bergougnoux et al. 2014). The eddy crossing motion of the ballooning structure in Figure 13 and Figure 15(a)(d)(g) is similar to the eddy crossing motion of the heavy particle (see Figure 22(a)). If the point mass of the ballooning structure is heavy enough compared with the resistance force applied to a filament by the eddies, the structure crosses eddies (vortices) in a cellular flow field, and there is no retardation of the settling speed. However, if the mass is comparable to the resistance force on a filament, then the fast settling motion of the ballooning structure in Figure 13 and Figure 15(e)(h)(i) is very similar to the preferential sweeping motion in Stout's theory of heavy particle motion (see Figure 22(b)). The ballooning structure is preferentially swept into the regions of the downdraft path (Maxey 1987, Stout et al. 1995). This preferential sweeping of the heavy particle is caused by its inertia. However, as the present simulation does not consider the inertia of the point mass, the preferential sweeping of the ballooning structure may thus be caused by the

anisotropic drag of a filament structure. If the vortex velocity is dominant and the vortex is large, the ballooning structure is trapped by the vortex (see Figure 15(c)(f)). This is very interesting, because the heavy particle does not settle down with the help of a filament. Although the ballooning structure produces negative buoyancy (toward a ground) because of its weight, the ballooning structure either stays in the upward current region of a vortex (see Figure 16B) or gains energy by cycling with a passive motion (see Figure 16A). This trapping motion was also observed by Zhao et al. (2017), who simulated the structure in a cavity flow.

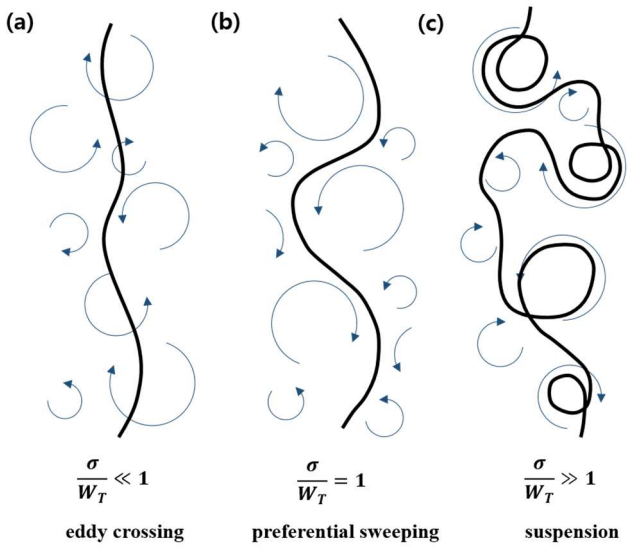

Figure 22. Three different regimes of heavy particle motion (redrawn from Stout el al. 1995)

Abundant turbulent eddies exist in the atmospheric boundary layer. These are mostly produced (i) by mechanical terrains on the Earth's surface, (ii) by rising thermal air parcels, and (iii) by the shear-winds on the surface. These eddies mostly develop upwards, as they draft with winds, because of the blockage by the ground (Adrian et al. 2000, Hunt and Morrison 2000, Hommema and Adrian 2003, Adrian 2007, Finnigan et. al 2009). These upward developing eddies, which have certain sizes and strengths, may be helpful to the ballooning spiders by trapping them and allowing them to stay in the air for longer periods.

4.1.3 Biased Behaviour in a Homogeneous Turbulence

As previously discussed (see Sections 4.1.1 and 4.1.2), a thin filament structure (spider silk) shows a nonlinear drag character on a point mass (spider) in a non-uniform flow. In a simple shear flow, the ballooning structure settles slower than it would in a still medium. In a cellular flow field, the same structure settles faster in small-size and relatively strong vortex cells, while either moving slower or becoming trapped in large-size and relatively strong vortex cells. This nonlinear character in homogeneous turbulence also results in a biased settling behaviour (biased toward slow settling) of the structure (see Figure 8). Reynolds et al. (2006) first proposed that turbulent wind may reduce the rate of fall of the spider by deforming and stretching the flexible fibres. Their study points out that the extensibility and flexibility of a filament may be the causes of the settling retardation. However, as previously discussed in Sections 4.1.1 and 4.1.2, the cause of the settling retardation seems to be the anisotropic

drag character of a thin filament and flexible deformation in vortex eddies in turbulence. As the model (extendible and flexible filament) proposed by Reynolds et al. did not consider the hydrodynamic interaction between beads (Rouse model; Rouse 1953, Dhont 2003, Reynolds 2006, Doi and Edwards 2007), the cause of the retardation in Reynolds' simulation seems to be flexibility (not extensibility), which helps the filament to become deformed and trapped in a quasi-vortical flow in the turbulence model.

Ballooning silks have a longer length-scale (i.e. a few metres) compared to an aerial seed (a few centimetres) (Sudo et al. 2008, Cho et al. 2018). Therefore, each segment of the ballooning silk is exposed to different wind flow fields in direction and magnitude. By contrast, an aerial seed is exposed to quasi-uniform airflow, although it still drifts in the fluctuating winds (see Figure 17). Accordingly, the question is whether the exertion of these non-uniform flows on the ballooning silk generates extra buoyancy capability during a ballooning flight. To clarify this, the behaviour of a filament-like parachuter under homogeneous turbulence was compared with that of an equivalent point-like parachuter (adjusted so that both have the same settling speed in a still medium) in the identical turbulent flow. As shown in Figure 18, the filament-like parachuter evidently shows biased behaviour towards either slow settling (in comparison with that of the point-like parachuter) or rising (see also Figure 19). This biased behaviour may be induced by the different (eccentric) characters of filament segments: The free-moving end easily drifts with the wind flows (Free tip condition: Leclereq and Langre 2018), while the point-mass-attached end is constrained by gravity. The segment right above the point-mass mostly stays vertical because of the weight constraint. This statistical difference is elucidated in Figure 20 by comparing the radiuses of gyration of the upper and lower parts. The result is reasonable: at low ballooning numbers $Bn_{tur} < 0.1$, the settling behaviour is dominant, such that the shape of the filament is vertically straight and there is no difference in the radius of gyration. However, at moderate ballooning numbers $0.1 < Bn_{tur} < 10$, the radius of gyration of the lower half segment is larger than that of the upper half segment, because the upper half segment can be more easily deformed by the turbulent flow. At high ballooning numbers $Bn_{tur} > 10$, the turbulent flow is dominant; therefore the shape of the filament is almost randomly distorted, and there is statistically no difference in the radius of gyration between the upper and lower half segments (see Figure 21 and Appendix C: Figure C 2). As discussed in Sections 4.1.1 and 4.1.2, this biased behaviour seemed to be induced by both the anisotropic drag of a filament and the vortical flows in homogeneous turbulence.

4.1.4 The Ballooning Number

Spiders' ballooning can be understood as a physical phenomenon in which two different physical scales are connected: the macroscopic weight of the spider, although insects of such size normally utilise a high Reynolds number flow for their flight, is sustained by the micro-fluid-dynamic forces that are harvested through the use of long thin fibres (see Figure 23). The physical properties of these two different scales are non-dimensionalised and expressed as the ballooning number (see Eqns. (2.30)-(2.33)). An increase in the ballooning number means that the fluid-dynamic forces exerted on a silk by the non-uniform flow become dominant compared with the force of gravity that acts on the body. Moreover, a decrease in the ballooning number means that the gravity force on the body becomes more dominant than the fluid-dynamic forces on a silk, meaning that the spider will fall like a heavy particle, cutting through the eddies of the air flow.

The characteristic velocity refers to the intensity of a non-uniform flow. In the case of the turbulent air, the root-mean-square fluctuation velocity is the characteristic velocity. If we assume that a spider flies in a 1.96 m s^{-1} mean wind speed (measured data 0.95 m above the ground), the root-mean-square fluctuation velocity is 0.41 m s^{-1} on a sunny and light breeze day. Thus, the ballooning number of a 20 mg crab spider for turbulence in the field may be about 7.42 (see Eqn. (4.1); dynamic viscosity of air: 1.837×10^{-5} kg m^{-1} s^{-1}; length of a spider silk: 3.22 m; number of silks: 60). This number belongs to the regime in which the behaviour of the ballooning structure is biased (towards slow settling in the turbulence; see Figure 8). The observed shapes of the ballooning silks in the field is also believed the events in the range of the ballooning number $1 < Bn_{tur} < 10$ (Cho et al. 2018). The superposed shapes of these ballooning silks in the field are compared with the results of the bead-spring model simulation (see Figure 24). As Figure 24 shows the geometric analogy the introduction of the ballooning number in the spiders' flight seems to be reasonable.

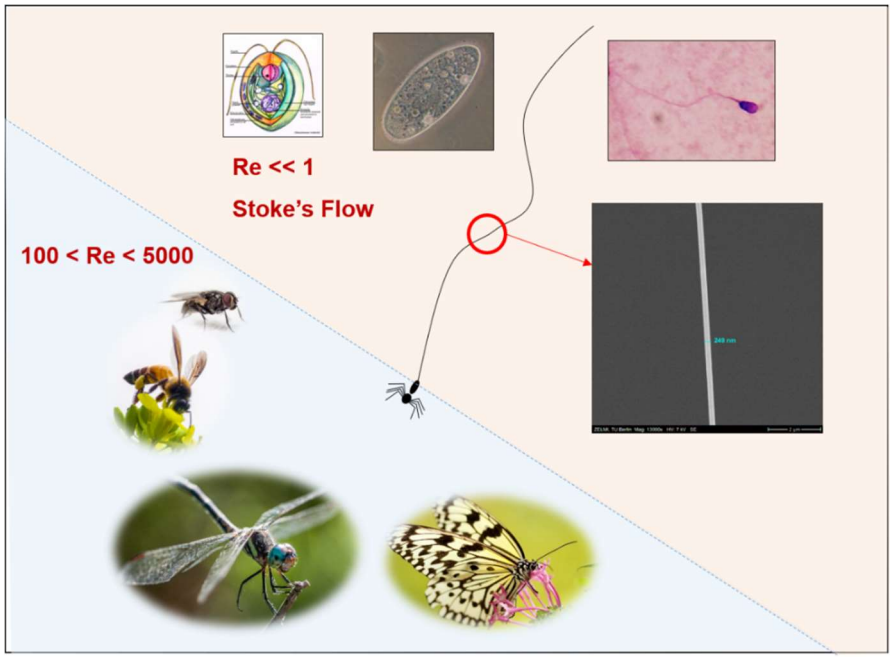

Figure 23. Simple schematics of two different flow regimes in animal locomotion. Although the body scale of a spider belongs to the scales of winged insects, the flow regimes around spider silks are low Reynolds number flow regimes, which can be frequently found in the locomotion of micro-organisms and cells. (Figures and photos by Ninghui Shi, Barfooz, Bobjgalindo on Wikipedia; Photos by Manlake Gabriel, Mamun Srizon, Boris Smokrovic, photostockeditor on Unsplash)

$$Bn_{tur} = \frac{\eta \sigma L}{\left({}^{m_{spider}}/_{n}\right) g} \tag{4.1}$$

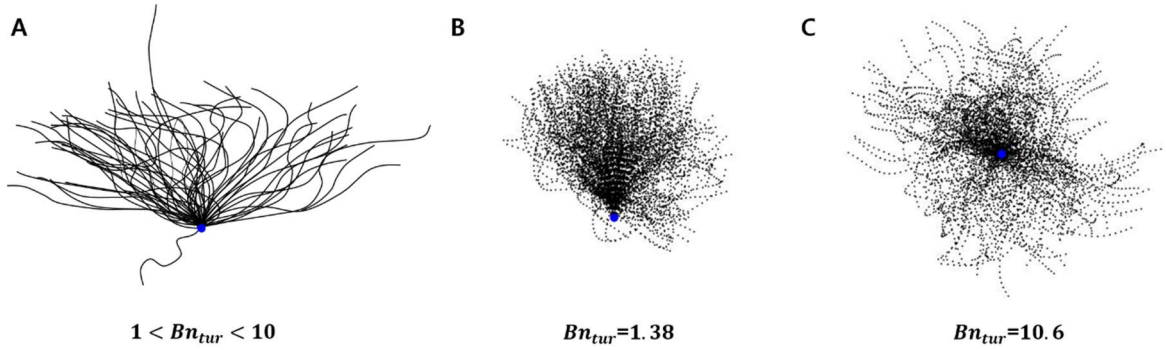

Figure 24. Superposed shapes of ballooning silks during the flight. The reference point is the position of its body (A) Superposed shapes of the observed ballooning events in the nature. ($1 < Bn_{tur} < 10$; Cho et al. 2018) (B) Superposed shapes of the ballooning silks in the simulation ($Bn_{tur} = 1.38$). The blue point means the position of a spider body (a point-mass). (C) Superposed shapes of the ballooning silks in the simulation ($Bn_{tur} = 10.6$). The blue point means the position of a spider body (a point-mass).

5 Conclusion

While the dynamics of a particle and a filament in a fluid flow have been independently and widely studied, the combined asymmetric structure of the two has been investigated far less extensively. This 'combined asymmetric structure' refers to a filament, at the end of which a point-mass is attached. This structure is also a physical model of a ballooning spider in the air. Here, the suspension dynamics of the structure were studied using numerical simulation. For the generalisation of the parameters, the ballooning number is newly defined as the ratio of the Stokes force on a filament to the gravity force on the weight. The simulation results revealed interesting characteristics of the ballooning structure in the non-uniform flows. First, the structure in a shear flow settles slower than would be the case in a still medium. This slow settling is caused by the anisotropic drag of a filament in a low Reynolds number flow. The slow settling occurs primarily due to the geometrically inclined attitude of a filament; secondarily, it occurs due to the force induced by and from a shear flow. Moreover, in a cellular flow field, the structure showed various settling and suspension modes. These motions mostly depend on the size and the strength of a cellular flow, and are thereby categorised according to these parameters. At the low ballooning number $Bn_{vor} < 1$, the structure behaved like a heavy particle; there is neither a retardation effect nor an acceleration effect $\langle V_z \rangle / V_{z,still} \approx 1$. At the high ballooning number $Bn_{vor} > 1$ and small vortex cell size $L_c/L_s < 1.2$, the structure is swept up by the vortical flows and settled faster than would be the case in a still medium. Furthermore, if the size of a vortex cell is larger than $1.2\ L_s$ and Bn_{vor} is larger than 1, the ballooning structure settles slowly or is trapped by a vortex and suspends with $\langle V_z \rangle / V_{z,still} \approx 0$. Different initial conditions of x_0 were also applied. Their motions converged to trapping motion by vortex cells at the end. While the point mass (spider's body) alone cannot be trapped by a vortex, this heavy particle (spider) is trapped with the help of the filament (spider silk). The ballooning structure also shows biased behaviour toward slow settling under homogeneous turbulence, while that of a point-like aerial seed was not similarly biased under identical turbulence conditions. As the nonlinearity of anisotropic drag of a flexible filament, which is deformed by non-uniform flows, was recognised as the cause of retardation and trapping of the ballooning structure in a shear flow and a cellular flow field, the drag anisotropy of a spider silk and the vortex trapping motion seem to be the main reasons, how they can suspend in the convective air current for a long time. Due to the abundance of turbulent eddies in the atmosphere, these retarding and trapping phenomena are plausible in spiders' ballooning flight and can explain how they acquire energies from the nonuniform air current for their long aerial journey.

6 Acknowledgments

The author deeply thanks Prof. Dr.-Ing. Klaus Affeld for scientific discussions and support concerning with this project.

7 References

Adrian, R. J. (2007): Hairpin vortex organization in wall turbulence. In Physics of Fluids 19 (4), p. 41301. DOI: 10.1063/1.2717527.

Adrian, R. J.; Meinhart, C. D.; Tomkins, C. D. (2000): Vortex organization in the outer region of the turbulent boundary layer. In J. Fluid Mech. 422, pp. 1–54. DOI: 10.1017/S0022112000001580.

Balachandar, S.; Eaton, John K. (2010): Turbulent Dispersed Multiphase Flow. In Annu. Rev. Fluid Mech. 42 (1), pp. 111–133. DOI: 10.1146/annurev.fluid.010908.165243.

Bearman, P. W. (1972): Some measurements of the distortion of turbulence approaching a two-dimensional bluff body. In J. Fluid Mech. 53 (03), p. 451. DOI: 10.1017/S0022112072000254.

Bergougnoux, Laurence; Bouchet, Gilles; Lopez, Diego; Guazzelli, Élisabeth (2014): The motion of solid spherical particles falling in a cellular flow field at low Stokes number. In Physics of Fluids 26 (9), p. 93302. DOI: 10.1063/1.4895736.

Boyadzhiev, L. (1973): On the movement of a spherical particle in vertically oscillating liquid. In J. Fluid Mech. 57 (03), p. 545. DOI: 10.1017/S0022112073001333.

Brennen, C.; Winet, H. (1977): Fluid Mechanics of Propulsion by Cilia and Flagella. In Annu. Rev. Fluid Mech. 9 (1), pp. 339–398. DOI: 10.1146/annurev.fl.09.010177.002011.

Brouzet, C.; Verhille, G.; Le Gal, P. (2014): Flexible fiber in a turbulent flow: a macroscopic polymer. In Physical review letters 112 (7), p. 74501. DOI: 10.1103/PhysRevLett.112.074501.

Burgers, J. M. (1938): in Second Report on Viscosity and Plasticity: Noord-Hollandsche Uitgevers-Maatschappij (Verhandelingen der Koninklijke Akademie van Wetenschappen, Afdeeling Natuurkunde: Wiskunde, natuurkunde, scheikunde, kristallenleer, sterrenkunde, weerkunde, en ingenieurswetenschappen). Available online at https://books.google.de/books?id=M94cHQAACAAJ.

Bustamante, C.; Marko, J.; Siggia, E.; Smith, S. (1994): Entropic elasticity of lambda-phage DNA. In Science 265 (5178), pp. 1599–1600. DOI: 10.1126/science.8079175.

Bustamante, C.; Smith, S. B.; Liphardt, J.; Smith, D. (2000): Single-molecule studies of DNA mechanics. In Current opinion in structural biology 10 (3), pp. 279–285.

Childress, Stephen (1981): Mechanics of swimming and flying. Cambridge: Cambridge University Press (Cambridge studies in mathematical biology, 2). Available online at https://doi.org/10.1017/CBO9780511569593.

Cho, Moonsung; Neubauer, Peter; Fahrenson, Christoph; Rechenberg, Ingo (2018): An observational study of ballooning in large spiders: Nanoscale multifibers enable large spiders' soaring flight. In PLoS biology 16 (6), e2004405. DOI: 10.1371/journal.pbio.2004405.

Dai, Liang; van der Maarel, Johan; Doyle, Patrick S. (2014): Extended de Gennes Regime of DNA Confined in a Nanochannel. In Macromolecules 47 (7), pp. 2445–2450. DOI: 10.1021/ma500326w.

Darwin, Charles (1845): Journal of researches into the natural history and geology of the countries visited during the voyage of H.M.S. Beagle round the world,, under the Command of Capt. Fitz Roy, R.N. Second Edition. New York: John Murray, Albemarle Street.

Das, Dibyendu; Sabhapandit, Sanjib (2008): Accurate statistics of a flexible polymer chain in shear flow. In Physical

review letters 101 (18), p. 188301. DOI: 10.1103/PhysRevLett.101.188301.

Delgado-Buscalioni, Rafael (2006): Cyclic motion of a grafted polymer under shear flow. In Physical review letters 96 (8), p. 88303. DOI: 10.1103/PhysRevLett.96.088303.

Delmotte, Blaise; Climent, Eric; Plouraboué, Franck (2015): A general formulation of Bead Models applied to flexible fibers and active filaments at low Reynolds number. In Journal of Computational Physics 286, pp. 14–37. DOI: 10.1016/j.jcp.2015.01.026.

Dhont, Jan K. G. (2003): An introduction to dynamics of colloids. 2. impr. Amsterdam: Elsevier (Studies in interface science, 2).

Doi, Masao; Edwards, Samuel F. (2007): The theory of polymer dynamics. Oxford: Clarendon Press (International series of monographs on physics, 73).

Doyle, P. S.; Ladoux, B.; Viovy, J. L. (2000): Dynamics of a tethered polymer in shear flow. In Physical review letters 84 (20), pp. 4769–4772. DOI: 10.1103/PhysRevLett.84.4769.

Doyle, Patrick S.; Underhill, Patrick T. (2005): Brownian Dynamics Simulations of Polymers and Soft Matter. In Sidney Yip (Ed.): Handbook of materials modeling, vol. 19. Dordrecht: Springer, pp. 2619–2630.

Dreyfus, Rémi; Baudry, Jean; Roper, Marcus L.; Fermigier, Marc; Stone, Howard A.; Bibette, Jérôme (2005): Microscopic artificial swimmers. In Nature 437 (7060), pp. 862–865. DOI: 10.1038/nature04090.

Drummond, I. T.; Duane, S.; Horgan, R. R. (1984): Scalar diffusion in simulated helical turbulence with molecular diffusivity. In J. Fluid Mech. 138 (-1), p. 75. DOI: 10.1017/S0022112084000045.

Finnigan, J. J.; Shaw, Roger H.; Patton, Edward G. (2009): Turbulence structure above a vegetation canopy. In J. Fluid Mech. 637, p. 387. DOI: 10.1017/S0022112009990589.

Fung, J.; Vassilicos, J. (1998): Two-particle dispersion in turbulentlike flows. In Phys. Rev. E 57 (2), pp. 1677–1690. DOI: 10.1103/PhysRevE.57.1677.

Fung, J. C. H. (1993): Gravitational settling of particles and bubbles in homogeneous turbulence. In J. Geophys. Res. 98 (C11), p. 20287. DOI: 10.1029/93JC01845.

Fung, J. C. H. (1998): Effect of nonlinear drag on the settling velocity of particles in homogeneous isotropic turbulence. In J. Geophys. Res. 103 (C12), pp. 27905–27917. DOI: 10.1029/98JC02822.

Fung, J. C. H.; Hunt, J. C. R.; Malik, N. A.; Perkins, R. J. (1992): Kinematic simulation of homogeneous turbulence by unsteady random Fourier modes. In J. Fluid Mech. 236 (-1), p. 281. DOI: 10.1017/S0022112092001423.

Fung, J. C. H.; Perkins, R. J. (2008): Dispersion modeling by kinematic simulation: Cloud dispersion model. In Fluid Dyn. Res. 40 (4), pp. 273–309. DOI: 10.1016/j.fluiddyn.2007.06.005.

Fung, J. C. H.; Vassilicos, J. C. (2003): Inertial particle segregation by turbulence. In Physical review. E, Statistical, nonlinear, and soft matter physics 68 (4 Pt 2), p. 46309. DOI: 10.1103/PhysRevE.68.046309.

Fung, J.C.H. (1997): Gravitational settling of small spherical particles in unsteady cellular flow fields. In Journal of Aerosol Science 28 (5), pp. 753–787. DOI: 10.1016/S0021-8502(96)00478-8.

Fung, Jimmy Chi Hung: Kinematic simulation of turbulent flow and particle motions. Apollo - University of Cambridge Repository.

Fung, Y. C. (1990): Biomechanics. Motion, Flow, Stress, and Growth. New York, NY: Springer. Available online at http://dx.doi.org/10.1007/978-1-4419-6856-2.

Gauger, Erik; Stark, Holger (2006): Numerical study of a microscopic artificial swimmer. In Physical review. E, Statistical, nonlinear, and soft matter physics 74 (2 Pt 1), p. 21907. DOI: 10.1103/PhysRevE.74.021907.

Gerashchenko, Sergiy; Steinberg, Victor (2006): Statistics of tumbling of a single polymer molecule in shear flow. In Physical review letters 96 (3), p. 38304. DOI: 10.1103/PhysRevLett.96.038304.

Glick, P. A. (1939): The distribution of insects, spiders, and mites in the air. In USDA Tech Bull (673), pp. 1–150.

Gorham, Peter W. (2013): Ballooning Spiders: The Case for Electrostatic Flight. Available online at https://arxiv.org/abs/1309.4731v2.

Gosline, J. M.; Guerette, P. A.; Ortlepp, C. S.; Savage, K. N. (1999): The mechanical design of spider silks: from fibroin sequence to mechanical function. In The Journal of experimental biology 202 (Pt 23), pp. 3295–3303.

Gustavsson, K.; Meneguz, E.; Reeks, M.; Mehlig, B. (2012): Inertial-particle dynamics in turbulent flows: caustics, concentration fluctuations and random uncorrelated motion. In New J. Phys. 14 (11), p. 115017. DOI: 10.1088/1367-2630/14/11/115017.

Happel, John; Brenner, Howard (1991): Low Reynolds number hydrodynamics. With special applications to particulate media. 5. printing. Dordrecht: Kluwer Acad. Publ (Mechanics of fluids and transport processes).

Harris, I. (Ed.) (1971): The nature of the wind. Proc. Seminar at Inst. Civil Engrs, June 1970.

Hinze, Julius Oscar (1987): Turbulence. 2. ed., reissued. New York, NY: McGraw-Hill (McGraw-Hill series in mechanical engineering).

Hommema, Scott E.; Adrian, Ronald J. (2003): Packet structure of surface eddies in the atmospheric boundary layer. In Boundary-Layer Meteorology 106 (1), pp. 147–170. DOI: 10.1023/A:1020868132429.

Humphrey, J. A. C. (1987): Fluid mechanic constraints on spider ballooning. In Oecologia 73 (3), pp. 469–477. DOI: 10.1007/BF00385267.

Hunt, J. C. R. (1973): A theory of turbulent flow round two-dimensional bluff bodies. In J. Fluid Mech. 61 (04), p. 625. DOI: 10.1017/S0022112073000893.

Hunt, Julian C.R.; Morrison, Jonathan F. (2000): Eddy structure in turbulent boundary layers. In European Journal of Mechanics - B/Fluids 19 (5), pp. 673–694. DOI: 10.1016/S0997-7546(00)00129-1.

Ibáñez-García, Gabriel O.; Hanna, Simon (2009): Relaxation of an initially-stretched, tethered polymer under shear flow: a Brownian dynamics simulation. In Soft Matter 5 (22), p. 4464. DOI: 10.1039/b916087f.

Jeffrey, D. J.; Onishi, Y. (1984): The forces and couples acting on two nearly touching spheres in low-Reynolds-number flow. In Z. angew. Math. Phys. 35 (5), pp. 634–641. DOI: 10.1007/BF00952109.

Jian, Hongmei; Vologodskii, Alexander V.; Schlick, Tamar (1997): A Combined Wormlike-Chain and Bead Model for Dynamic Simulations of Long Linear DNA. In Journal of Computational Physics 136 (1), pp. 168–179. DOI: 10.1006/jcph.1997.5765.

Jo, Kyubong; Chen, Yeng-Long; Pablo, Juan J. de; Schwartz, David C. (2009): Elongation and migration of single DNA molecules in microchannels using oscillatory shear flows. In Lab on a chip 9 (16), pp. 2348–2355. DOI: 10.1039/b902292a.

Joel, Anna-Christin; Baumgartner, Werner (2017): Nanofibre production in spiders without electric charge. In The Journal of experimental biology 220 (Pt 12), pp. 2243–2249. DOI: 10.1242/jeb.157594.

Ko, Frank K.; Kawabata, Sueo; Inoue, Mari; Niwa, Masako; Fossey, Stephen; Song, John W. (2001): Engineering

Properties of Spider Silk. In MRS Proc. 702, p. 91. DOI: 10.1557/PROC-702-U1.4.1.

Kraichnan, Robert H. (1970): Diffusion by a Random Velocity Field. In Phys. Fluids 13 (1), p. 22. DOI: 10.1063/1.1692799.

Kronenberger, Katrin; Vollrath, Fritz (2015): Spiders spinning electrically charged nano-fibres. In Biology letters 11 (1), p. 20140813. DOI: 10.1098/rsbl.2014.0813.

Ladoux, B.; Doyle, P. S. (2000): Stretching tethered DNA chains in shear flow. In Europhys. Lett. 52 (5), pp. 511–517. DOI: 10.1209/epl/i2000-00467-y.

Lafitte, Anthony; Le Garrec, Thomas; Bailly, Christophe; Laurendeau, Estelle (2014): Turbulence Generation from a Sweeping-Based Stochastic Model. In AIAA Journal 52 (2), pp. 281–292. DOI: 10.2514/1.J052368.

Larson, R. G.; Perkins, T. T.; Smith, D. E.; Chu, S. (1997): Hydrodynamics of a DNA molecule in a flow field. In Phys. Rev. E 55 (2), pp. 1794–1797. DOI: 10.1103/PhysRevE.55.1794.

Lauga, Eric; Powers, Thomas R. (2009): The hydrodynamics of swimming microorganisms. In Rep. Prog. Phys. 72 (9), p. 96601. DOI: 10.1088/0034-4885/72/9/096601.

Leclercq, Tristan; Langre, Emmanuel de (2018): Reconfiguration of elastic blades in oscillatory flow. In J. Fluid Mech. 838, pp. 606–630. DOI: 10.1017/jfm.2017.910.

Lee, Nam-Kyung; d. Thirumalai (2004): Pulling-Speed-Dependent Force-Extension Profiles for Semiflexible Chains. In Biophysical Journal 86 (5), pp. 2641–2649. DOI: 10.1016/S0006-3495(04)74320-9.

Lindström, Stefan B.; Uesaka, Tetsu (2007): Simulation of the motion of flexible fibers in viscous fluid flow. In Physics of Fluids 19 (11), p. 113307. DOI: 10.1063/1.2778937.

Litvinov, S.; Hu, X. Y.; Adams, N. A. (2011): Numerical simulation of tethered DNA in shear flow. In Journal of physics. Condensed matter : an Institute of Physics journal 23 (18), p. 184118. DOI: 10.1088/0953-8984/23/18/184118.

Lowe, Christopher P. (2003): Dynamics of filaments: modelling the dynamics of driven microfilaments. In Philosophical Transactions of the Royal Society B: Biological Sciences 358 (1437), pp. 1543–1550. DOI: 10.1098/rstb.2003.1340.

Manton, M. J. (1974): On the motion of a small particle in the atmosphere. In Boundary-Layer Meteorol 6 (3-4), pp. 487–504. DOI: 10.1007/BF02137681.

Material Properties of Spider Silk (2003). Degree of Master of Science. University of Rochester, Rochester, NY.

Maxey, M. R. (1987): The gravitational settling of aerosol particles in homogeneous turbulence and random flow fields. In J. Fluid Mech. 174 (1), p. 441. DOI: 10.1017/S0022112087000193.

Maxey, M. R. (1987): The motion of small spherical particles in a cellular flow field. In Phys. Fluids 30 (7), p. 1915. DOI: 10.1063/1.866206.

Maxey, M. R.; Corrsin, S. (1986): Gravitational Settling of Aerosol Particles in Randomly Oriented Cellular Flow Fields. In J. Atmos. Sci. 43 (11), pp. 1112–1134. DOI: 10.1175/1520-0469(1986)043<1112:GSOAPI>2.0.CO;2.

Monin, A. S.; Yaglom, A. M.; Ablow, C. M. (1977): StatisticalFluidMechanics : TheMechanicsofTurbulence. In American Journal of Physics 45 (10), p. 1010. DOI: 10.1119/1.10870.

Morley, Erica L.; Robert, Daniel (2018): Electric Fields Elicit Ballooning in Spiders. In Current biology : CB 28 (14), 2324-2330.e2. DOI: 10.1016/j.cub.2018.05.057.

Ning, Zemin; Melrose, John R. (1999): A numerical model for simulating mechanical behavior of flexible fibers. In The Journal of Chemical Physics 111 (23), pp. 10717–10726. DOI: 10.1063/1.480426.

Ortega-Jimenez, Victor Manuel; Dudley, Robert (2013): Spiderweb deformation induced by electrostatically charged insects. In Scientific reports 3, p. 2108. DOI: 10.1038/srep02108.

Perkins, T.; Quake; Smith, D.; Chu, S. (1994): Relaxation of a single DNA molecule observed by optical microscopy. In Science 264 (5160), pp. 822–826. DOI: 10.1126/science.8171336.

Perkins, T.; Smith, D.; Larson, R.; Chu, S. (1995): Stretching of a single tethered polymer in a uniform flow. In Science 268 (5207), pp. 83–87. DOI: 10.1126/science.7701345.

Purcell, E. M. (1977): Life at low Reynolds number. In American Journal of Physics 45 (1), pp. 3–11. DOI: 10.1119/1.10903.

Reeks, M. W. (1977): On the dispersion of small particles suspended in an isotropic turbulent fluid. In J. Fluid Mech. 83 (03), p. 529. DOI: 10.1017/S0022112077001323.

Reynolds, A. M.; Bohan, D. A.; Bell, J. R. (2006): Ballooning dispersal in arthropod taxa with convergent behaviours: dynamic properties of ballooning silk in turbulent flows. In Biology letters 2 (3), pp. 371–373. DOI: 10.1098/rsbl.2006.0486.

Riley, James J. (1974): Diffusion experiments with numerically integrated isotropic turbulence. In Phys. Fluids 17 (2), p. 292. DOI: 10.1063/1.1694714.

Rotne, Jens; Prager, Stephen (1969): Variational Treatment of Hydrodynamic Interaction in Polymers. In The Journal of Chemical Physics 50 (11), pp. 4831–4837. DOI: 10.1063/1.1670977.

Rouse, Prince E. (1953): A Theory of the Linear Viscoelastic Properties of Dilute Solutions of Coiling Polymers. In The Journal of Chemical Physics 21 (7), pp. 1272–1280. DOI: 10.1063/1.1699180.

Schroeder, Charles M.; Shaqfeh, Eric S. G.; Chu, Steven (2004): Effect of Hydrodynamic Interactions on DNA Dynamics in Extensional Flow: Simulation and Single Molecule Experiment. In Macromolecules 37 (24), pp. 9242–9256. DOI: 10.1021/ma049461l.

Schroeder, Charles M.; Teixeira, Rodrigo E.; Shaqfeh, Eric S. G.; Chu, Steven (2005): Characteristic periodic motion of polymers in shear flow. In Physical review letters 95 (1), p. 18301. DOI: 10.1103/PhysRevLett.95.018301.

Shaqfeh, Eric S.G. (2005): The dynamics of single-molecule DNA in flow. In Journal of Non-Newtonian Fluid Mechanics 130 (1), pp. 1–28. DOI: 10.1016/j.jnnfm.2005.05.011.

Snyder, W. H.; Lumley, J. L. (1971): Some measurements of particle velocity autocorrelation functions in a turbulent flow. In J. Fluid Mech. 48 (01), p. 41. DOI: 10.1017/S0022112071001460.

Squires, Kyle D.; Eaton, John K. (1990): Particle response and turbulence modification in isotropic turbulence. In Physics of Fluids A: Fluid Dynamics 2 (7), pp. 1191–1203. DOI: 10.1063/1.857620.

Squires, Kyle D.; Eaton, John K. (1991): Preferential concentration of particles by turbulence. In Physics of Fluids A: Fluid Dynamics 3 (5), pp. 1169–1178. DOI: 10.1063/1.858045.

Stommel, H. (1949): Trajectories of small bodies sinking slowly through convection cells. In J. Mar. Res. 8, pp. 24–29.

Stout, J. E.; Arya, S. P.; Genikhovich, E. L. (1995): The Effect of Nonlinear Drag on the Motion and Settling Velocity of Heavy Particles. In J. Atmos. Sci. 52 (22), pp. 3836–3848. DOI: 10.1175/1520-0469(1995)052<3836:TEONDO>2.0.CO;2.

Suter, Robert B. (1991): Ballooning in spiders. Results of wind tunnel experiments. In Ethology Ecology & Evolution 3 (1), pp. 13–25. DOI: 10.1080/08927014.1991.9525385.

Suter, Robert B. (1992): Ballooning: Data from Spiders in Freefall Indicate the Importance of Posture. In The Journal of Arachnology 2 (20), pp. 107–113. Available online at http://www.jstor.org/stable/3705774.

Suter, Robert B. (1999): An Aerial Lottery: The Physics of Ballooning in a Chaotic Atmosphere 1 (27), pp. 281–293. Available online at http://www.jstor.org/stable/3705999.

Suzuki, Takeshi; Sakai, Yasuhiko (2003): Numerical Simulation of Reactive Turbulent Scalar Mixing Layer by Fourier Modes and Lagrangian Molecular Mixing Model. In The Proceedings of the Fluids engineering conference 2003 (0), p. 112. DOI: 10.1299/jsmefed.2003.112.

Taylor, Geoffrey Ingram and Green, Albert Edward (1937): Mechanism of the production of small eddies from large ones. In Proc. R. Soc. Lond. A 158 (895), pp. 499–521. DOI: 10.1098/rspa.1937.0036.

Toschi, Federico; Bodenschatz, Eberhard (2009): Lagrangian Properties of Particles in Turbulence. In Annu. Rev. Fluid Mech. 41 (1), pp. 375–404. DOI: 10.1146/annurev.fluid.010908.165210.

Turfus C. (1985): Stochastic Modelling of Turbulent Dispersion Near Surfaces: University of Cambridge.

Vassilicos, J. C.; Fung, J. C. H. (1995): The self-similar topology of passive interfaces advected by two-dimensional turbulent-like flows. In Physics of Fluids 7 (8), pp. 1970–1998. DOI: 10.1063/1.868510.

Verhille, Gautier; Bartoli, Adrien (2016): 3D conformation of a flexible fiber in a turbulent flow. In Exp Fluids 57 (7), p. 74501. DOI: 10.1007/s00348-016-2201-1.

Vollrath, Fritz; Edmonds, Donald (2013): Consequences of electrical conductivity in an orb spider's capture web. In Die Naturwissenschaften 100 (12), pp. 1163–1169. DOI: 10.1007/s00114-013-1120-8.

Wang, Jun; Lu, Chang (2007): Single molecule λ-DNA stretching studied by microfluidics and single particle tracking. In Journal of Applied Physics 102 (7), p. 74703. DOI: 10.1063/1.2786896.

Wang, Lian-Ping; Maxey, Martin R. (1993): Settling velocity and concentration distribution of heavy particles in homogeneous isotropic turbulence. In J. Fluid Mech. 256 (-1), p. 27. DOI: 10.1017/S0022112093002708.

Wells, M. R.; Stock, D. E. (1983): The effects of crossing trajectories on the dispersion of particles in a turbulent flow. In J. Fluid Mech. 136 (-1), p. 31. DOI: 10.1017/S0022112083002049.

Winkler, Roland G. (2006): Semiflexible polymers in shear flow. In Physical review letters 97 (12), p. 128301. DOI: 10.1103/PhysRevLett.97.128301.

Wong, P. Kina.K.; Lee, Yi-Kuen; Ho, Chih-Ming (2003): Deformation of DNA molecules by hydrodynamic focusing. In J. Fluid Mech. 497, pp. 55–65. DOI: 10.1017/S002211200300658X.

Yamamoto, Satoru; Matsuoka, Takaaki (1993): A method for dynamic simulation of rigid and flexible fibers in a flow field. In The Journal of Chemical Physics 98 (1), pp. 644–650. DOI: 10.1063/1.464607.

Yip, Sidney (Ed.) (2005): Handbook of materials modeling. Dordrecht: Springer.

Zhao, Longhua; Panayotova, Lordanka N.; Chuang, Angela; Sheldon, Kimberly S.; Bourouiba, Lydia; Miller, Laura A. (2017): Flying Spiders: Simulating and Modeling the Dynamics of Ballooning. In Anita T. Layton, Laura A. Miller (Eds.): Women in Mathematical Biology, vol. 8. Cham: Springer International Publishing (Association for Women in Mathematics Series), pp. 179–210.

Appendix A. Validation

To validate the anisotropic character of the bead model, we compared the results of hydrodynamic simulation with the results of the approximate method proposed by Burgers (1938, Happel and Brenner 1991) and experimental data. The experiment is implemented using straight and cylindrical steel wires with thicknesses ranging from 0.3-0.8 mm. The drag forces of these steel wires are measured in both directions (transverse, in the direction perpendicular to the axis, and longitudinally, in the direction of the axis) by dropping the wires into corn syrup with viscosities ranging from 2-3 kg/ms. The simulation values coincide very well with those of the experiments and the theoretical values. The experiment shows the 1.3-2.2 factors of the ratio between a transverse drag and a longitudinal drag. The values from the approximated method indicate the factors of 1.5-1.6. The simulation shows the factors of 1.3-1.5. This ratio of the drag on a wire moving perpendicular to the axis to the drag on a wire moving parallel to its length is supposed to be a factor of 2, however Purcell proposed that it may be around 1.5 from his experiment (Purcell 1977). Although there are large differences in the slenderness of filaments between real ballooning phenomena and our model, a simulation with slenderness of 45 to 120 can describe the anisotropic character of a filament in a low Reynolds flow and can also be used for the study of fibre motion in various fluid flows (Lauga and Powers 2009).

The non-dimensional resistance coefficients, which are based on Burgers' approximated methods (Eqns. (5.29) and (5.30)), are calculated by means of Eqns. (0.3) and (0.4). The non-dimensional resistance coefficients differ from the translation tensor, which has length scale (Happel and Brenner 1991).

$$F_N = \frac{4\pi\eta UL}{\left(ln\left(2\frac{L}{d}\right) + 0.5\right)} \tag{0.1}$$

$$F_T = \frac{2\pi\eta UL}{\left(ln\left(2\frac{L}{d}\right) - 0.72\right)} \tag{0.2}$$

$$R_N = \frac{F_N}{\eta UL} \tag{0.3}$$

$$R_T = \frac{F_T}{\eta UL} \tag{0.4}$$

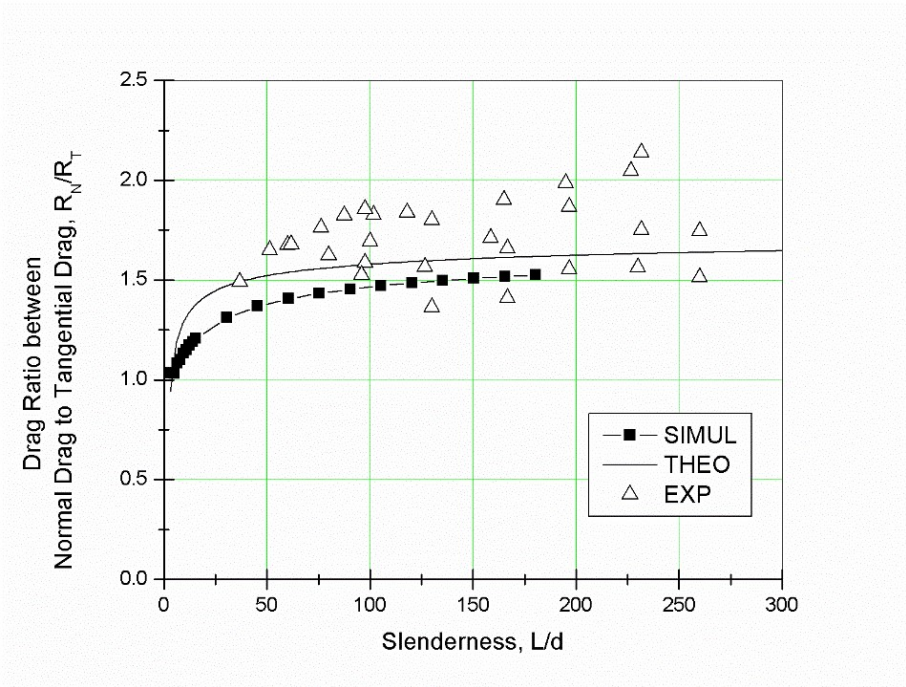

Figure A 1. Drag ratio of the transverse resistance force to the longitudinal resistance force of a thin cylindrical rod.

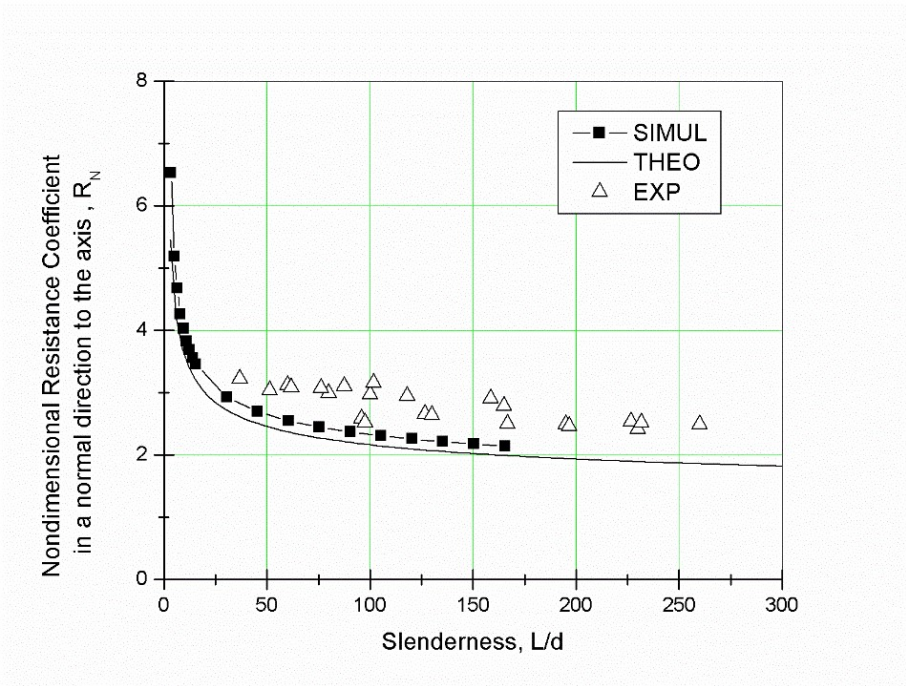

Figure A 2. Dimensionless transverse (normal) resistance coefficients of a thin cylinder as a function of the slenderness of the cylinder.

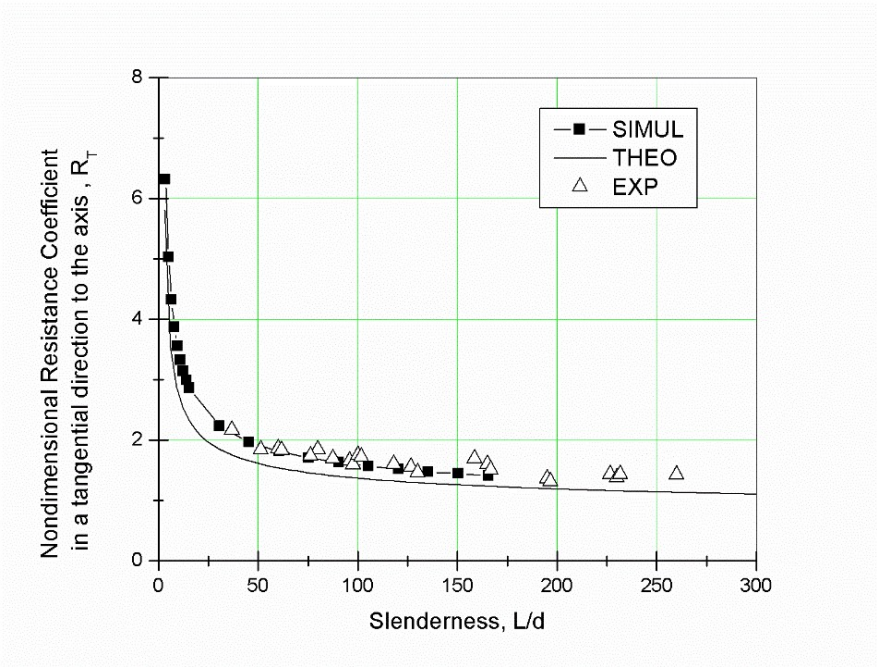

Figure A 3. Dimensionless longitudinal (tangential) resistance coefficients of a thin cylinder as a function of the slenderness of the cylinder.

Appendix B. Input Parameters

B1. Homogeneous Turbulence

The ballooning number is varied by composing different parameters, e.g. the length of the structure, the viscosity of the medium, the turbulent kinetic energy and its weight. Table 0.1 shows the input parameters which are used in the simulation. The elastic constant of the tensile spring is increased, because the elongation of a spider silk is limited to the 30% of the initial length (Ko et al. 2001, Bonino 2003). The divergence problem of the bead-spring model in the turbulent flow field is corrected by adjusting the bending stiffness of the bending spring to 0.1 Nm.

Table 0.1 Input parameters for a homogeneous turbulence.

	Values
Bn_{tur}	0.022 - 445
n	20, 30, 40
TKE $[m^2/s^2]$	0.23 - 2.45
σ	0.68 - 2.22
$\eta\,[kg/(m \cdot s)]$	0.1, 0.2, 0.5, 1, 2, 5
a $[m]$	0.1
a_1	a
$a_2, \cdots, a_n$	a
g_0	a
l_0	$3a$
w_1 $[kg]$	0.01, 0.02, 0.05, 0.1, 0.2 0. 5, 1
$\rho_2, \cdots, \rho_n$ $[kg/m^3]$	1.225
ρ_f $[kg/m^3]$	1.225
k $[N/m]$	300
A $[Nm]$	0.1
Δt $[sec]$	0.001

B2. Shear Flow

Table 0.2 shows input parameter sets for a shear flow. Different sets and combinations of input parameters are used, in order to cover the wide range of the ballooning number. The sets of 1-3 in Table 0.2 are used for the model with the hydrodynamic interaction between beads. The set 4 is used for the model without with the hydrodynamic interaction between beads. The variation of the spring constants is applied in order not to exceed elongation of 1.2 of the chain, because the drag anisotropy diminishes as the distance between beads increases.

Table 0.2 Input parameters for a shear flow.

	Set 1	**Set 2**	**Set 3**	**Set 4 (No Hydro.)**
Bn_{shear}	0.011 - 57	0.042 - 1133	1.9 - 4539	0.047 - 155
n	20, 30, 40	40, 60	40, 80	30, 40, 50
γ [/s]	0.1, 0.2, 0.5, 1, 2, 5	0.1, 0.2, 0.5, 1, 2, 5	1, 2, 5, 10	0.1, 0.2, 0.5, 1, 2, 5
η $[kg/(m \cdot s)]$	0.1, 0.2, 0.5, 1, 2, 5	0.1, 0.2, 0.5, 1, 2, 5	0.5, 1, 2, 5, 10	0.1, 0.2, 0.5, 1, 2, 5
a $[m]$	0.1	0.1	0.1	0.1
a_1	a	a	a	a
$a_2, \cdots, a_n$	a	a	a	a
g_0	a	a	a	a
l_0	$3a$	$3a$	$3a$	$3a$
w_1 $[kg]$	$0.1, 0.2, 0.5, 1$	$0.1, 0.2, 0.5, 1$	$0.1, 0.2, 0.5, 1$	$0.1, 0.2, 0.5, 1$
$\rho_2, \cdots, \rho_n$ $[kg/m^3]$	1.225	1.225	1.225	1.225
ρ_f $[kg/m^3]$	1.225	1.225	1.225	1.225
k $[N/m]$	200	300	1000	200
A $[Nm]$	1.0×10^{-4}	1.0×10^{-4}	1.0×10^{-4}	1.0×10^{-4}
Δt $[sec]$	0.001	0.001	0.0005	0.001

B3. Periodic Cellular Flow

The wide range of the ballooning number is achieved by varying the characteristic velocity of the periodic cellular flow and the weight of the ballooning structure. The input parameters are summarised in Table 0.3. The ratio of the filament length to the diameter of a vortex cell is additionally considered by simulating in various sizes of cellular vortex fields. The three different x-axis positions are employed to observe the dependency of the initial condition at the release.

Table 0.3 Input parameters for a periodic cellular flow.

	Values
Bn_{vor}	0.064 - 3.42
n	30
U_0 [m/s]	0.25, 0.5, 1, 1.5
L_c	0.25, 0.5, 0.75, 1, 1.25, 1.5, 2 $\times L$
x_0	0.25, 0.5, 0.75 $\times L$
$\eta\,[kg/(m \cdot s)]$	0.5
a $[m]$	0.1
a_1	a
$a_2, \cdots, a_n$	a
g_0	a
l_0	$3a$
w_1 $[kg]$	$0.1, 0.2, 0.5, 1$
$\rho_2, \cdots, \rho_n$ $[kg/m^3]$	1.225
ρ_f $[kg/m^3]$	1.225
k $[N/m]$	200
A $[Nm]$	1.0×10^{-4}
Δt $[sec]$	0.002

Appendix C. Dynamic Motions

C1. Dynamic Motions in Homogeneous Turbulence

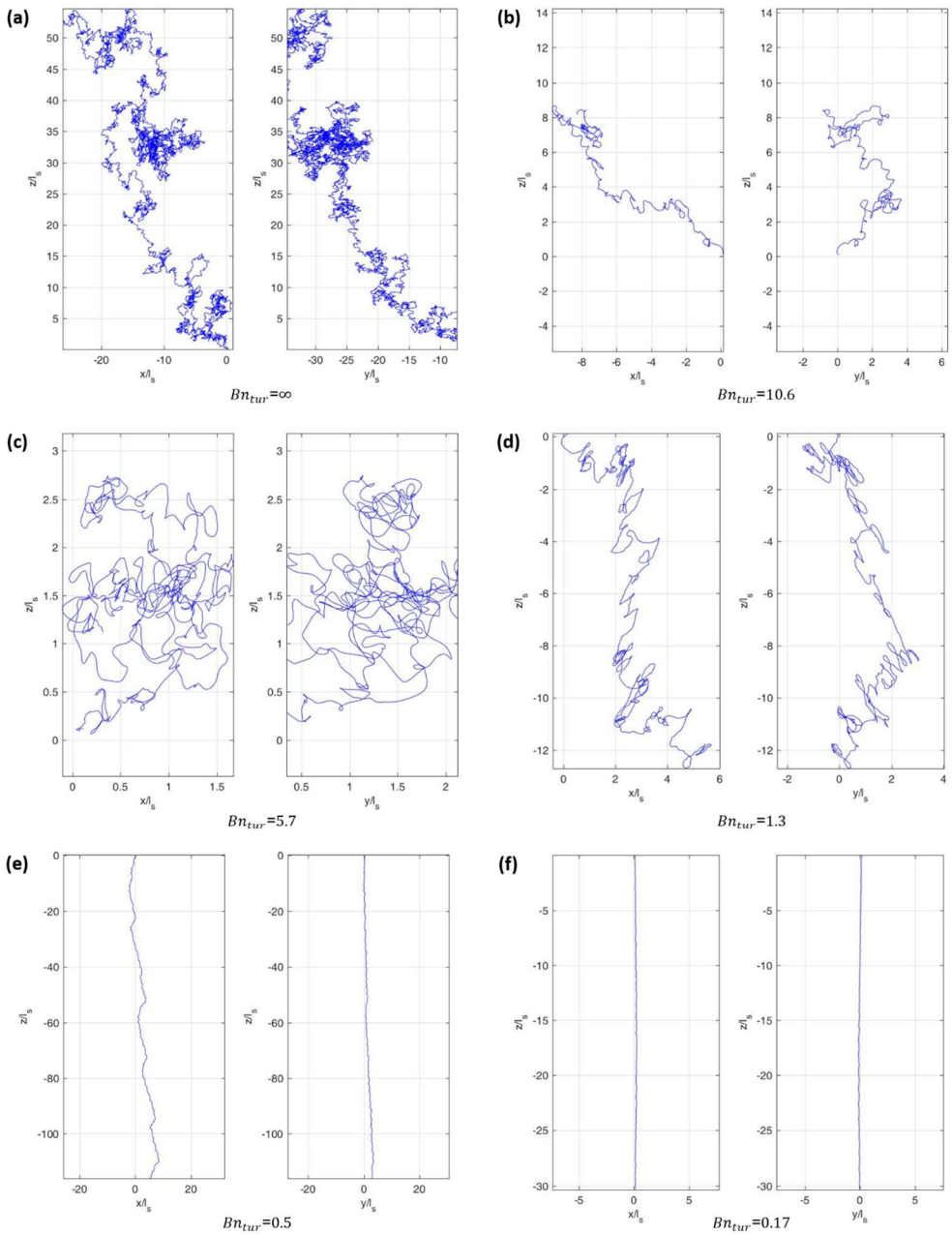

Figure C 1. Trace plots in homogeneous turbulence. (the number of beads: 30, length: 4.45 m, viscosity: 0.2 kg/ms) (a) $Bn_{tur} = \infty$ (mass: $0.61 \times 10^{-4}\ kg$, $\sigma = 0.578$, $u' = 0.381$, $v' = 0.799$, $w' = 0.471$), (b) $Bn_{tur} = 10.6$ (mass: $0.05\ kg$, $\sigma = 0.713$, $u' = 0.633$, $v' = 0.772$, $w' = 0.725$), (c) $Bn_{tur} = 5.7$ (mass: $0.02\ kg$, $\sigma = 0.714$, $u' = 0.510$, $v' = 0.860$, $w' = 0.728$), (d) $Bn_{tur} = 1.3$ (mass: $0.1\ kg$, $\sigma = 0.831$, $u' = 0.735$, $v' = 0.686$, $w' = 1.030$), (e) $Bn_{tur} = 0.5$ (mass: $0.2\ kg$, $\sigma = 0.647$, $u' = 0.712$, $v' = 0.477$, $w' = 0.722$), (f) $Bn_{tur} = 0.17$ (mass: $1\ kg$, $\sigma = 1.012$, $u' = 1.118$, $v' = 1.251$, $w' = 0.509$) ; Unit of σ, u', v', w': $[m/s]$

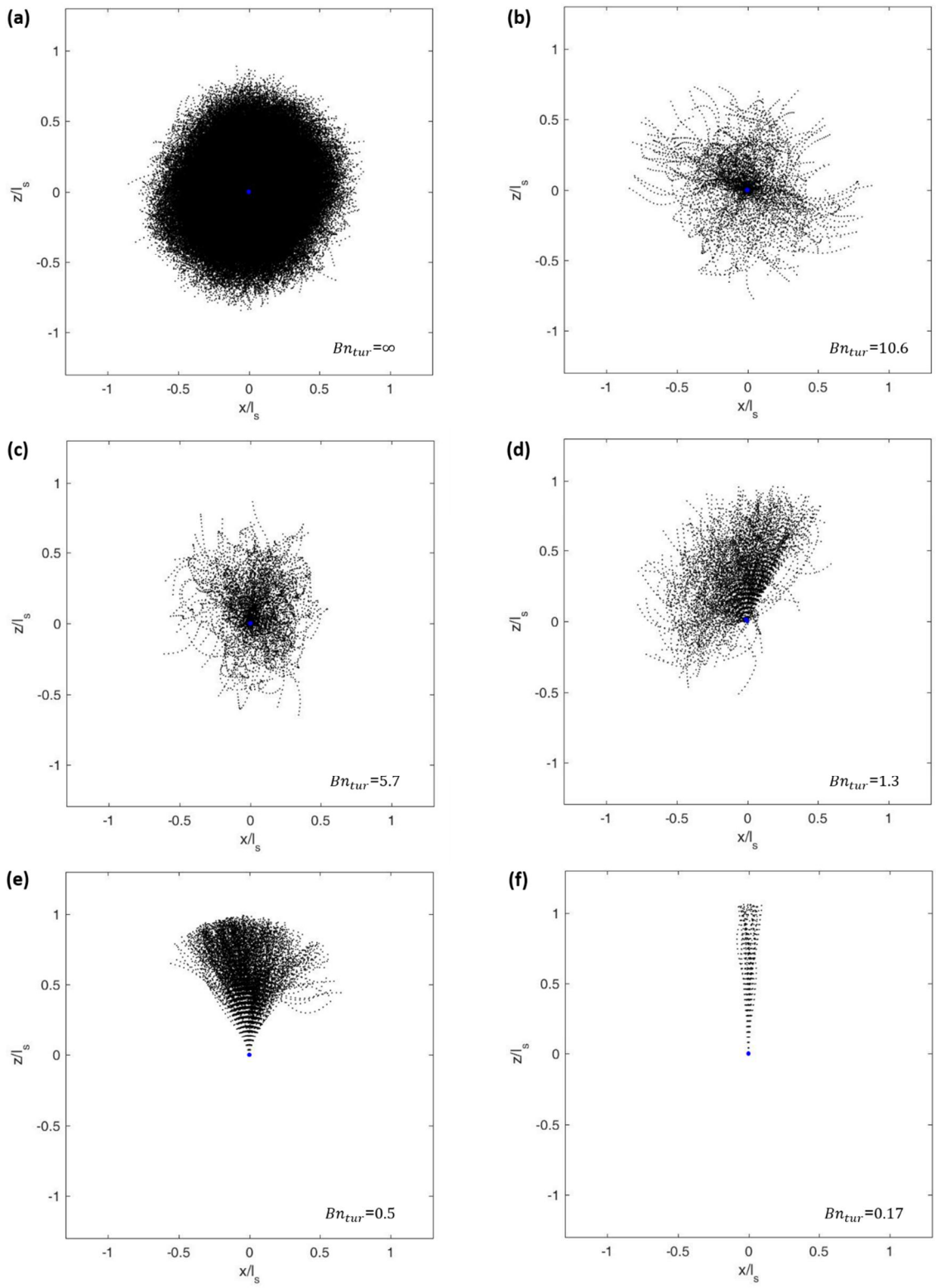

Figure C 2. Projection plots of the filament structure in homogeneous turbulence in the relative coordinate of the lower end. (the number of beads: 30, length: 4.45 m, viscosity: 0.2 kg/ms) (a) $Bn_{tur} = \infty$ (mass: $0.61 \times 10^{-4}\ kg$, $\sigma = 0.578$, $u' = 0.381$, $v' = 0.799$, $w' = 0.471$), (b) $Bn_{tur} = 10.6$ (mass: $0.05\ kg$, $\sigma = 0.713$, $u' = 0.633$, $v' = 0.772$, $w' = 0.725$), (c) $Bn_{tur} = 5.7$ (mass: $0.02\ kg$, $\sigma = 0.714$, $u' = 0.510$, $v' = 0.860$, $w' = 0.728$), (d) $Bn_{tur} = 1.3$ (mass: $0.1\ kg$, $\sigma = 0.831$, $u' = 0.735$, $v' = 0.686$, $w' = 1.030$), (e) $Bn_{tur} = 0.5$ (mass: $0.2\ kg$, $\sigma = 0.647$, $u' = 0.712$, $v' = 0.477$, $w' = 0.722$), (f) $Bn_{tur} = 0.17$ (mass: $1\ kg$, $\sigma = 1.012$, $u' = 1.118$, $v' = 1.251$, $w' = 0.509$) ; Unit of σ, u', v', w': $[m/s]$

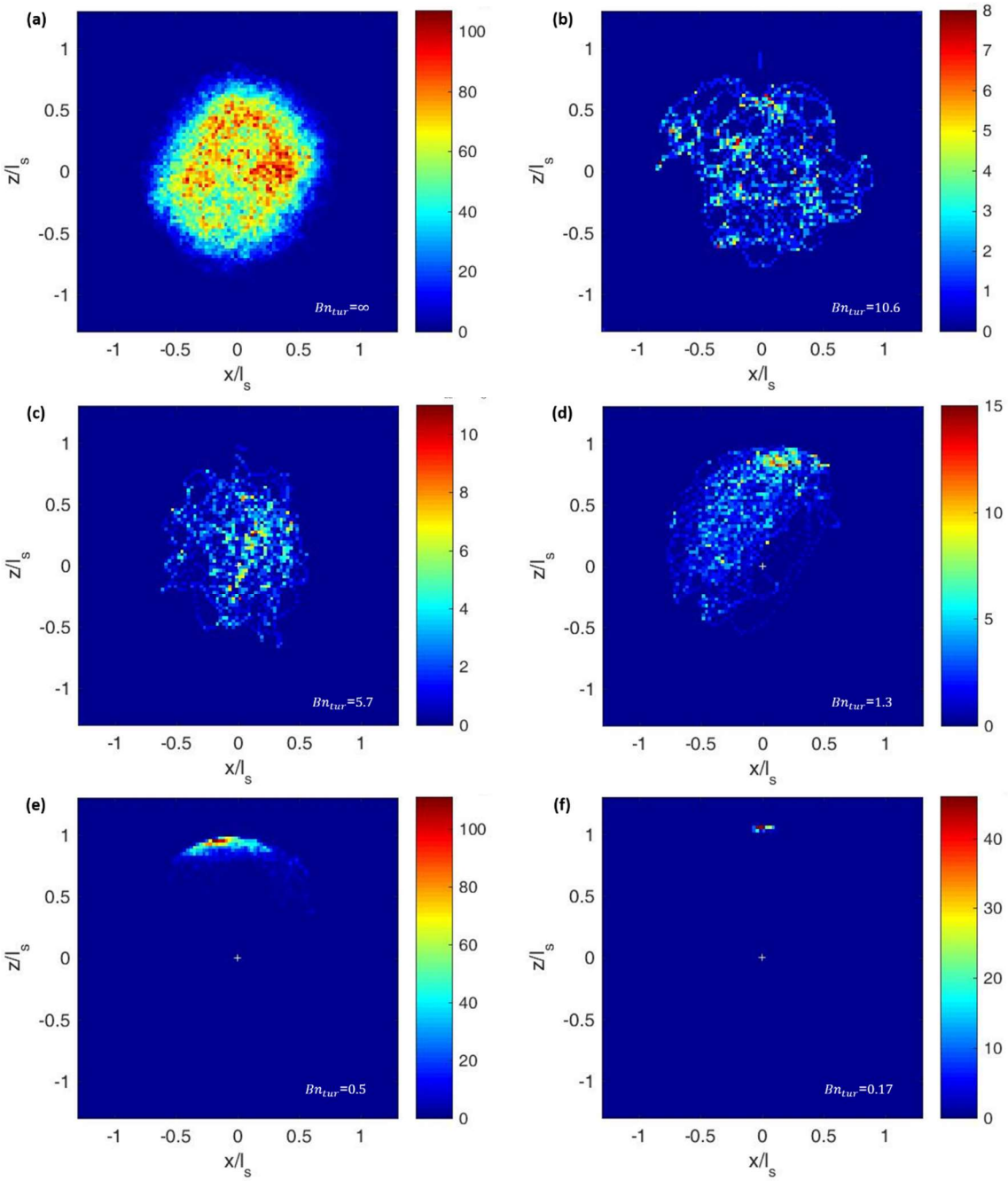

Figure C 3. Projected spatial frequency of the end point of the filament. (the number of beads: 30, length: 4.45 m, viscosity: 0.2 kg/ms) (a) $Bn_{tur} = \infty$ (mass: $0.61 \times 10^{-4}\,kg$, $\sigma = 0.578$, $u' = 0.381$, $v' = 0.799$, $w' = 0.471$), (b) $Bn_{tur} = 10.6$ (mass: $0.05\,kg$, $\sigma = 0.713$, $u' = 0.633$, $v' = 0.772$, $w' = 0.725$), (c) $Bn_{tur} = 5.7$ (mass: $0.02\,kg$, $\sigma = 0.714$, $u' = 0.510$, $v' = 0.860$, $w' = 0.728$), (d) $Bn_{tur} = 1.3$ (mass: $0.1\,kg$, $\sigma = 0.831$, $u' = 0.735$, $v' = 0.686$, $w' = 1.030$), (e) $Bn_{tur} = 0.5$ (mass: $0.2\,kg$, $\sigma = 0.647$, $u' = 0.712$, $v' = 0.477$, $w' = 0.722$), (f) $Bn_{tur} = 0.17$ (mass: $1\,kg$, $\sigma = 1.012$, $u' = 1.118$, $v' = 1.251$, $w' = 0.509$) ; Unit of σ, u', v', w': $[m/s]$

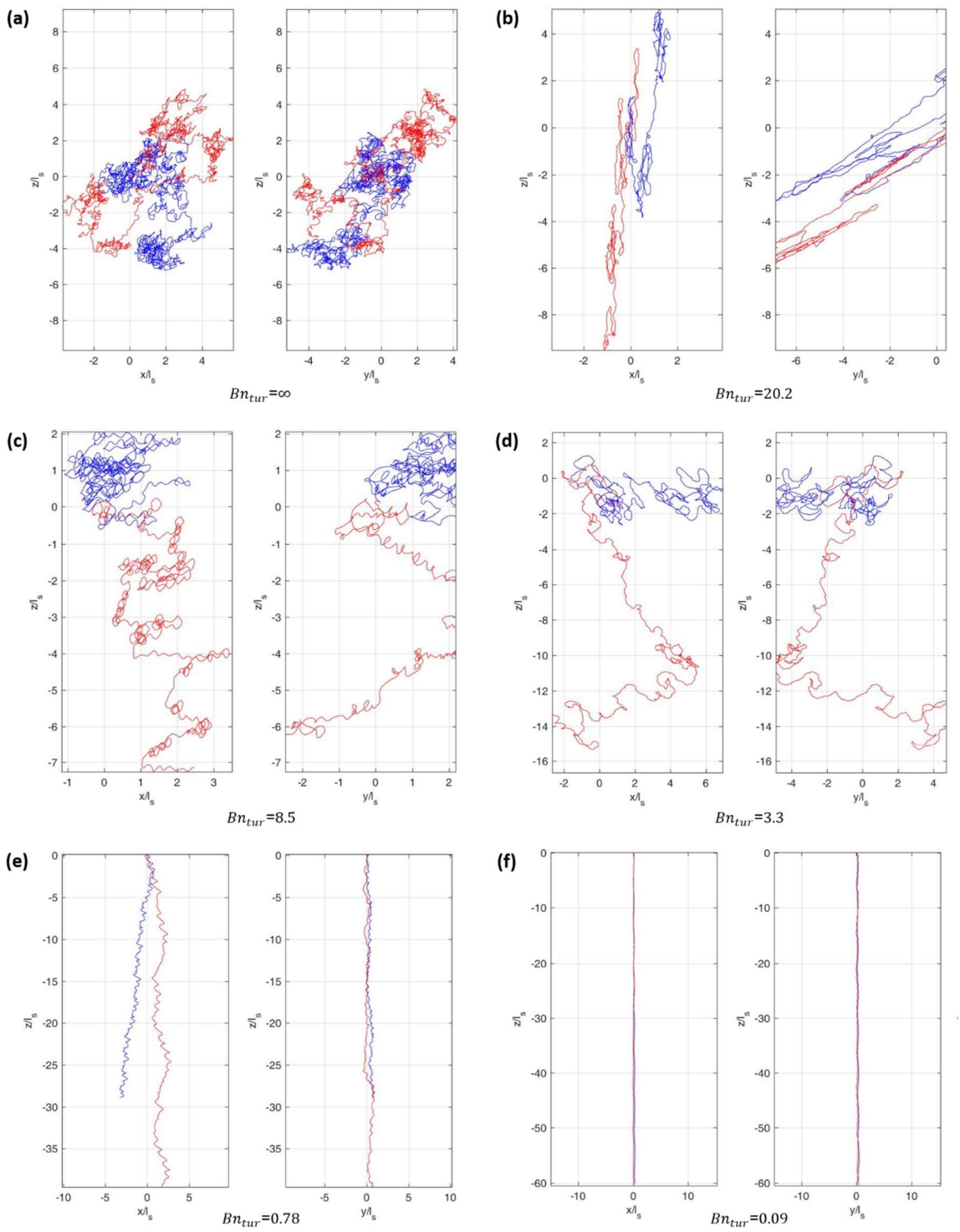

Figure C 4. Trace plots of two different ballooners in an identical homogeneous turbulence. (blue line: a filament-like ballooner, red line: a point-like ballooner; the number of beads: 30, length: 4.45 m, viscosity: 0.2 kg/ms) (a) $Bn_{tur} = \infty$ (mass: $0.61 \times 10^{-4}\,kg$, $\sigma = 0.858$, $u' = 0.803$, $v' = 0.884$, $w' = 0.883$), (b) $Bn_{tur} = 20.2$ (mass: $0.01\,kg$, $\sigma = 1.229$, $u' = 0.475$, $v' = 1.764$, $w' = 1.093$), (c) $Bn_{tur} = 8.5$ (mass: $0.02\,kg$, $\sigma = 1.072$, $u' = 0.984$, $v' = 1.085$, $w' = 1.140$), (d) $Bn_{tur} = 3.3$ (mass: $0.05\,kg$, $\sigma = 1.063$, $u' = 1.106$, $v' = 1.130$, $w' = 0.944$), (e) $Bn_{tur} = 0.78$ (mass: $0.1\,kg$, $\sigma = 0.503$, $u' = 0.593$, $v' = 0.548$, $w' = 0.330$), (f) $Bn_{tur} = 0.09$ (mass: $1\,kg$, $\sigma = 0.554$, $u' = 0.364$, $v' = 0.524$, $w' = 0.716$) ; Unit of σ, u', v', w': $[m/s]$

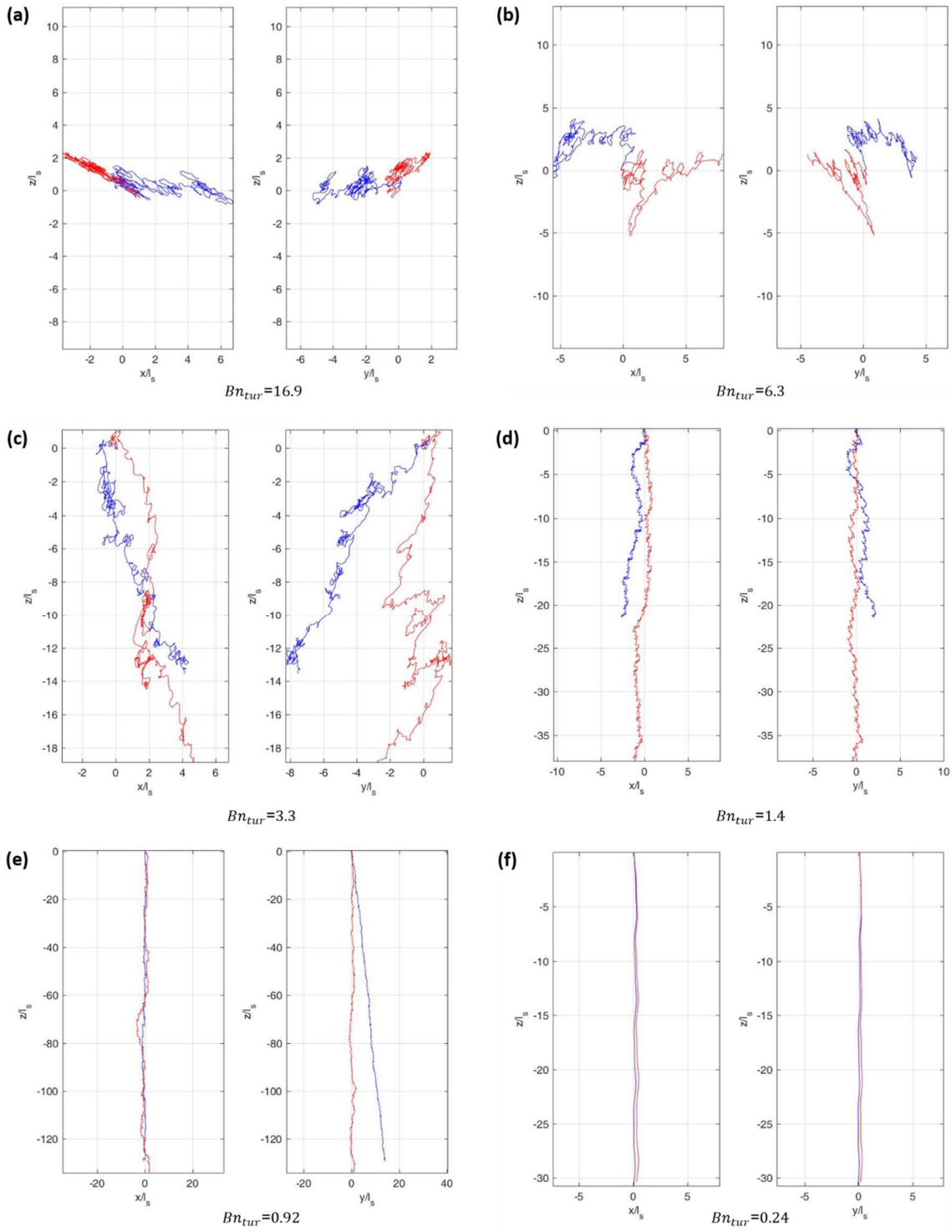

Figure C 5. Trace plots of two different ballooners in an identical homogeneous turbulence. (blue line: a filament-like ballooner, red line: a point-like ballooner; the number of beads: 30, length: 4.45 m, viscosity: 0.2 kg/ms) (a) $Bn_{tur} = 16.9$ (mass: $0.01\,kg$, $\sigma = 1.034$, $u' = 1.365$, $v' = 0.757$, $w' = 0.879$), (b) $Bn_{tur} = 6.3$ (mass: $0.02\,kg$, $\sigma = 0.793$, $u' = 0.695$, $v' = 0.605$, $w' = 1.019$), (c) $Bn_{tur} = 3.3$ (mass: $0.05\,kg$, $\sigma = 1.060$, $u' = 0.849$, $v' = 0.947$, $w' = 1.325$), (d) $Bn_{tur} = 1.4$ (mass: $0.1\,kg$, $\sigma = 0.889$, $u' = 0.889$, $v' = 0.804$, $w' = 0.967$), (e) $Bn_{tur} = 0.92$ (mass: $0.2\,kg$, $\sigma = 1.177$, $u' = 1.130$, $v' = 0.981$, $w' = 1.384$), (f) $Bn_{tur} = 0.24$ (mass: $0.5\,kg$, $\sigma = 0.761$, $u' = 0.860$, $v' = 0.615$, $w' = 0.786$) ; Unit of σ, u', v', w': $[m/s]$

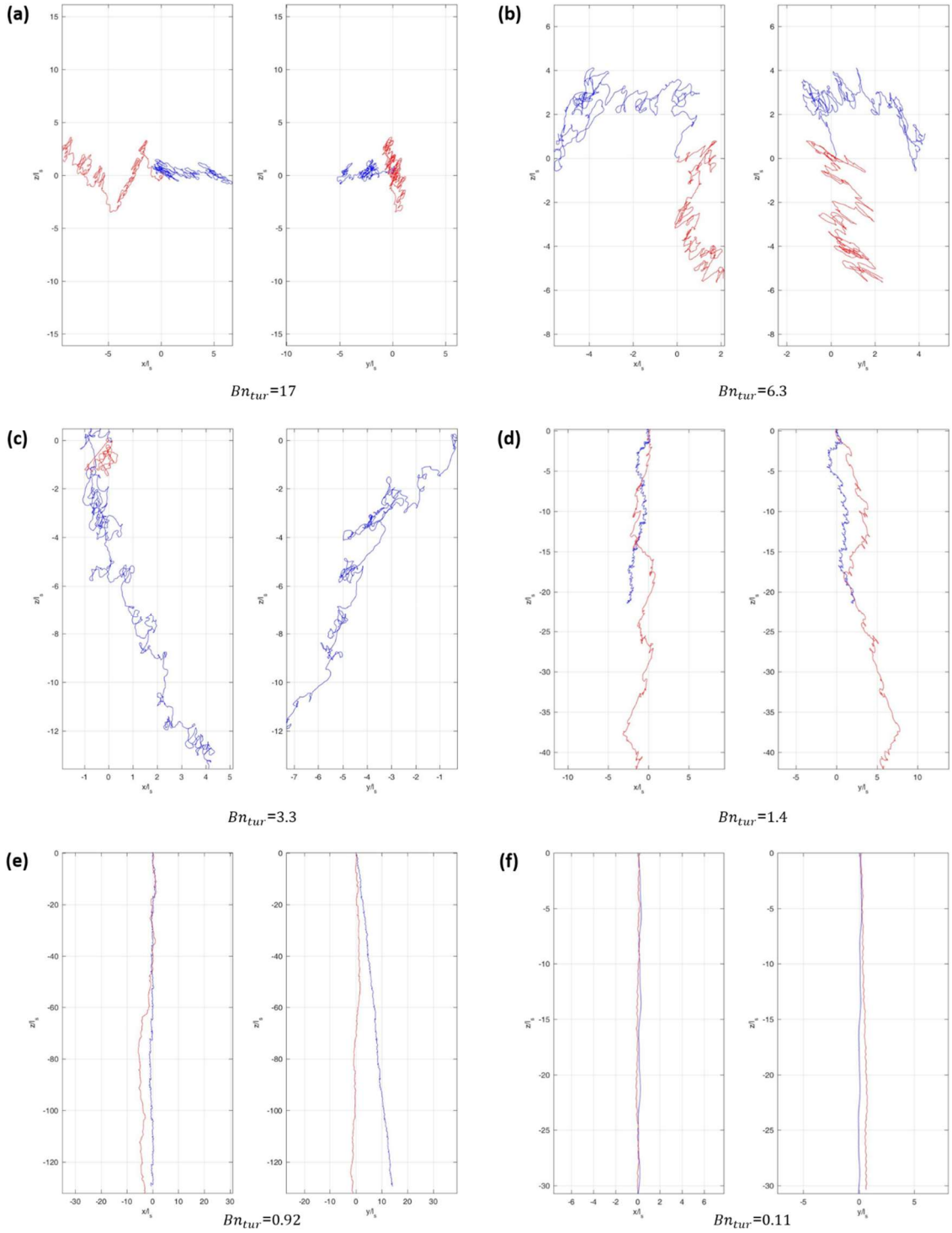

Figure C 6. Trace plots of two different ballooners in an identical homogeneous turbulence. (blue line: a filament-like ballooner, red line: a point-like ballooner; the number of beads: 30, length: 4.45 m, viscosity: 0.2 kg/ms) (a) $Bn_{tur} = 17$ (mass: $0.01\,kg$, $\sigma = 1.034$, $u' = 1.365$, $v' = 0.757$, $w' = 0.879$), (b) $Bn_{tur} = 6.29$ (mass: $0.02\,kg$, $\sigma = 0.793$, $u' = 0.695$, $v' = 0.605$, $w' = 1.019$), (c) $Bn_{tur} = 3.3$ (mass: $0.05\,kg$, $\sigma = 1.060$, $u' = 0.849$, $v' = 0.947$, $w' = 1.325$), (d) $Bn_{tur} = 1.4$ (mass: $0.1\,kg$, $\sigma = 0.889$, $u' = 0.889$, $v' = 0.804$, $w' = 0.967$), (e) $Bn_{tur} = 0.92$ (mass: $0.2\,kg$, $\sigma = 1.177$, $u' = 1.130$, $v' = 0.981$, $w' = 1.384$), (f) $Bn_{tur} = 0.11$ (mass: $1\,kg$, $\sigma = 0.637$, $u' = 0.479$, $v' = 0.844$, $w' = 0.524$) ; Unit of σ, u', v', w': $[m/s]$

C2. Dynamic Motions in a Shear Flow

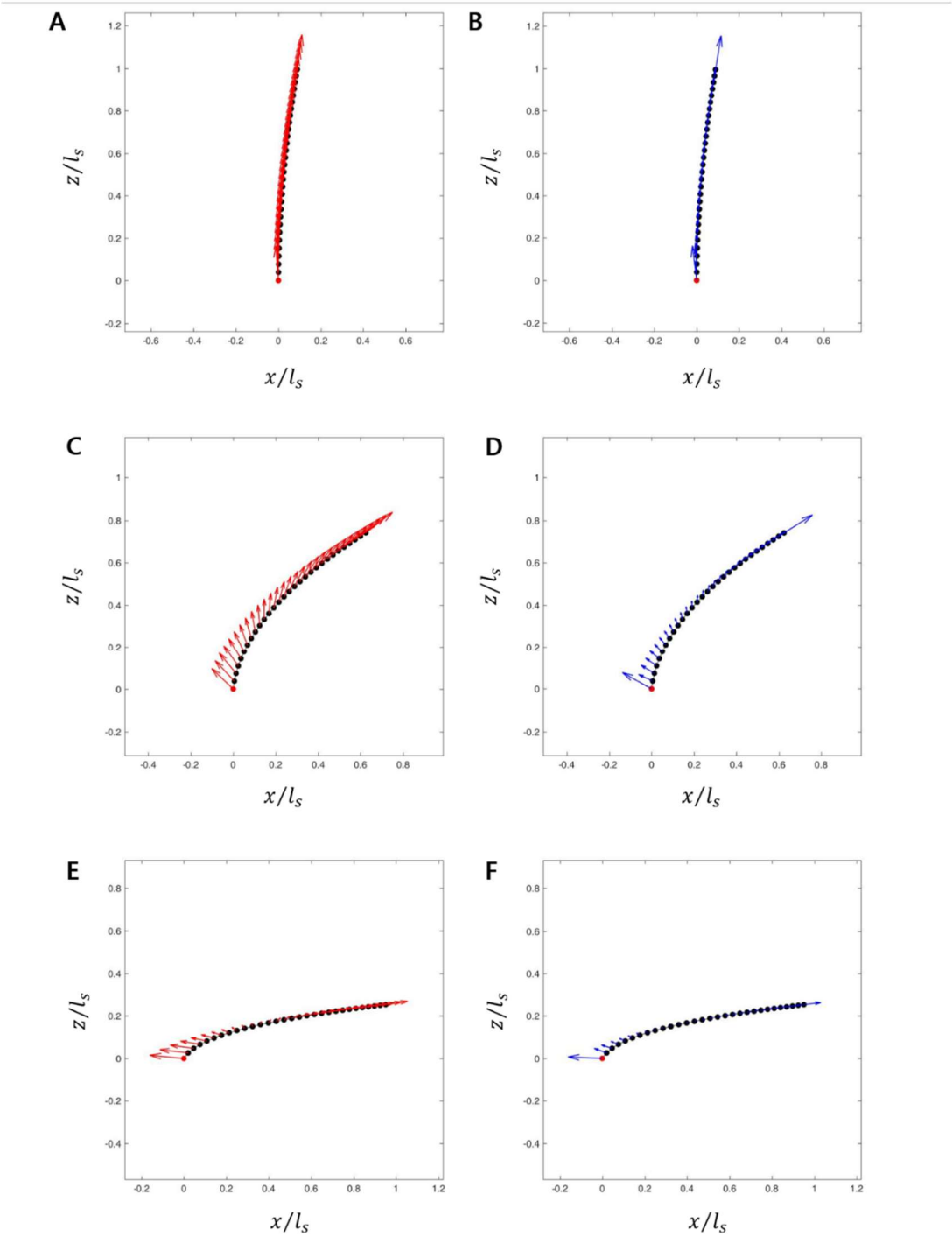

Figure C 7. Relative flow velocity and resistance force vector distributions on the ballooning structure in a shear flow. (A) Velocity vector distribution when Bn_{shear}= 0.104; (B) Force vector distribution when Bn_{shear}= 0.104; (C) Velocity vector distribution when Bn_{shear}= 1.4; (D) Force vector distribution when Bn_{shear}= 1.4. (E) Velocity vector distribution when Bn_{shear}= 20.7; (F) Force vector distribution when Bn_{shear} =20.7. (Red dots indicate weight, while black dots describe a flexible filament structure.)

C3. Dynamic Motions in a Periodic Cellular Flow

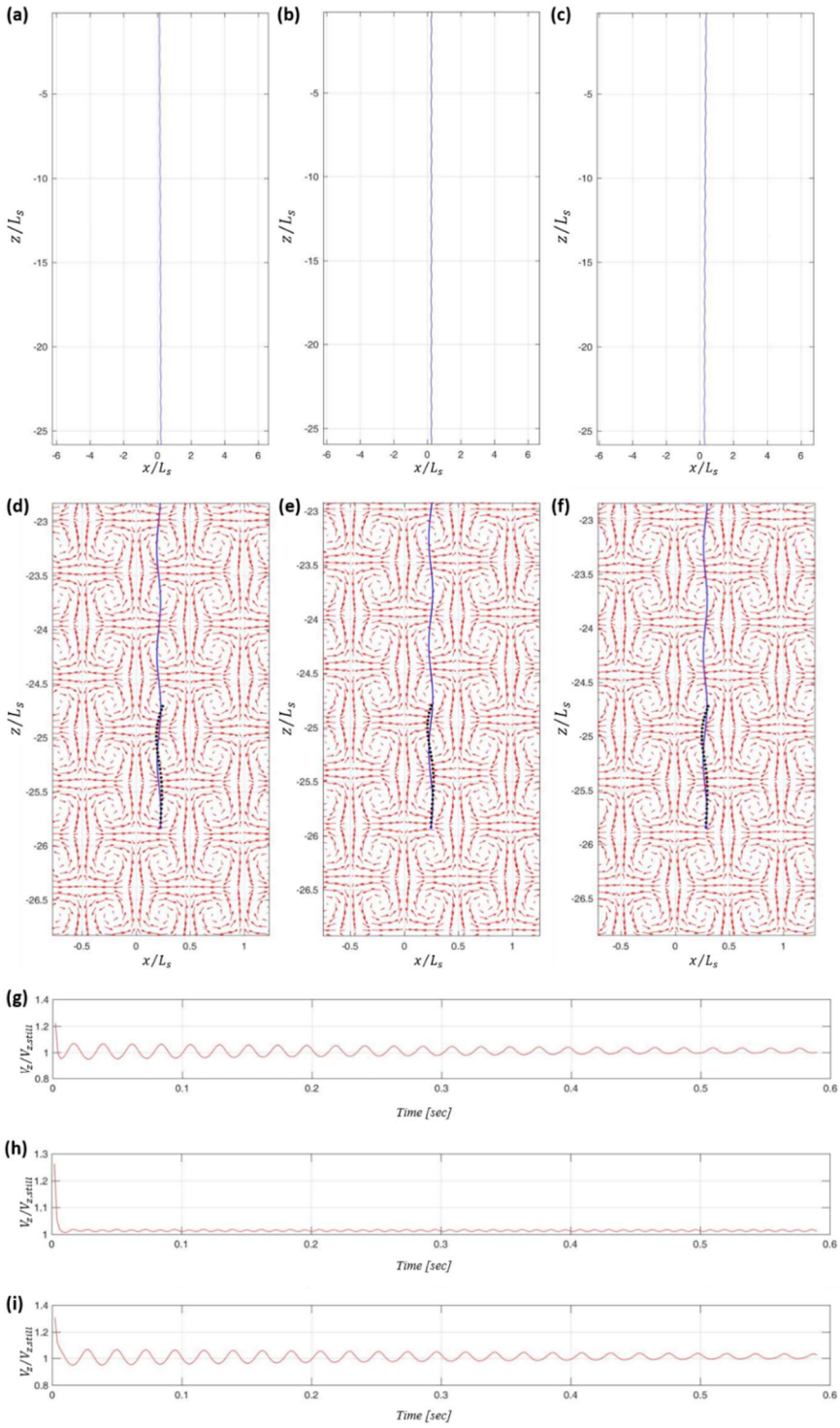

Figure C 8. Eddy crossing $\langle V_z \rangle / V_{z,still} = 1.014$; (a)-(c): Trace plots of a point mass (spider body). (d)-(f): Flow fields and the bead-spring model. (blue lines: trajectory plots). (g)-(i): Nondimensionalised settling speeds over time. $Bn_{vor} = 0.13$ (the number of beads: 30, length: 4.45 m, mass: 1 kg, viscosity: 0.5 kg/ms, vortex velocity: $U_0 = 0.5\, m/s$, size of the vortex cell: $L_c/L_s = 0.5$; (a),(d),(g): $x_0/L_c = 0.25$; (b),(e),(h): $x_0/L_c = 0.5$; (c),(f),(i): $x_0/L_c = 0.75$)

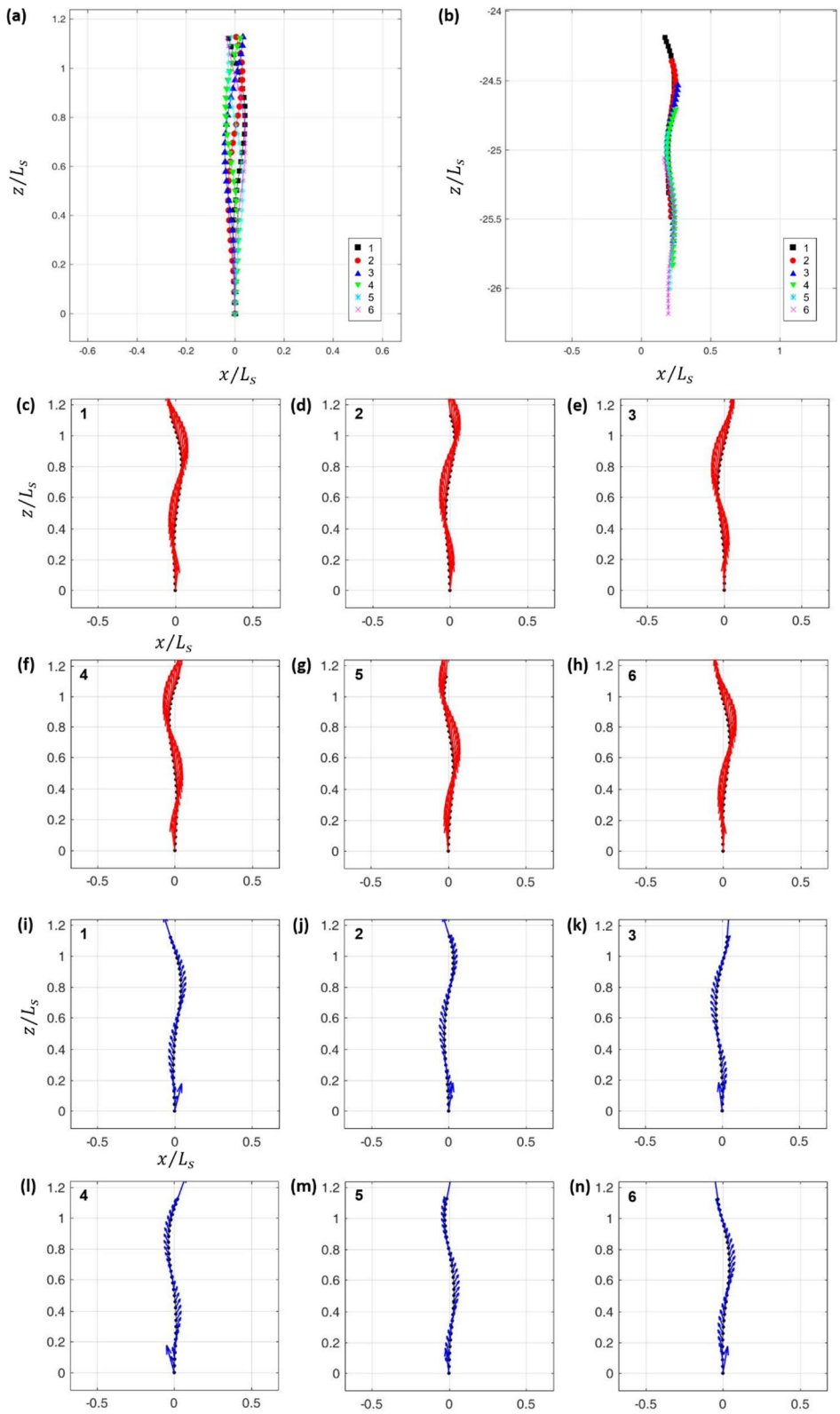

Figure C 9. Eddy crossing $\langle V_z \rangle / V_{z,still} = 1.014$; (a) Shape of a filament during sedimentation in relative coordinate of the lower end. (b) Shape of a filament during sedimentation in absolute coordinate. (c)-(h): Distribution of the relative velocity vectors of the flow. (i)-(n): Distribution of the force vectors by the flow. $Bn_{vor} = 0.13$ (the number of beads: 30, length: 4.45 m, mass: 1 kg, viscosity: 0.5 kg/ms, vortex velocity: $U_0 = 0.5\ m/s$, size of the vortex cell: $L_c/L_s = 0.5$)

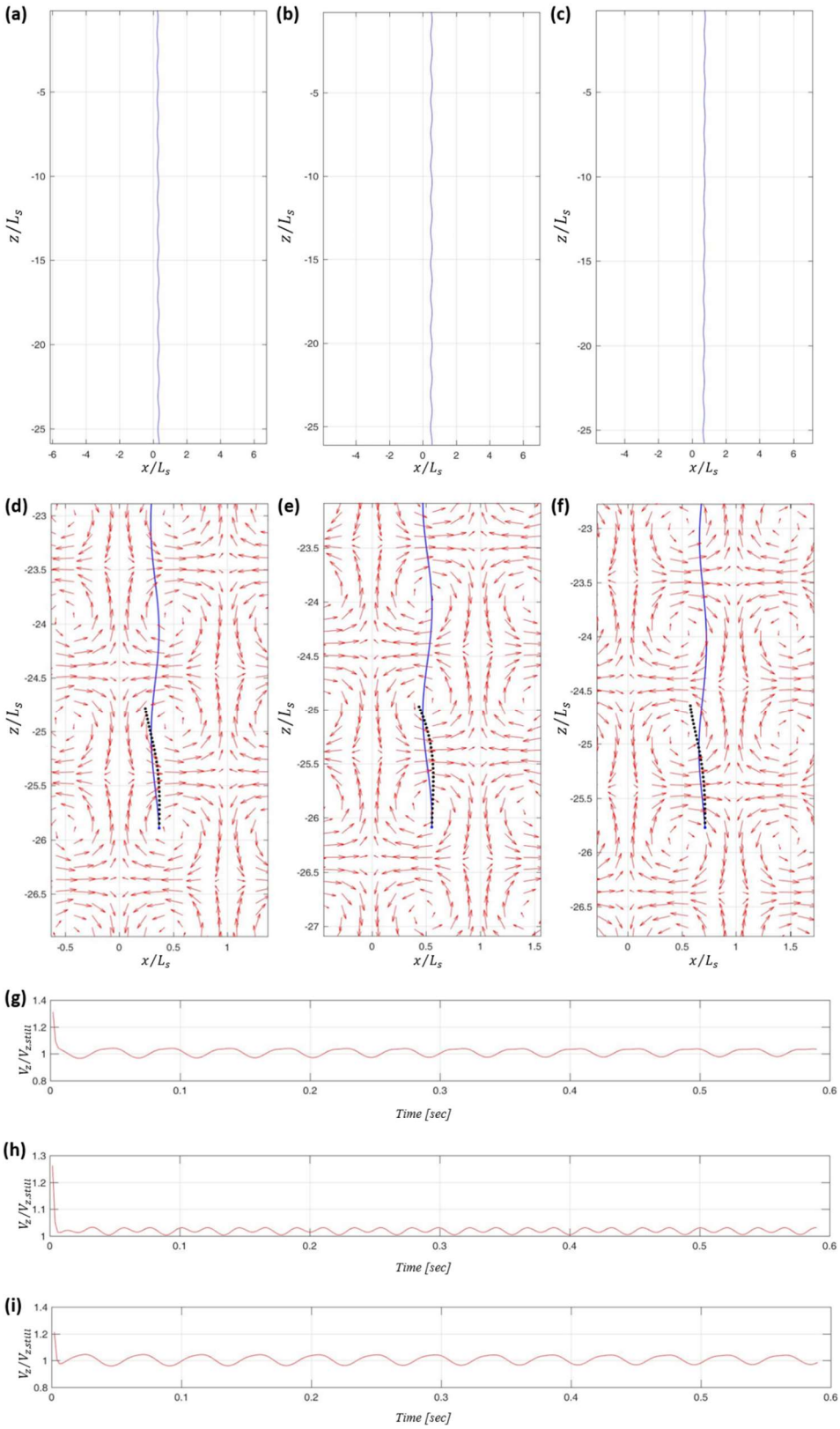

Figure C 10. Eddy crossing $\langle V_z \rangle / V_{z,still} = 1.015$; (a)-(c): Trace plots of a point mass (spider body). (d)-(f): Flow fields and the bead-spring model. (blue lines: trajectory plots). (g)-(i): Nondimensionalised settling speeds over time. $Bn_{vor} = 0.13$ (the number of beads: 30, length: 4.45 m, mass: 1 kg, viscosity: 0.5 kg/ms, vortex velocity: $U_0 = 0.5\ m/s$, size of the vortex cell: $L_c/L_s = 1$; (a),(d),(g): $x_0/L_c = 0.25$; (b),(e),(h): $x_0/L_c = 0.5$; (c),(f),(i): $x_0/L_c = 0.75$)

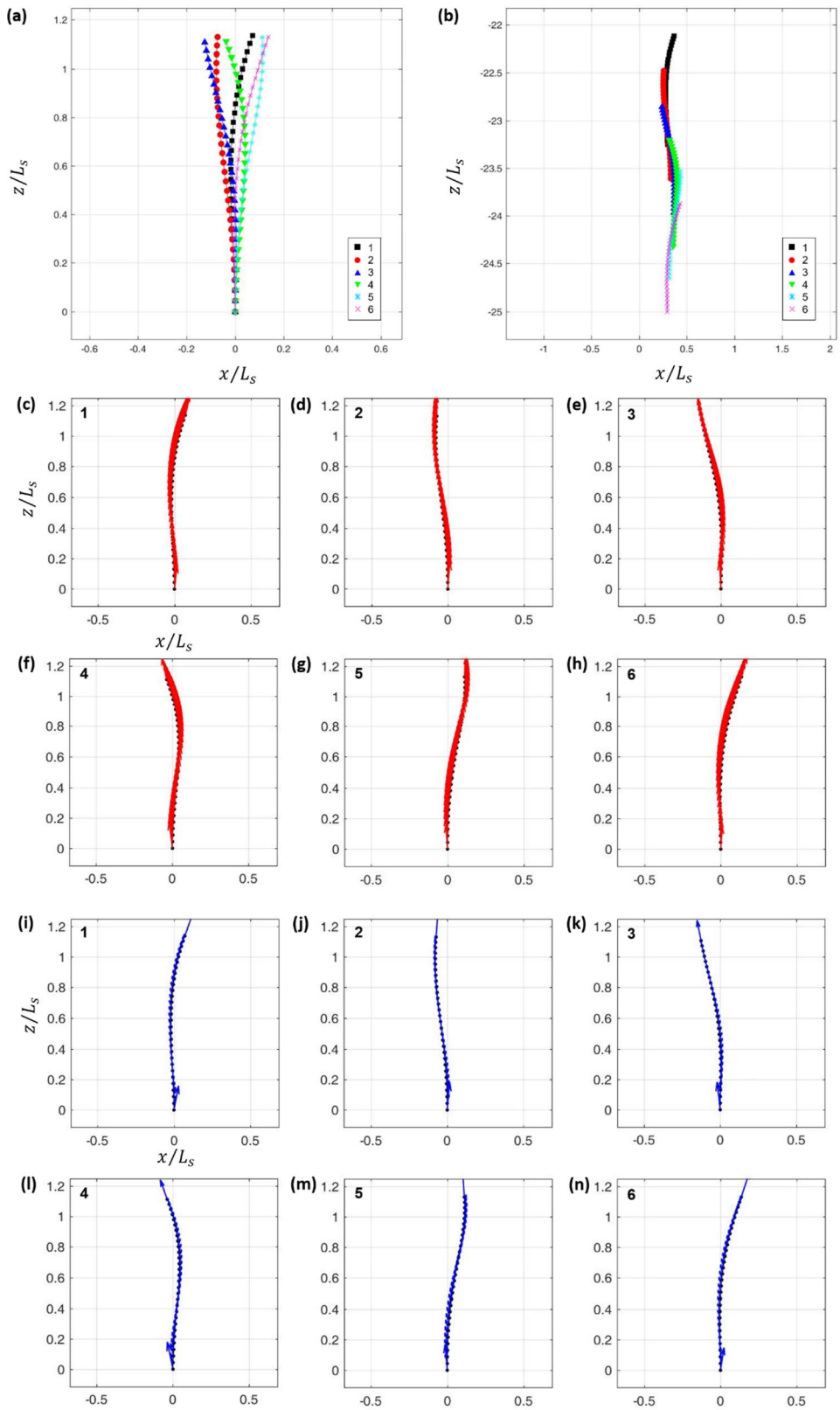

Figure C 11. Eddy crossing $\langle V_z \rangle / V_{z,still} = 1.015$; (a) Shape of a filament during sedimentation in relative coordinate of the lower end. (b) Shape of a filament during sedimentation in absolute coordinate. (c)-(h): Distribution of the relative velocity vectors of the flow. (i)-(n): Distribution of the force vectors by the flow. $Bn_{vor} = 0.13$ (the number of beads: 30, length: 4.45 m, mass: 1 kg, viscosity: 0.5 kg/ms, vortex velocity: $U_0 = 0.5\ m/s$, size of the vortex cell: $L_c/L_s = 1$)

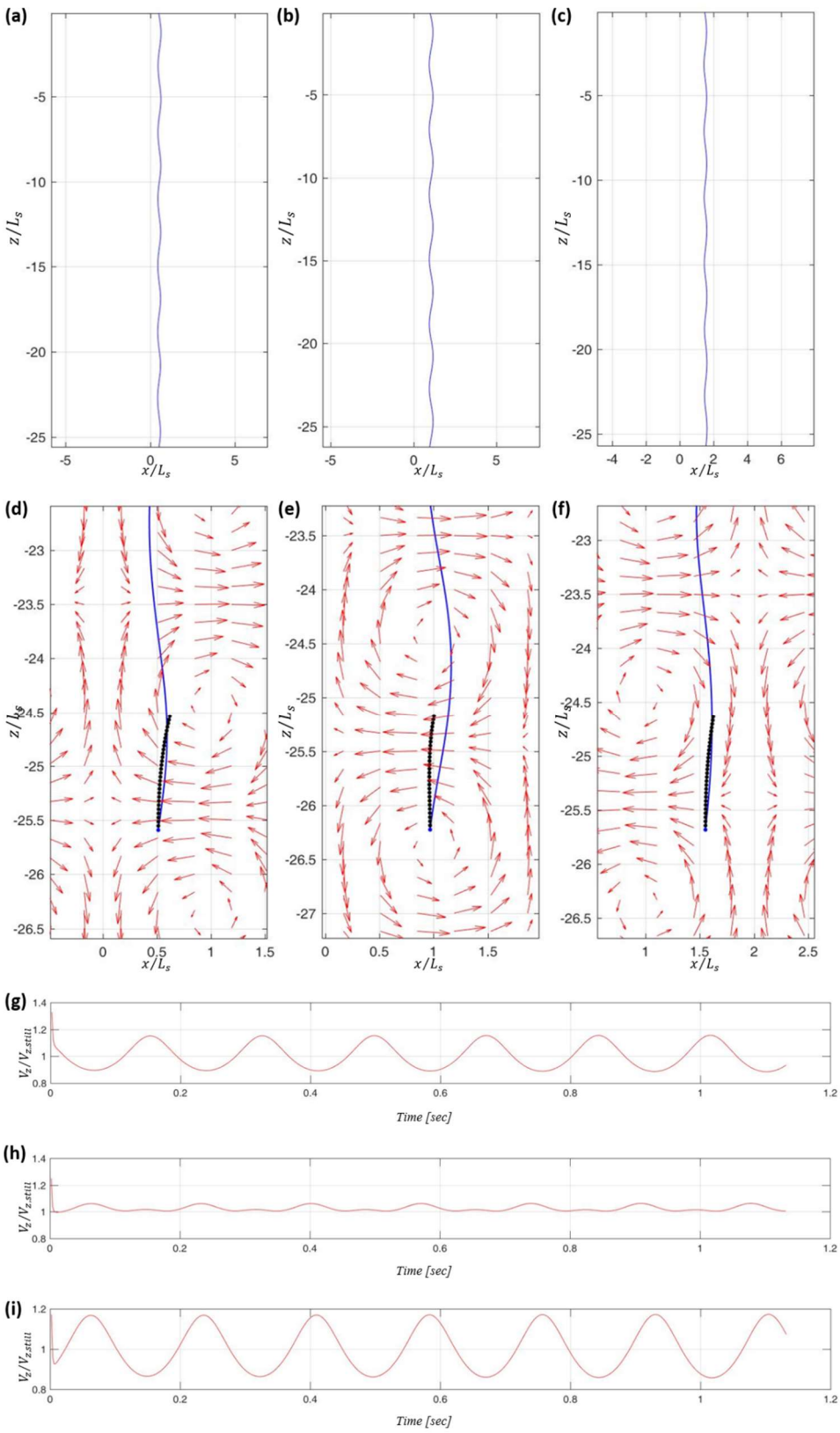

Figure C 12. Eddy crossing $\langle V_z \rangle / V_{z,still} = 1.001$; (a)-(c): Trace plots of a point mass (spider body). (d)-(f): Flow fields and the bead-spring model. (blue lines: trajectory plots). (g)-(i): Nondimensionalised settling speeds over time. $Bn_{vor} = 0.13$ (the number of beads: 30, length: 4.45 m, mass: 1 kg, viscosity: 0.5 kg/ms, vortex velocity: $U_0 = 0.5\ m/s$, size of the vortex cell: $L_c/L_s = 2$; (a),(d),(g): $x_0/L_c = 0.25$; (b),(e),(h): $x_0/L_c = 0.5$; (c),(f),(i): $x_0/L_c = 0.75$)

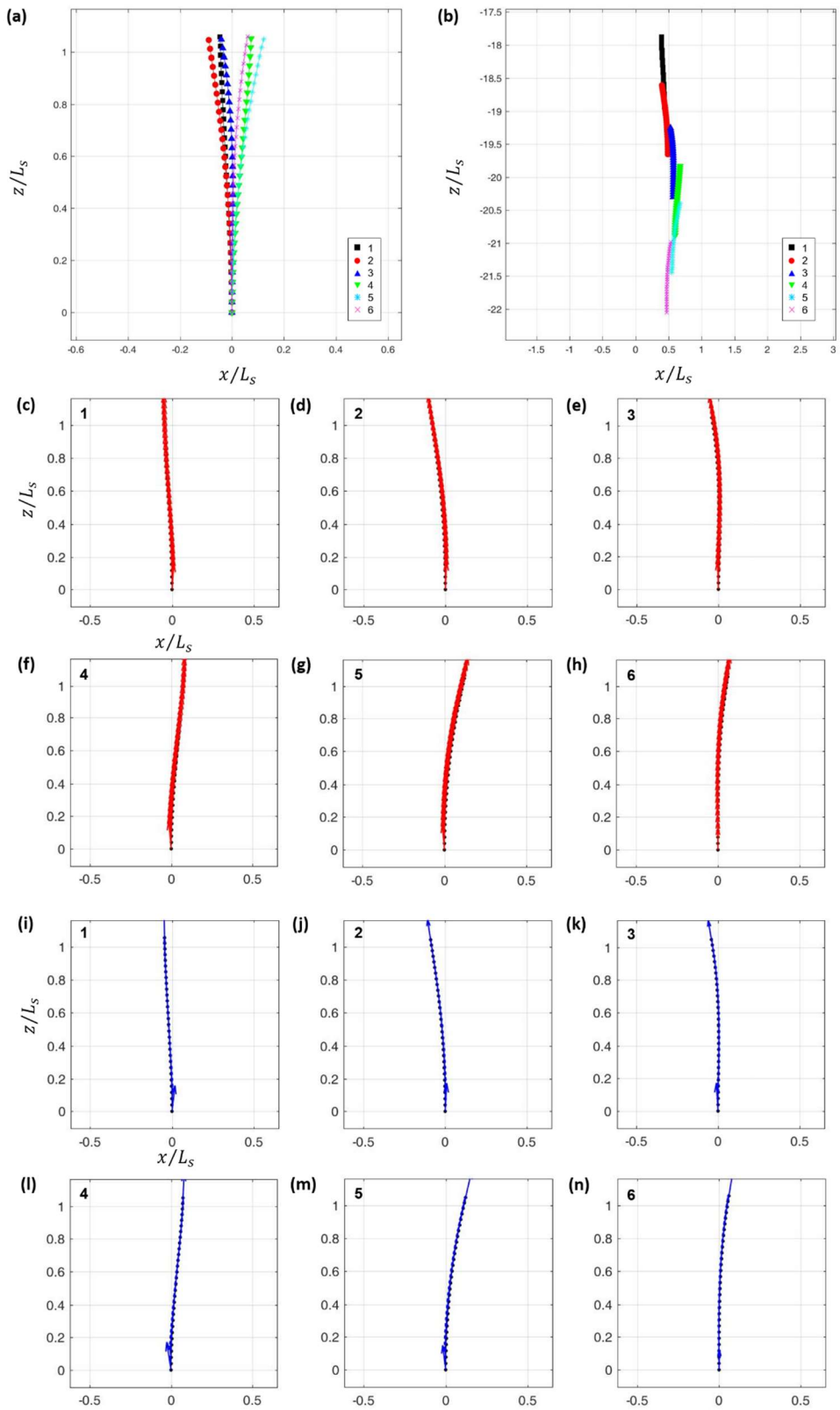

Figure C 13. Eddy crossing $\langle V_z \rangle / V_{z,still} = 1.001$; (a) Shape of a filament during sedimentation in relative coordinate of the lower end. (b) Shape of a filament during sedimentation in absolute coordinate. (c)-(h): Distribution of the relative velocity vectors of the flow. (i)-(n): Distribution of the force vectors by the flow. $Bn_{vor} = 0.13$ (the number of beads: 30, length: 4.45 m, mass: 1 kg, viscosity: 0.5 kg/ms, vortex velocity: $U_0 = 0.5\ m/s$, size of the vortex cell: $L_c/L_s = 2$)

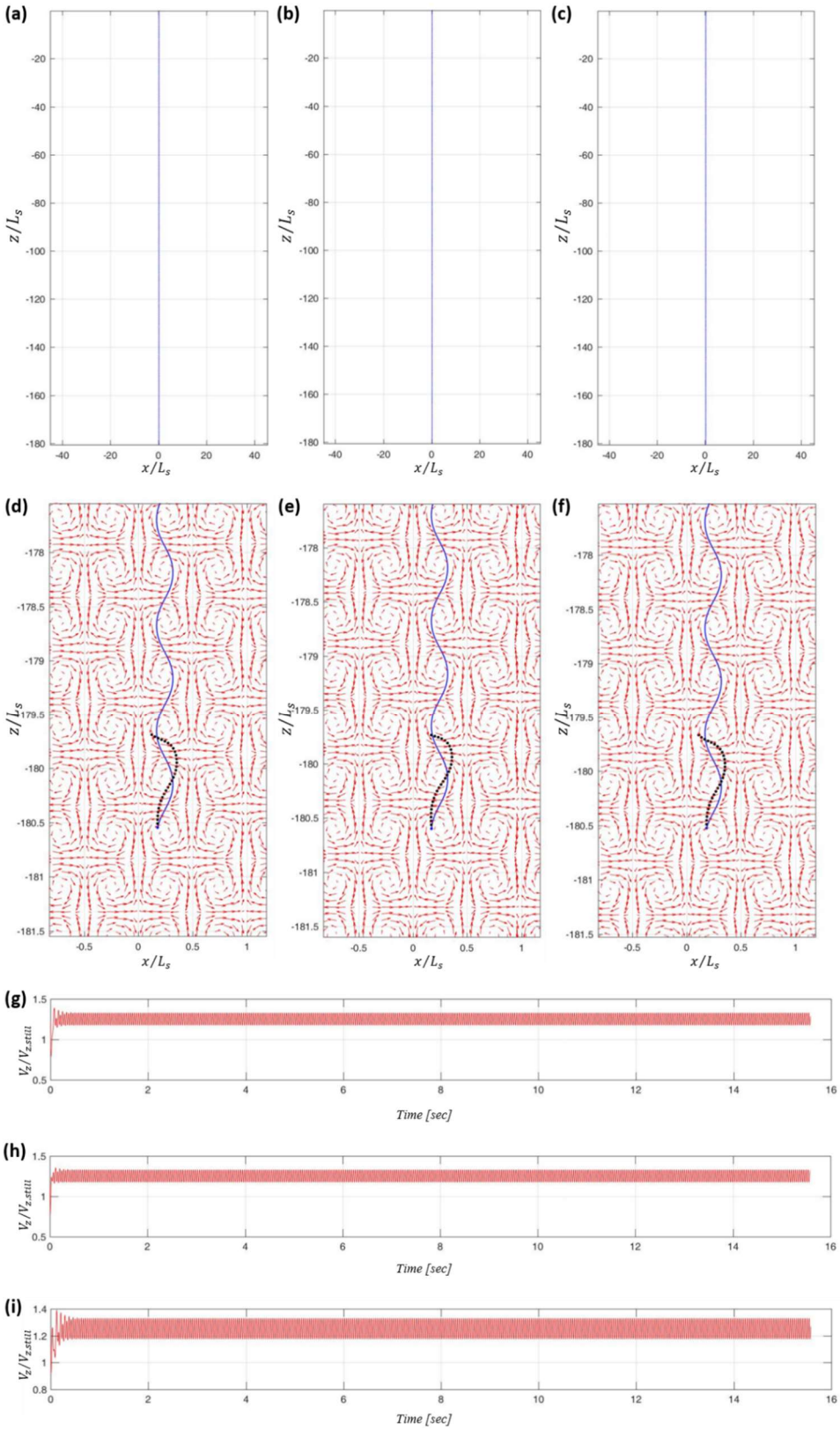

Figure C 14. Fast settling $\langle V_z \rangle / V_{z,still} = 1.251$; (a)-(c): Trace plots of a point mass (spider body). (d)-(f): Flow fields and the bead-spring model. (blue lines: trajectory plots). (g)-(i): Nondimensionalised settling speeds over time. $Bn_{vor} = 0.58$ (the number of beads: 30, length: 4.45 m, mass: 0.2 kg, viscosity: 0.5 kg/ms, vortex velocity: $U_0 = 0.5\, m/s$, size of the vortex cell: $L_c/L_s = 0.5$; (a),(d),(g): $x_0/L_c = 0.25$; (b),(e),(h): $x_0/L_c = 0.5$; (c),(f),(i): $x_0/L_c = 0.75$)

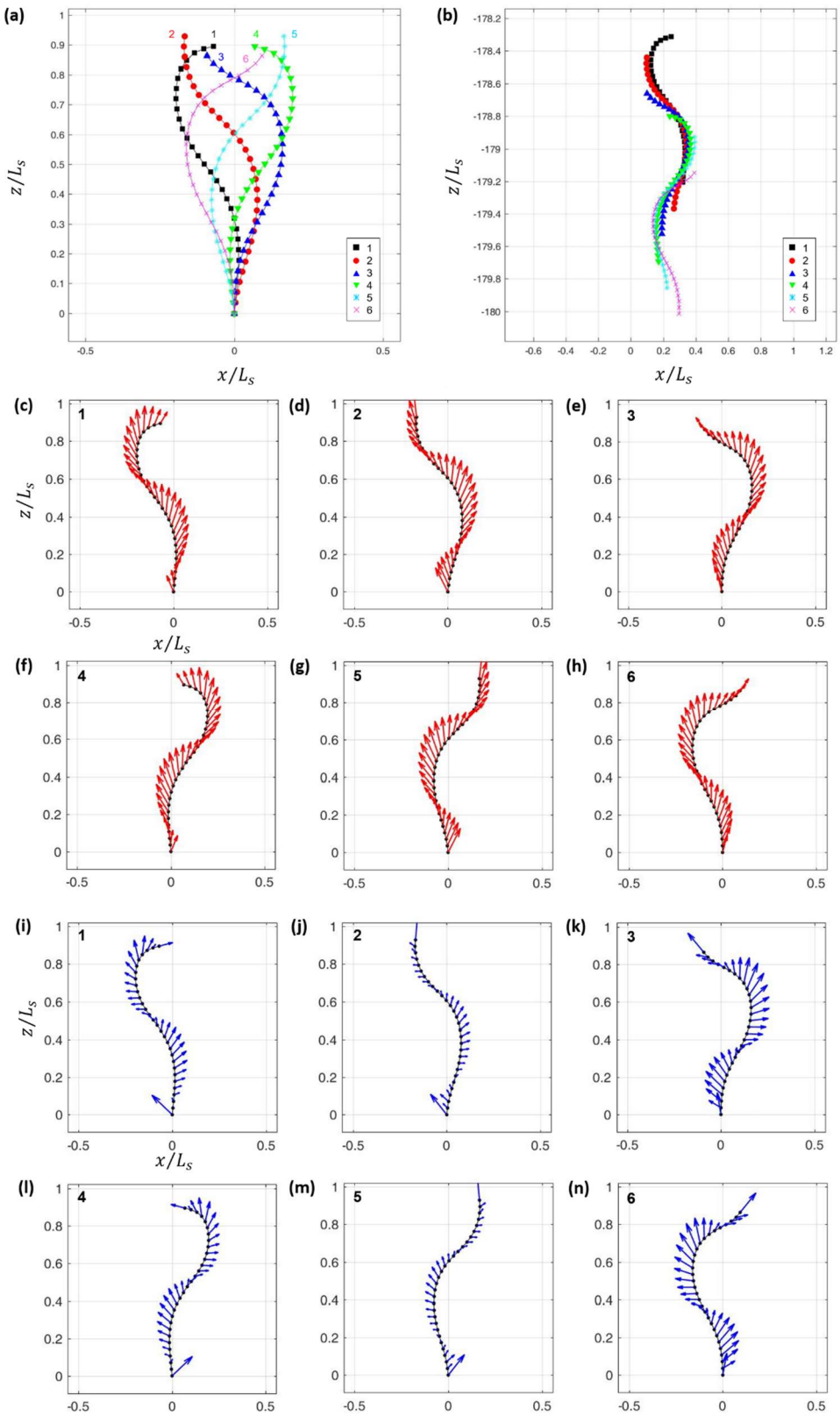

Figure C 15. Fast settling $\langle V_z \rangle / V_{z,still} = 1.251$; (a) Shape of a filament during sedimentation in relative coordinate of the lower end. (b) Shape of a filament during sedimentation in absolute coordinate. (c)-(h): Distribution of the relative velocity vectors of the flow. (i)-(n): Distribution of the force vectors by the flow. $Bn_{vor} = 0.58$ (the number of beads: 30, length: 4.45 m, mass: 0.2 kg, viscosity: 0.5 kg/ms, vortex velocity: $U_0 = 0.5\ m/s$, size of the vortex cell: $L_c/L_s = 0.5$)

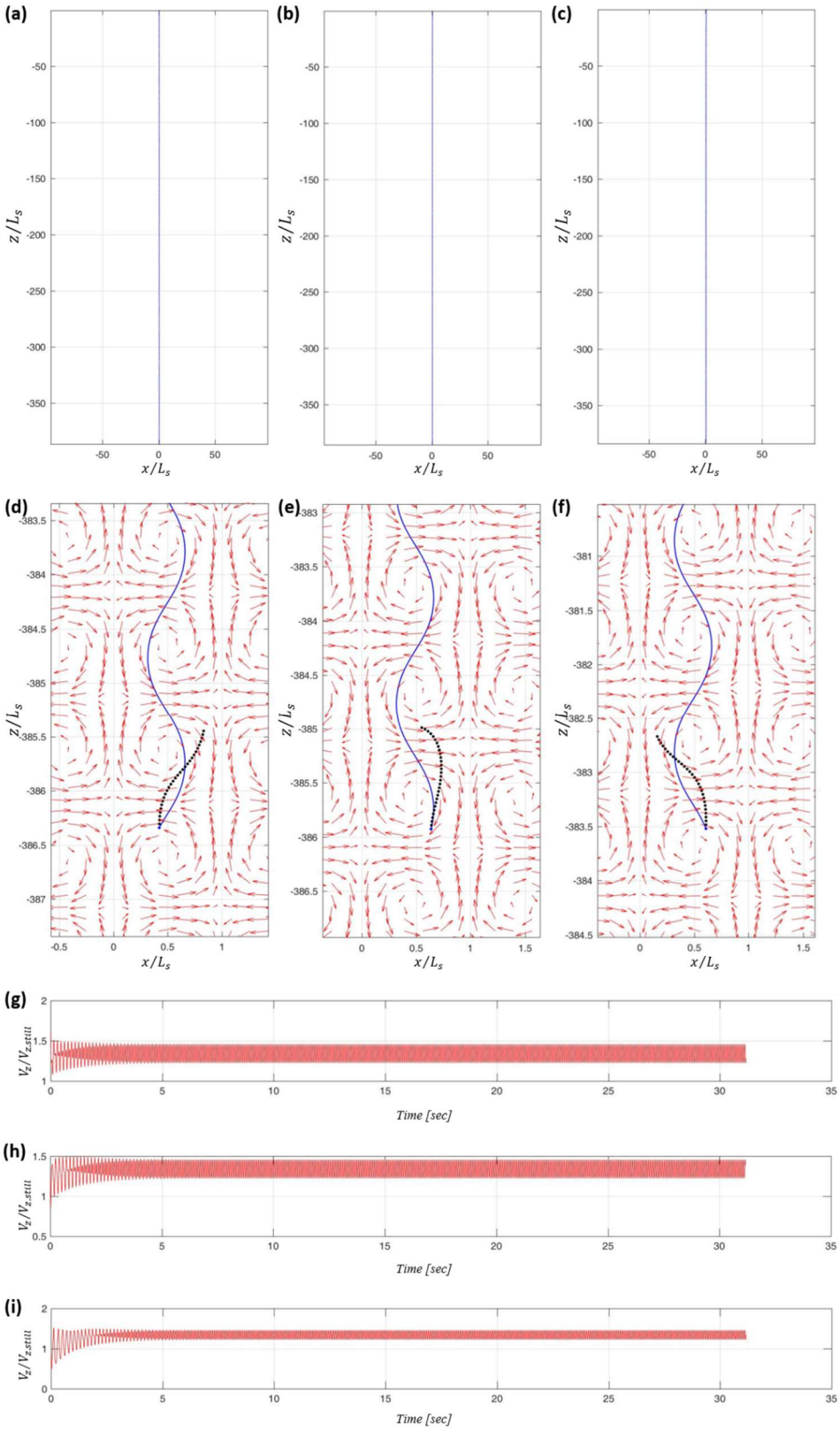

Figure C 16. Fast settling $\langle V_z \rangle / V_{z,still} = 1.328$; (a)-(c): Trace plots of a point mass (spider body). (d)-(f): Flow fields and the bead-spring model. (blue lines: trajectory plots). (g)-(i): Nondimensionalised settling speeds over time. $Bn_{vor} = 0.58$ (the number of beads: 30, length: 4.45 m, mass: 0.2 kg, viscosity: 0.5 kg/ms, vortex velocity: $U_0 = 0.5\ m/s$, size of the vortex cell: $L_c/L_s = 1$; (a),(d),(g): $x_0/L_c = 0.25$; (b),(e),(h): $x_0/L_c = 0.5$; (c),(f),(i): $x_0/L_c = 0.75$)

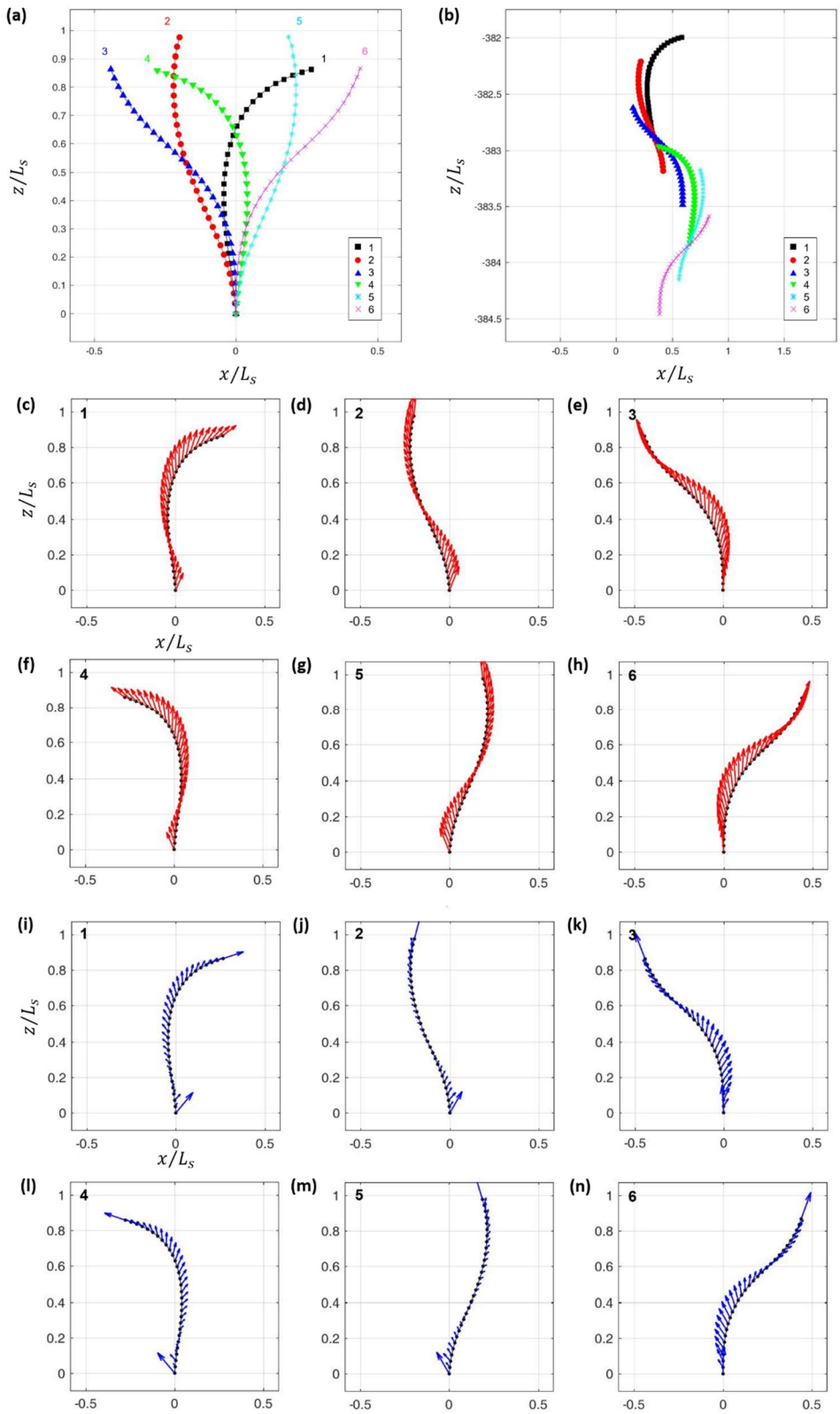

Figure C 17. Fast settling $\langle V_z \rangle / V_{z,still} = 1.328$; (a) Shape of a filament during sedimentation in relative coordinate of the lower end. (b) Shape of a filament during sedimentation in absolute coordinate. (c)-(h): Distribution of the relative velocity vectors of the flow. (i)-(n): Distribution of the force vectors by the flow. $Bn_{vor} = 0.58$ (the number of beads: 30, length: 4.45 m, mass: 0.2 kg, viscosity: 0.5 kg/ms, vortex velocity: $U_0 = 0.5\ m/s$, size of the vortex cell: $L_c/L_s = 1$)

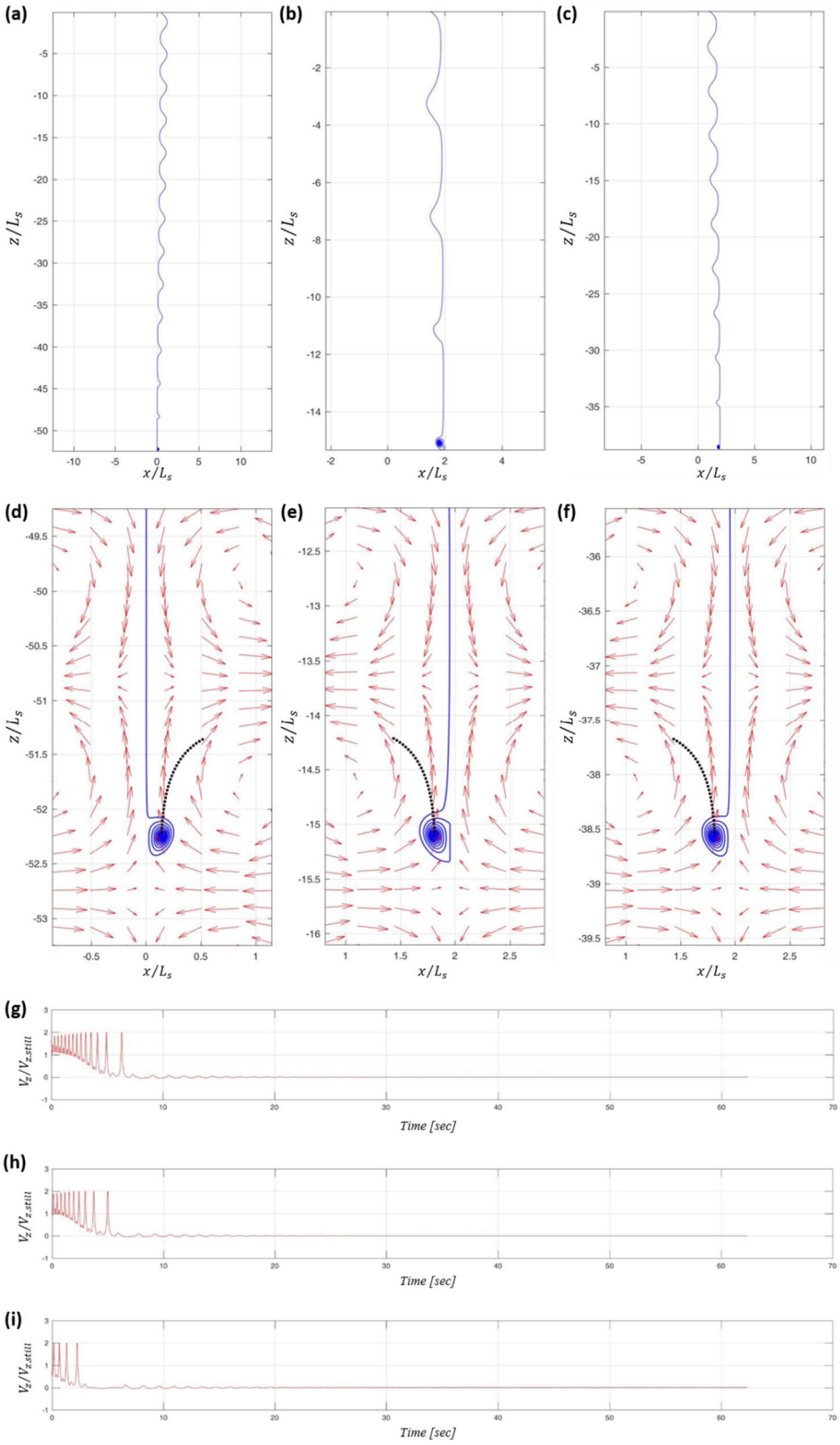

Figure C 18. Trapping $\langle V_z \rangle / V_{z,still} = 0$; (a)-(c): Trace plots of a point mass (spider body). (d)-(f): Flow fields and the bead-spring model. (blue lines: trajectory plots). (g)-(i): Nondimensionalised settling speeds over time. $Bn_{vor} = 0.58$ (the number of beads: 30, length: 4.45 m, mass: 0.2 kg, viscosity: 0.5 kg/ms, vortex velocity: $U_0 = 0.5\ m/s$, size of the vortex cell: $L_c/L_s = 2$; (a),(d),(g): $x_0/L_c = 0.25$; (b),(e),(h): $x_0/L_c = 0.5$; (c),(f),(i): $x_0/L_c = 0.75$)

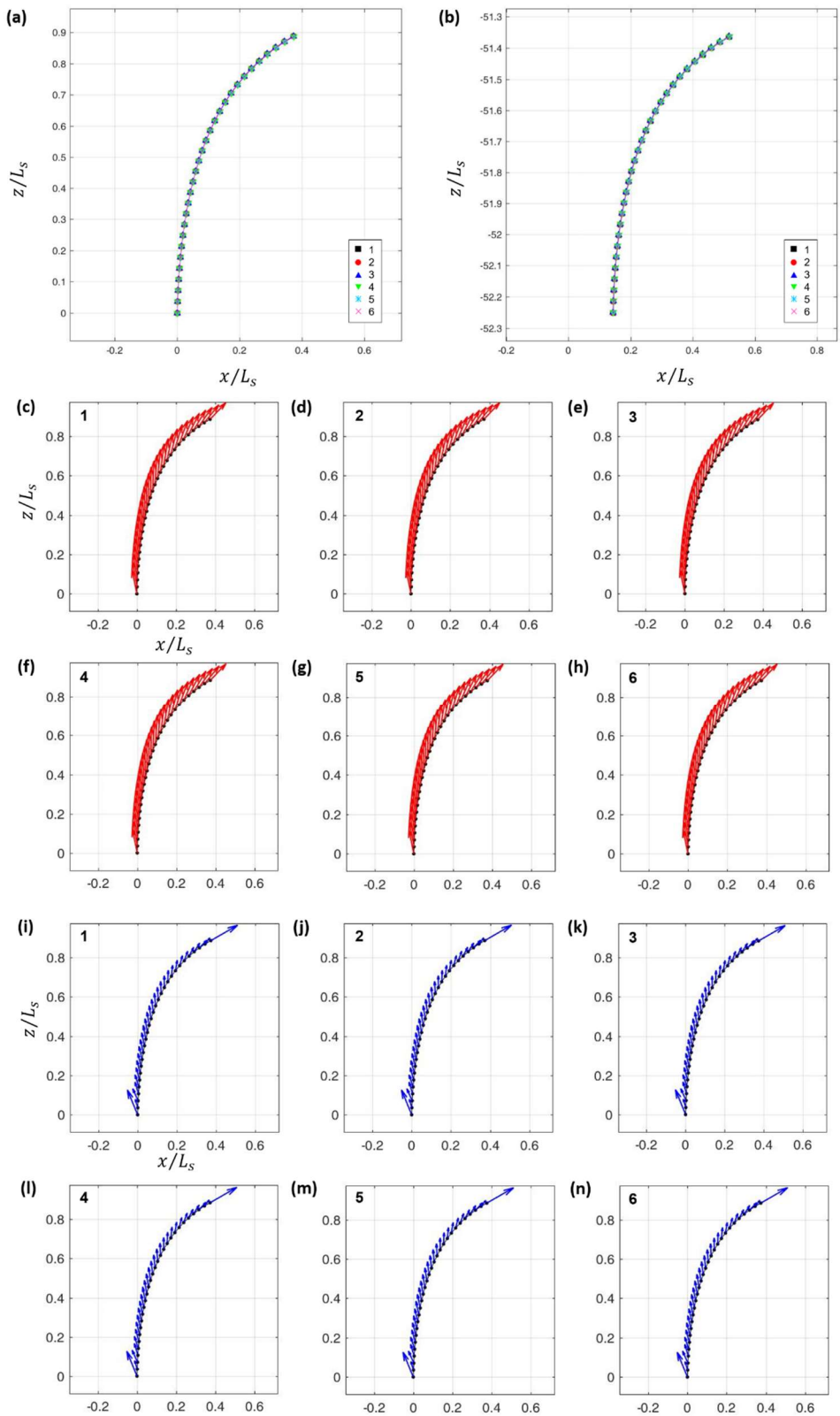

Figure C 19. Trapping $\langle V_z \rangle / V_{z,still} = 0$; (a) Shape of a filament during sedimentation in relative coordinate of the lower end. (b) Shape of a filament during sedimentation in absolute coordinate. (c)-(h): Distribution of the relative velocity vectors of the flow. (i)-(n): Distribution of the force vectors by the flow. $Bn_{vor} = 0.58$ (the number of beads: 30, length: 4.45 m, mass: 0.2 kg, viscosity: 0.5 kg/ms, vortex velocity: $U_0 = 0.5\, m/s$, size of the vortex cell: $L_c/L_s = 2$)

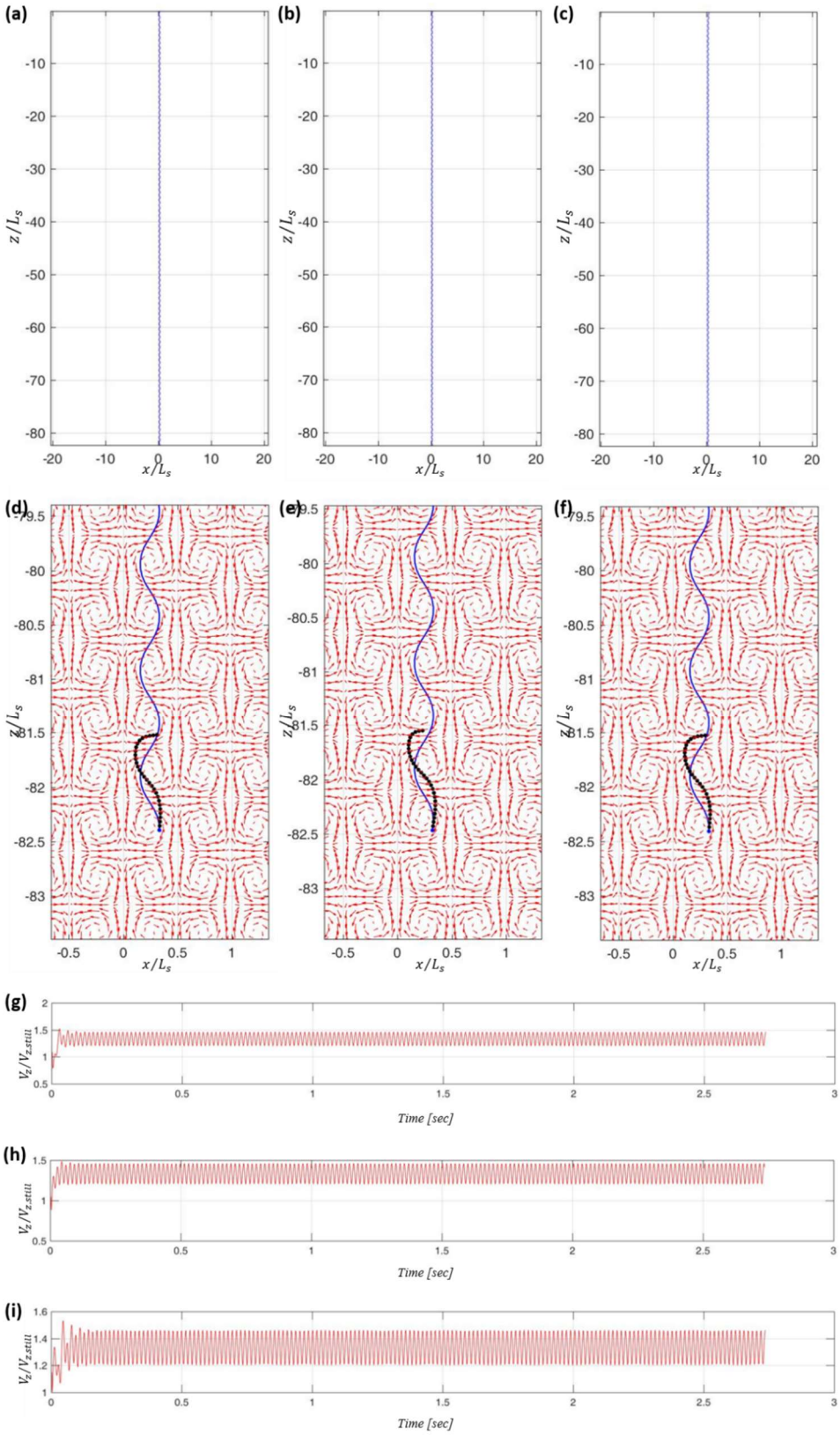

Figure C 20. Fast settling $\langle V_z \rangle / V_{z,still} = 1.335$; (a)-(c): Trace plots of a point mass (spider body). (d)-(f): Flow fields and the bead-spring model. (blue lines: trajectory plots). (g)-(i): Nondimensionalised settling speeds over time. $Bn_{vor} = 0.72$ (the number of beads: 30, length: 4.45 m, mass: 0.5 kg, viscosity: 0.5 kg/ms, vortex velocity: $U_0 = 1.5\ m/s$, size of the vortex cell: $L_c/L_s = 0.5$; (a),(d),(g): $x_0/L_c = 0.25$; (b),(e),(h): $x_0/L_c = 0.5$; (c),(f),(i): $x_0/L_c = 0.75$)

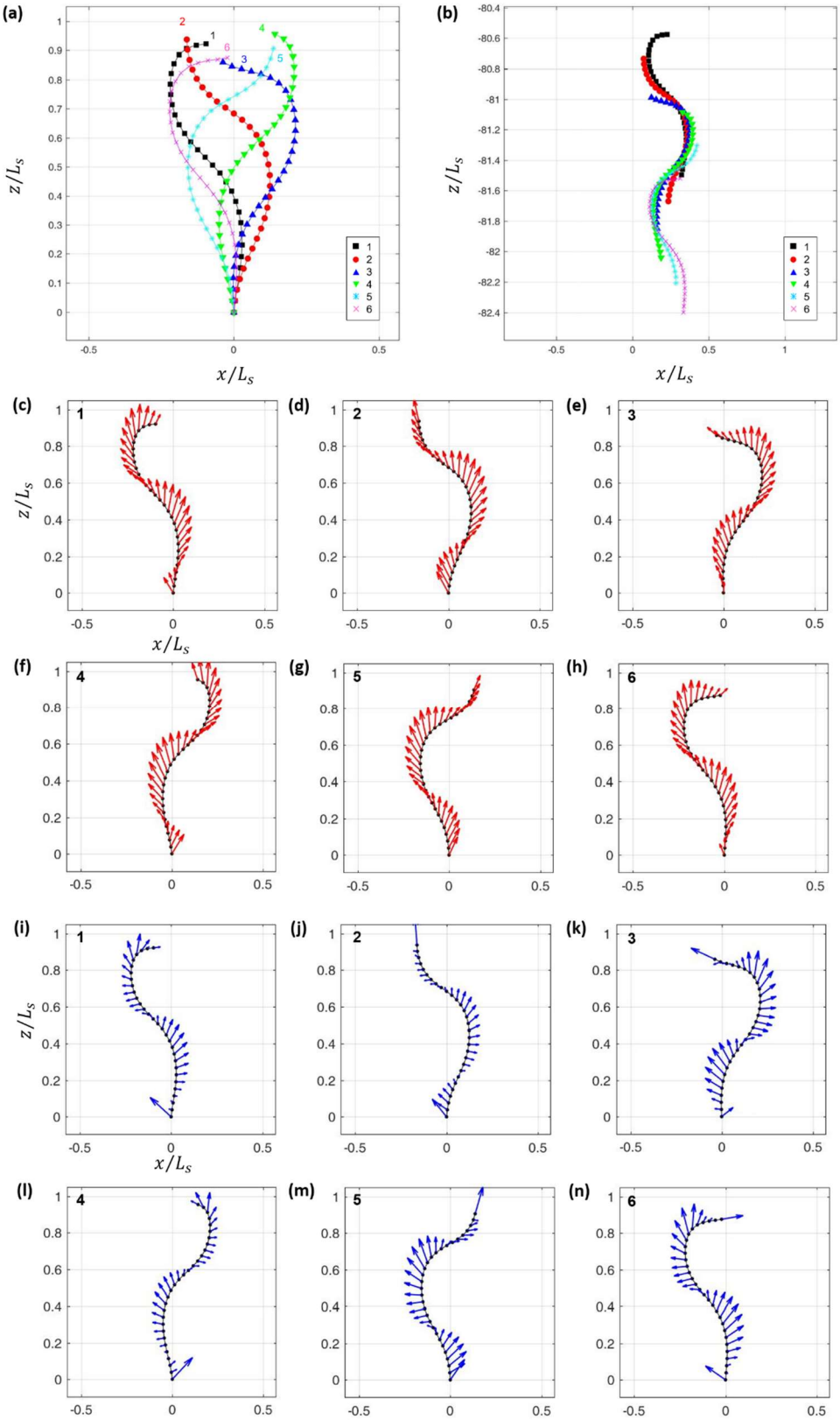

Figure C 21. Fast settling $\langle V_z \rangle / V_{z,still} = 1.335$; (a) Shape of a filament during sedimentation in relative coordinate of the lower end. (b) Shape of a filament during sedimentation in absolute coordinate. (c)-(h): Distribution of the relative velocity vectors of the flow. (i)-(n): Distribution of the force vectors by the flow. $Bn_{vor} = 0.72$ (the number of beads: 30, length: 4.45 m, mass: 0.5 kg, viscosity: 0.5 kg/ms, vortex velocity: $U_0 = 1.5\ m/s$, size of the vortex cell: $L_c/L_s = 0.5$)

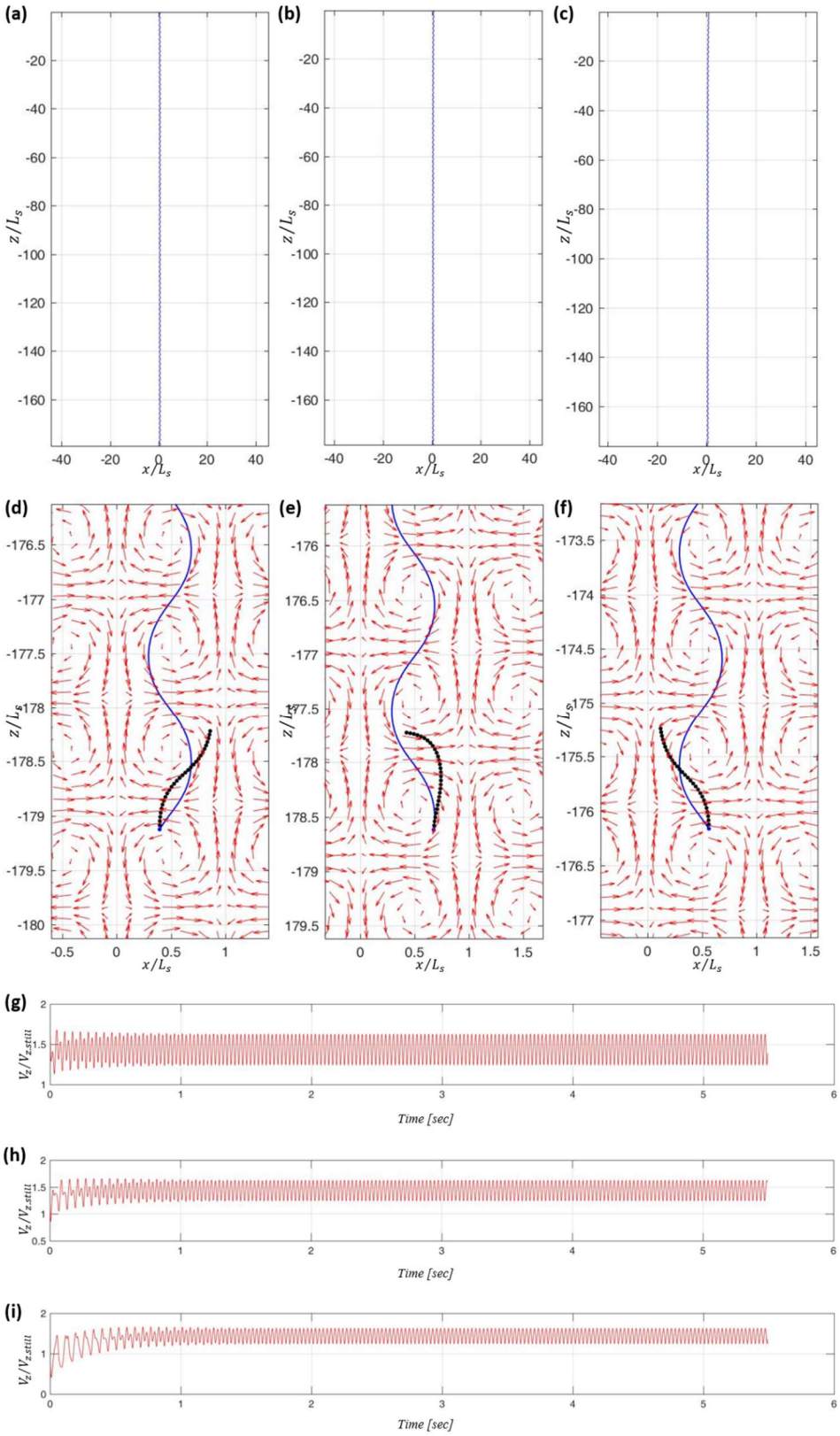

Figure C 22. Fast settling $\langle V_z \rangle / V_{z,still} = 1.446$; (a)-(c): Trace plots of a point mass (spider body). (d)-(f): Flow fields and the bead-spring model. (blue lines: trajectory plots). (g)-(i): Nondimensionalised settling speeds over time. $Bn_{vor} = 0.72$ (the number of beads: 30, length: 4.45 m, mass: 0.5 kg, viscosity: 0.5 kg/ms, vortex velocity: $U_0 = 1.5\ m/s$, size of the vortex cell: $L_c/L_s = 1$; (a),(d),(g): $x_0/L_c = 0.25$; (b),(e),(h): $x_0/L_c = 0.5$; (c),(f),(i): $x_0/L_c = 0.75$)

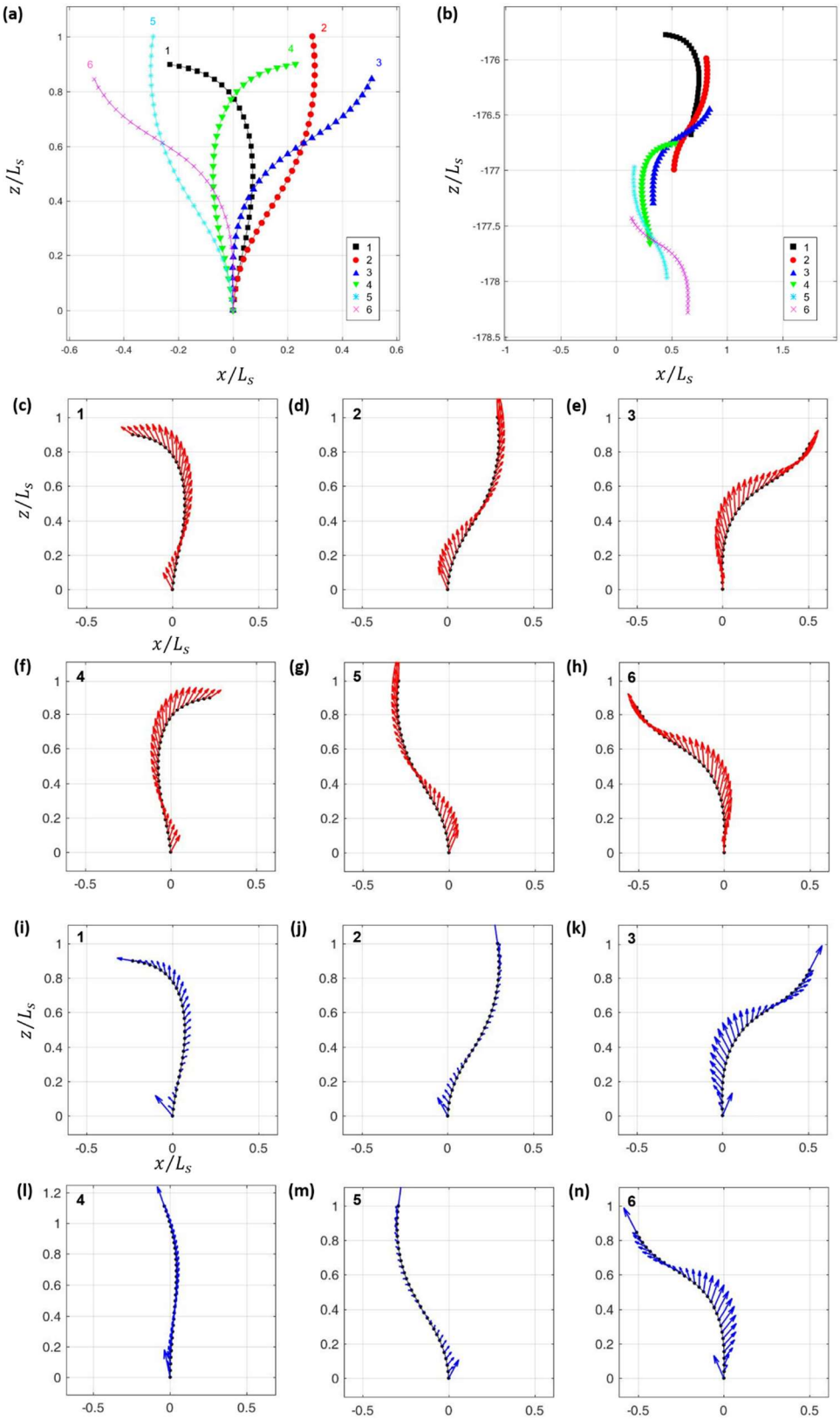

Figure C 23. Fast settling $\langle V_z \rangle / V_{z,still} = 1.446$; (a) Shape of a filament during sedimentation in relative coordinate of the lower end. (b) Shape of a filament during sedimentation in absolute coordinate. (c)-(h): Distribution of the relative velocity vectors of the flow. (i)-(n): Distribution of the force vectors by the flow. $Bn_{vor} = 0.72$ (the number of beads: 30, length: 4.45 m, mass: 0.5 kg, viscosity: 0.5 kg/ms, vortex velocity: $U_0 = 1.5\ m/s$, size of the vortex cell: $L_c/L_s = 1$)

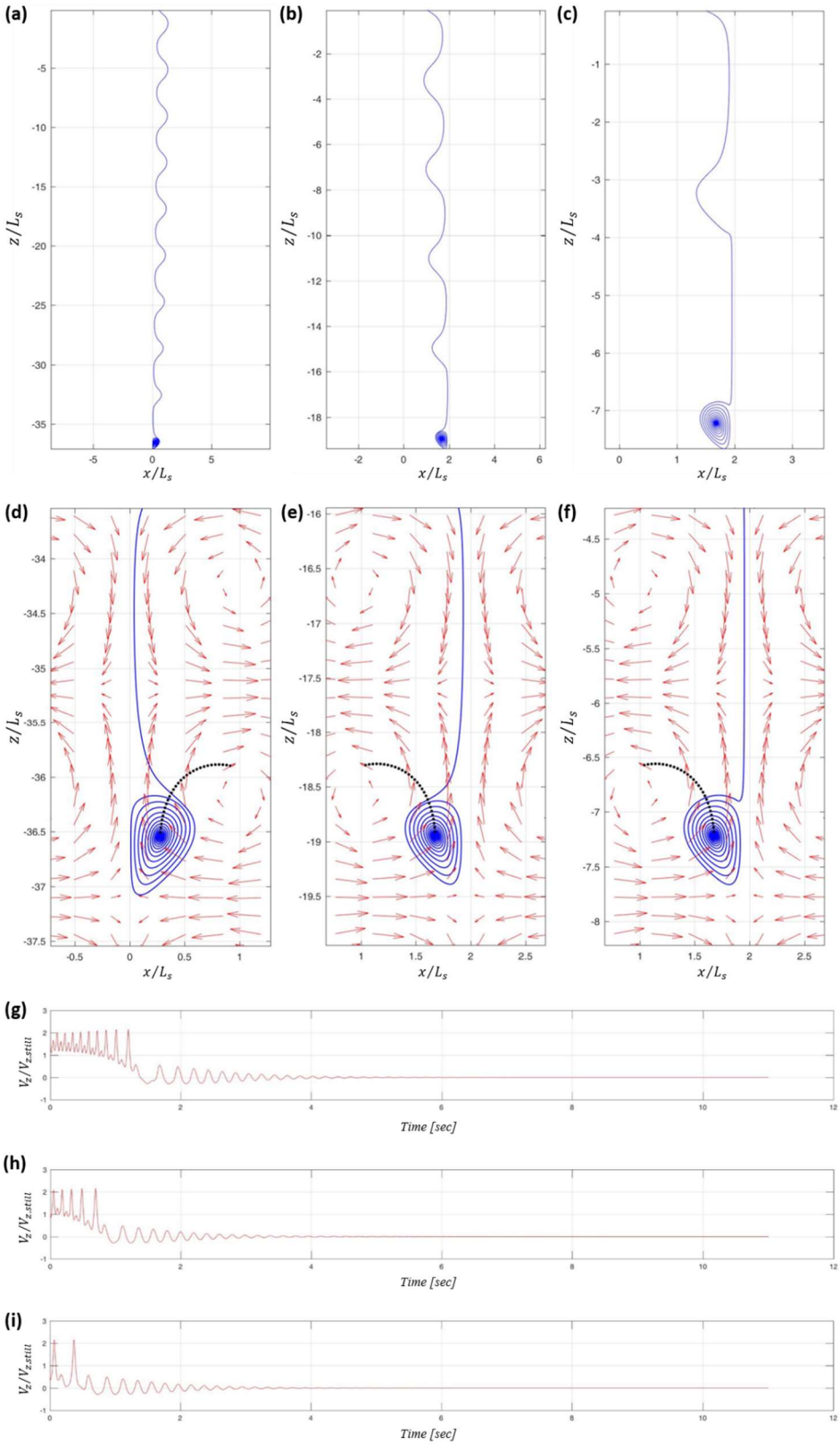

Figure C 24. Trapping $\langle V_z \rangle / V_{z,still} = 0$; (a)-(c): Trace plots of a point mass (spider body). (d)-(f): Flow fields and the bead-spring model. (blue lines: trajectory plots). (g)-(i): Nondimensionalised settling speeds over time. $Bn_{vor} = 0.72$ (the number of beads: 30, length: 4.45 m, mass: 0.5 kg, viscosity: 0.5 kg/ms, vortex velocity: $U_0 = 1.5\ m/s$, size of the vortex cell: $L_c/L_s = 2$; (a),(d),(g): $x_0/L_c = 0.25$; (b),(e),(h): $x_0/L_c = 0.5$; (c),(f),(i): $x_0/L_c = 0.75$)

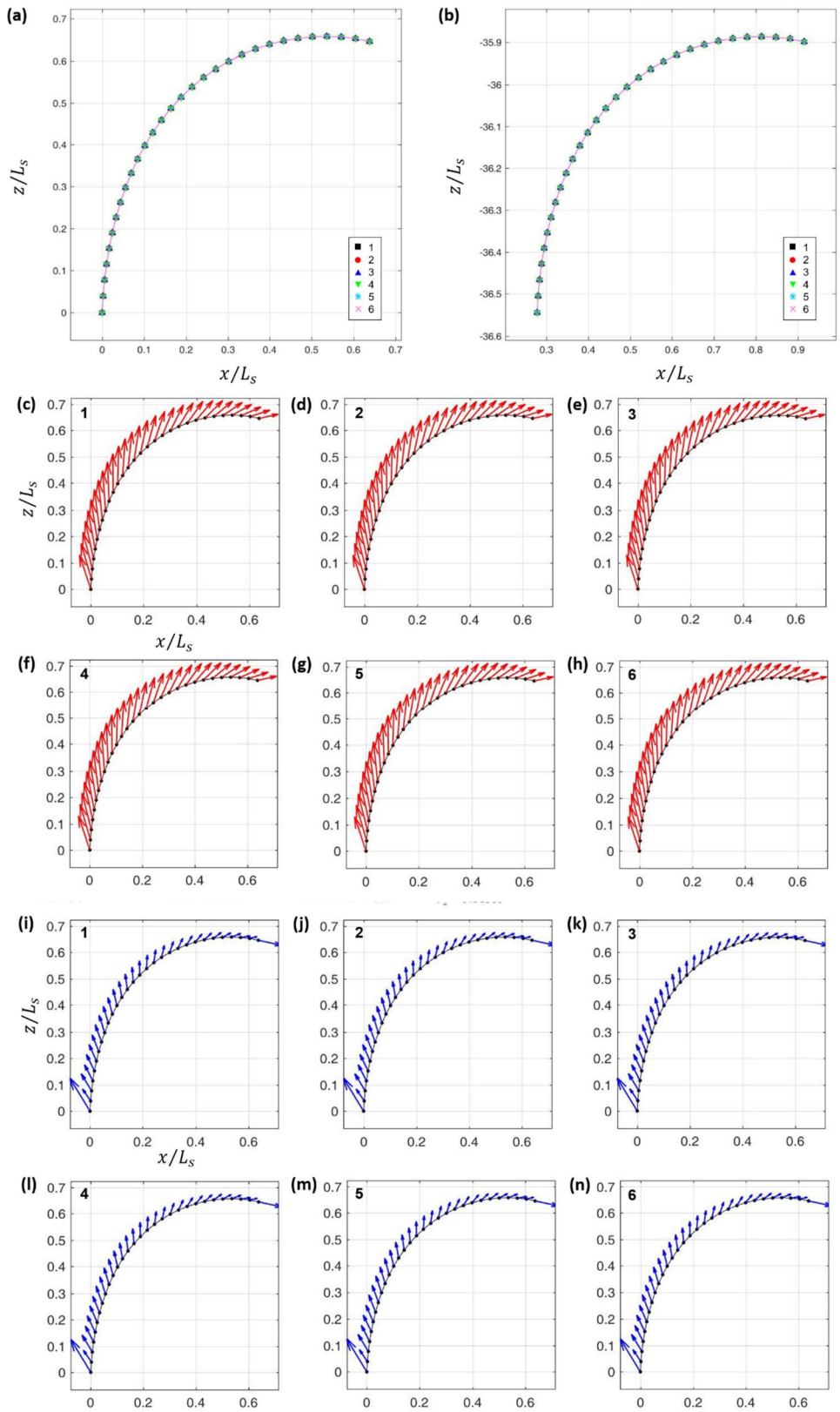

Figure C 25. Trapping $\langle V_z \rangle / V_{z,still} = 0$; (a) Shape of a filament during sedimentation in relative coordinate of the lower end. (b) Shape of a filament during sedimentation in absolute coordinate. (c)-(h): Distribution of the relative velocity vectors of the flow. (i)-(n): Distribution of the force vectors by the flow. $Bn_{vor} = 0.72$ (the number of beads: 30, length: 4.45 m, mass: 0.5 kg, viscosity: 0.5 kg/ms, vortex velocity: $U_0 = 1.5\, m/s$, size of the vortex cell: $L_c/L_s = 2$)

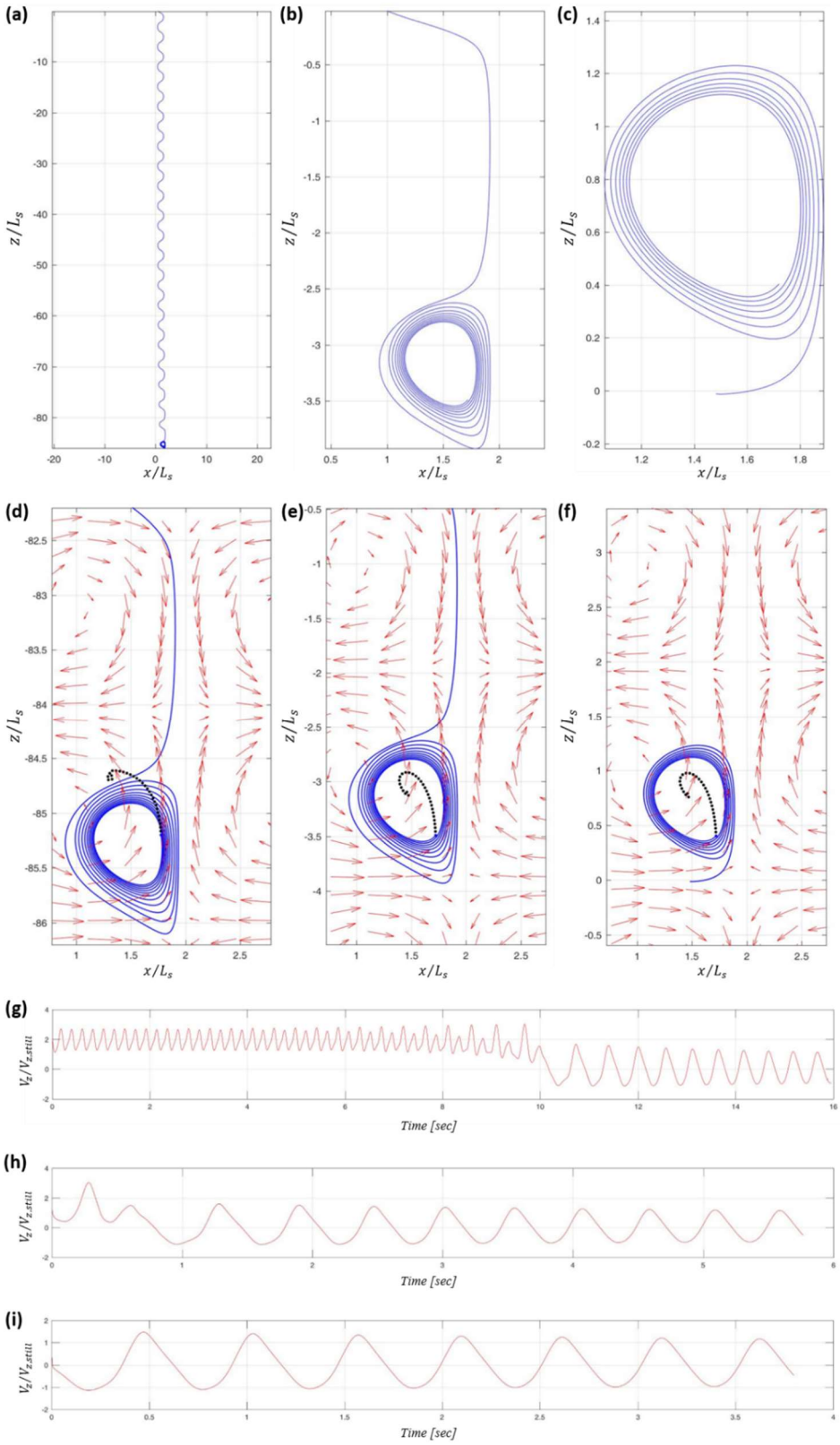

Figure C 26. Trapping $\langle V_z \rangle / V_{z,still} = 0$; (a)-(c): Trace plots of a point mass (spider body). (d)-(f): Flow fields and the bead-spring model. (blue lines: trajectory plots). (g)-(i): Nondimensionalised settling speeds over time. $Bn_{vor} = 1.13$ (the number of beads: 30, length: 4.45 m, mass: 0.1 kg, viscosity: 0.5 kg/ms, vortex velocity: $U_0 = 0.5\ m/s$, size of the vortex cell: $L_c/L_s = 2$; (a),(d),(g): $x_0/L_c = 0.25$; (b),(e),(h): $x_0/L_c = 0.5$; (c),(f),(i): $x_0/L_c = 0.75$)

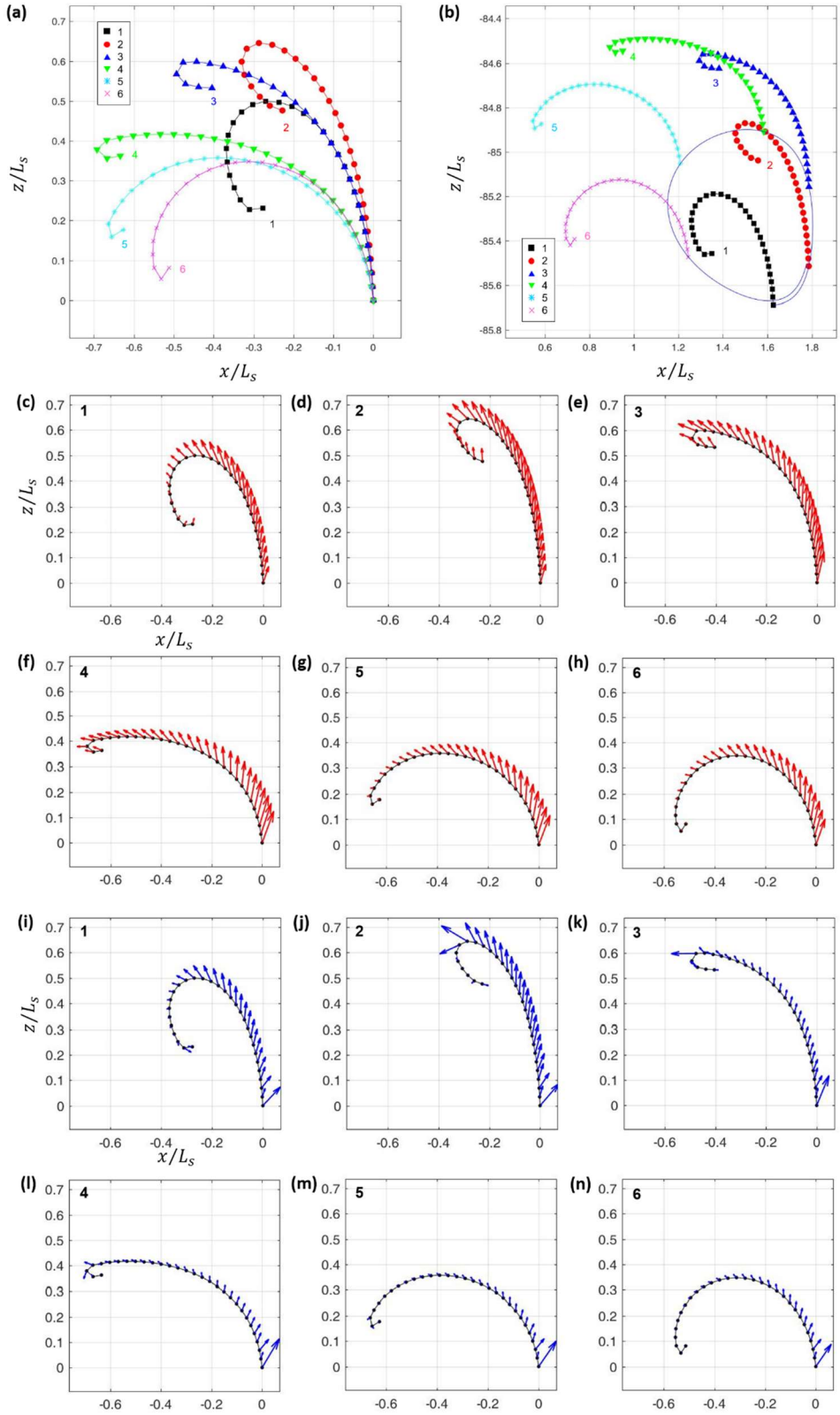

Figure C 27. Trapping $\langle V_z \rangle / V_{z,still} = 0$; (a) Shape of a filament during sedimentation in relative coordinate of the lower end. (b) Shape of a filament during sedimentation in absolute coordinate. (c)-(h): Distribution of the relative velocity vectors of the flow. (i)-(n): Distribution of the force vectors by the flow. $Bn_{vor} = 1.13$ (the number of beads: 30, length: 4.45 m, mass: 0.1 kg, viscosity: 0.5 kg/ms, vortex velocity: $U_0 = 0.5\ m/s$, size of the vortex cell: $L_c/L_s = 2$)

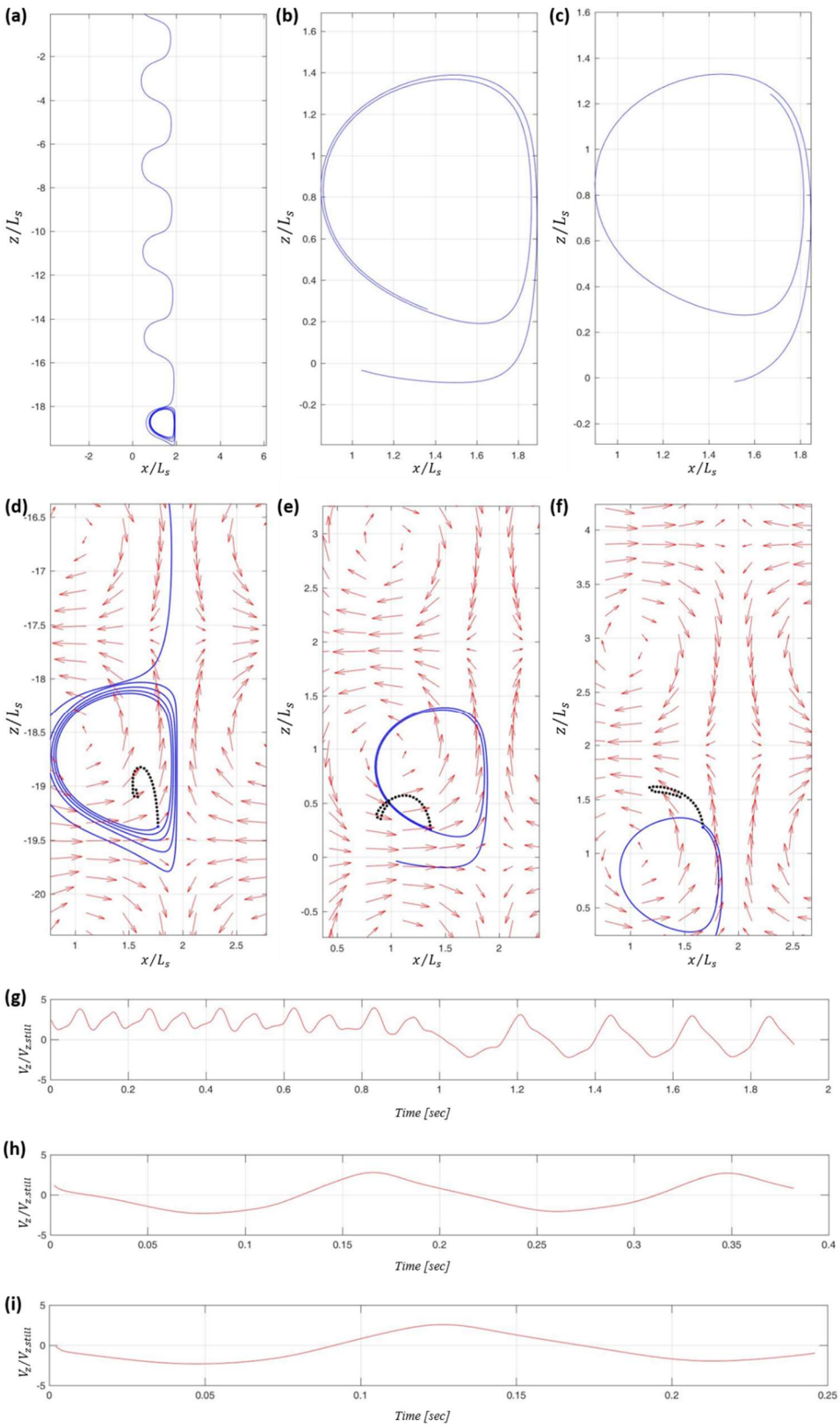

Figure C 28. Trapping $\langle V_z \rangle / V_{z,still} = 0$; (a)-(c): Trace plots of a point mass (spider body). (d)-(f): Flow fields and the bead-spring model. (blue lines: trajectory plots). (g)-(i): Nondimensionalised settling speeds over time. $Bn_{vor} = 1.72$ (the number of beads: 30, length: 4.45 m, mass: 0.2 kg, viscosity: 0.5 kg/ms, vortex velocity: $U_0 = 1.5\ m/s$, size of the vortex cell: $L_c/L_s = 2$; (a),(d),(g): $x_0/L_c = 0.25$; (b),(e),(h): $x_0/L_c = 0.5$; (c),(f),(i): $x_0/L_c = 0.75$)

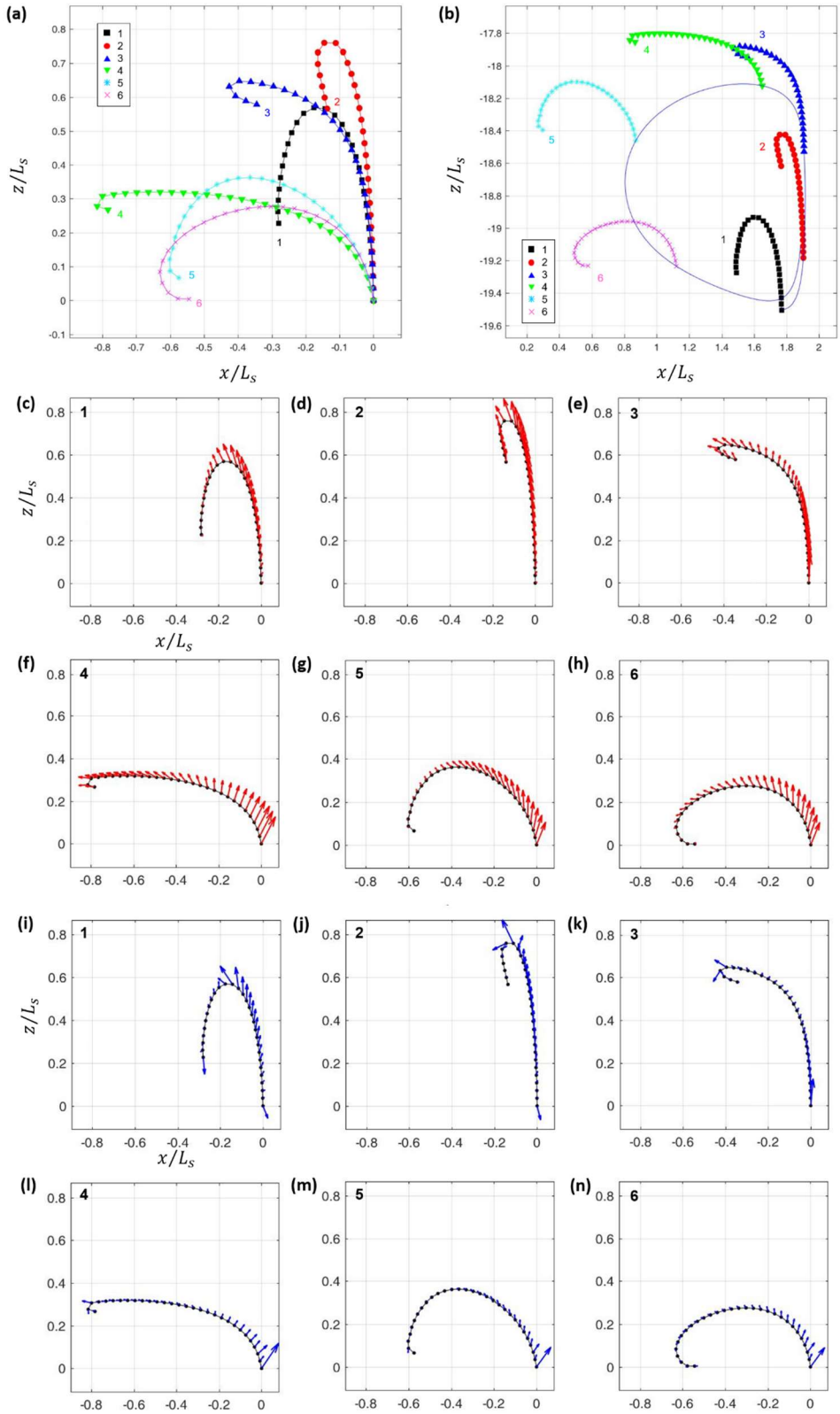

Figure C 29. Trapping $\langle V_z \rangle / V_{z,still} = 0$; (a) Shape of a filament during sedimentation in relative coordinate of the lower end. (b) Shape of a filament during sedimentation in absolute coordinate. (c)-(h): Distribution of the relative velocity vectors of the flow. (i)-(n): Distribution of the force vectors by the flow. $Bn_{vor} = 1.72$ (the number of beads: 30, length: 4.45 m, mass: 0.2 kg, viscosity: 0.5 kg/ms, vortex velocity: $U_0 = 1.5\ m/s$, size of the vortex cell: $L_c/L_s = 2$)